Inverse Problems in Electromagnetics

by

Xudong Chen

B. Eng. Zhejiang University, China (1999)
M. S. Zhejiang University, China (2001)

Submitted to the
Department of Electrical Engineering and Computer Science
in partial fulfillment of the requirements for the degree of

Doctor of Philosophy

at the

MASSACHUSETTS INSTITUTE OF TECHNOLOGY

May 2005
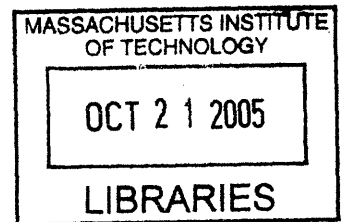
Author . . . .
Department of Electrical Engineering and Computer Science
May 10, 2005

Certified by . . . .
Jin Au Kong
Professor of Electrical Engineering and Computer Science
Thesis Supervisor

Certified by . . . .
Tomasz M. Grzegorczyk
Research Scientist
Thesis Co-Supervisor

Accepted by. . . . .
Arthur C. Smith
Chairman, Department Committee on Graduate Students

Inverse Problems in Electromagnetics

by

Xudong Chen

Submitted to the Department of Electrical Engineering and Computer Science
on May 10, 2005, in partial fulfillment of the
requirements for the degree of
Doctor of Philosophy

Abstract

Two inverse problems in eletromagnetics are investigated in this thesis. The first is the retrieval of the effective constitutive parameters of metamaterials from the measurement of the reflection and the transmission coefficients. A robust method is proposed for the retrieval of metamaterials as isotropic media, and four improvements over the existing methods make the retrieval results more stable. Next, a new scheme is presented for the retrieval of a specific bianisotropic metamaterial that consists of split-ring resonators, which signifies that the cross polarization terms of the metamaterial are quantitatively investigated for the first time. Finally, an optimization approach is designed to achieve the retrieval of general bianisotropic media with 72 unknown parameters. The hybrid algorithm combining the differential evolution (DE) algorithm and the simplex method steadily converges to the exact solution.

The second inverse problem deals with the detection and the classification of buried metallic objects using electromagnetic induction (EMI). Both the exciting and the induced magnetic fields are expanded as a linear combination of basic modes in the spheroidal coordinate system. Due to the orthogonality and the completeness of the spheroidal basic modes, the scattering coefficients are uniquely determined and are characteristics of the object. The scattering coefficients are retrieved from the knowledge of the induced fields, where both synthetic and measurement data are used. The ill-conditioning issue is dealt with by mode truncation and Tikhonov regularization technique. Stored in a library, the scattering coefficients can produce fast forward models for use in pattern matching. In addition, they can be used to train support vector machine (SVM) to sort objects into generic classes.

Thesis Supervisor: Jin Au Kong
Title: Professor of Electrical Engineering and Computer Science

Thesis Co-Supervisor: Tomasz M. Grzegorczyk
Title: Research Scientist

Acknowledgments

I am deeply indebted to my thesis supervisor Prof. Jin Au Kong who has given me the opportunity to study electromagnetics at the Center for Electromagnetic Theory and Applications (CETA). It was my distinct pleasure to be a teaching assistant for several of his classes. His passion, humor, and wisdom exhibited in his teaching will always inspire me. His deep insight initiated the research work in the fourth chapter of the thesis. Through his broad, extensive knowledge and skill, Prof. Kong teaches me not only electromagnetic theory, but also other aspects of life, from literature, story-telling, to leadership and management ability. Prof. Kong's kindness and friendship will always be in my heart.

I also thank my co-supervisor Dr. Grzegorczyk whose contribution to the constitutive parameter retrieval part of this thesis is invaluable. Without his help and advice, my work in this part will be slowed or even stopped. I appreciate his patience in correcting my grammar not only in my papers but also in my other documents. His infinite passion in work also inspires me to work hard. I am grateful for his kindness in helping me to rehearse my presentations for the RQE and the thesis defense. Also many thanks for his kind help in many other areas in my life.

Also deserving special thanks is Dr. Kevin O'Neill, who has in many respects been a co-supervisor of this thesis specifically with reference to the buried-object detection chapter. Through two and half years of working with him, I know he is really a good mentor. For my work in the fifth chapter of this thesis, I actually worked on a general idea that he built up two and half years ago, and since then he has helped me dig into the details. All the experimental data were provided by him. When we work together, many of his words like "I believe you" encourage me and make me warm. His working spirit also excites me to work hard. Besides academic mentoring, he has also been my good friend: he plays jokes on me and he learns Chinese from me. His help, patience, and respect are invaluable to me.

It is my pleasure to also recognize my colleagues in the CETA group. Benjamin Barrowes's work in the spheroidal modeling has had an important impact on the buried-object detection part of this thesis. I am indebted to him for his early tutoring as well as for his friendship. The software tips I learned from him saved me lot of time. Jianbing Chen has

lives. I have kept in touch with many good friends in China by phone or email in the past four years. Thank you, Li Jin, Xiangwei Li, Meng Wang, Yongjun Ye, and Yu Yuan.

I would like to thank Prof. Guangzheng Ni, my master thesis supervisor at Zhejiang University, China. I made the right decision to change my undergraduate major and choose such a knowledgeable, energetic, eloquent, and charming professor as my master thesis supervisor. During the two years I worked at his lab, he gave me sufficient freedom to choose research topics and encouraged me to publish papers. Besides, he also cared for my concerns in life. I always remember his warm words when he saw me staying late at office, "Don't work too hard. Health is the most important."

Also deserving of special thanks are Prof. Shiyou Yang and Prof. Qifan Yang at Zhejiang University. As my master thesis co-supervisor, Prof. Shiyou Yang brought me into a fantastic world, the research of inverse problems. The optimization technique I learned at Zhejiang University is closely related to the work done in this thesis. Prof. Qifan Yang is one of the best lecturers I've ever met. What I learned from him is not only the theories in math, but also the ability to solve real problems. His guidance and special care in my participation in the Mathematical Contest in Modeling will be always in my heart.

Finally, I wish to express my utmost gratitude for my parents and some of my relatives. Neither of my parents went to college, but they have always held me to a high standard in my studies. My family was not wealthy, but they saved money to support my brother's and my own education. They care not only our academic work, but also our characters. I have been taught to be honest, polite, considerate, warm-hearted, and respectful. Dear Dad and Mom, I love you. This thesis is my best gift for you so far. Thank you. I would also like to thank my dearest brother, Xufeng, for his confidence in me and for his care of our parents during my thirteen years of study away from home. My Aunt Xiuling Yue and my grandma have encouraged me and believed in my ability since the first day I entered the elementary school. Their spiritual and financial support of my studies will never be forgotten. Thank you!

Contents

List of Figures

14

15

16

List of Tables

Chapter 1

Introduction

This thesis investigates two inverse problems in electromagnetics. The first problem, the retrieval of the effective constitutive parameters of metamaterials from the measurement of the reflection and the transmission coefficients, is addressed in chapter 2, 3 and 4. The second inverse problem deals with the detection and the classification of buried objects using electromagnetic induction (EMI), which is covered in chapter 5 of the thesis.

Left-handed metamaterials have been a subject of important scientific interest since the first experimental verification of a negative refraction [1]. In 1968, Veselago first introduced a medium with simultaneously negative permittivity and permeability [2]. Since the electric field vector, magnetic field vector, and the wavenumber form a left-handed system in it, this medium is called a left-handed medium (LHM). Nevertheless, real materials with simultaneously negative permittivity and permeability are not available. However, in the last few years, left-handed media have been experimentally designed as artificial materials, or metamaterials [1, 3, 4], following the theoretical work by Pendry [5, 6]. There are many interesting phenomena associated with LHM, such as a negative refraction [1], a lateral beam shift [7], a perfect imaging effect [8], and a reversed Doppler shift [2].

Constitutive parameters are important in quantitatively characterizing the wave propagation inside homogeneous media. However, designed as engineered composite structures, metamaterials are inhomogeneous. Typical left-handed metamaterials consist of periodic infinite metallic wires and split-ring resonators (SRRs), where the periodic infinite metallic wires can be effectively modeled as a dilute plasma, thus providing a negative permittivity

(ϵ) [5], and the periodic arrays of SRRs give a negative permeability (μ) [6]. In spite of their inhomogeneity, metamaterials can be replaced conceptually by homogeneous materials under some circumstances so that there would be no difference in the observed electromagnetic responses between the two. The above replacement is achieved when the applied fields have spatial variation on a scale significantly larger than the periodicity of the wires and SRRs, in which case the composite metamaterial is said to form an effective medium.

There are many ways to obtain the effective constitutive parameters of metamaterials. In the numerical approach, the electromagnetic fields inside metamaterials are calculated, and the constitutive parameters are obtained by taking the ratios of the spatially averaged fields, i.e., $\epsilon = \frac{<\overline{D}>}{<\overline{E}>}$ and $\mu = \frac{<\overline{B}>}{<\overline{H}>}$, where $< \cdot >$ denotes a spacial-average operator [9, 6]. Such an approach is feasible for numerical simulations, but is hard to apply to experimental measurements. Alternatively, analytical approaches describe the electromagnetic properties using some approximate analytical models for given metamaterial structures. While analytical approaches give insights into the relationship between the physical properties and geometrical properties of metamaterials, they become increasingly difficult to use in metamaterials with complicated geometry structures. Consequently, retrieval techniques are more commonly used because they can be applied to both simple and complicated structures, and can use both numerical and experimental data. In the retrieval approach, we assign the effective constitutive parameters to the metamaterial so that the scattered waves (i.e., the reflection and transmission coefficients, or S parameters) from a planar slab of the hypothetical homogeneous medium match those from a slab of metamaterial with the same thickness. The retrieved constitutive parameters, even if approximate, are helpful in the design of metamaterials and in the interpretation of their scattering properties.

In the retrieval of the constitutive parameters, three stages of retrieval are addressed. First, in chapter 2, a robust method is proposed for the retrieval of metamaterials as isotropic media, and four improvements over the existing methods make the retrieval results more stable. Second, chapter 3 presents a new scheme for the retrieval of a specific bianisotropic metamaterial that consists of split-ring resonators, which signifies that the cross polarization terms of the metamaterial are quantitatively investigated for the first time. Finally, an optimization approach is designed in chapter 4 to achieve the retrieval of general bian-

isotropic media. The hybrid algorithm combining the differential evolution (DE) algorithm and the simplex method steadily converges to the exact solution.

Chapter 5 is dedicated to the detection and the classification of buried objects using electromagnetic induction (EMI). The detection and removal of buried unexploded ordnance (UXO) is an important environmental problem, made very expensive and challenging by the high false alarm rate. Among the techniques for detecting UXOs, electromagnetic induction is promising and has been widely explored [10, 11, 12, 13, 14, 15]. It is well-known that time varying fields induce a current flow in the electrically conductive and/or magnetically permeable objects placed in their vicinity, and the induced current produces magnetic fields, known as the secondary fields (correspondingly, the exciting fields are referred to as the primary fields). We can then detect and discriminate the objects through the observation of the secondary fields.

Many numerical techniques are available for EMI calculation in the magneto-quasistatic (MQS) regime. Two of the most widely used models that work well for simple structures are (1) the dipole model [10, 16], in which one approximates the response of an object with one or a number of independently responding magnetic dipoles, and (2) sphere models [17], in which one approximates the object with a sphere. But many objects are complicated enough so that it is impossible or very difficult to approximate them with independent dipoles or spheres so that we need to resort to more complicated analytical geometries [18, 19, 20]. For such objects, recent forward modeling approaches in terms of standardized excitations succeed in capturing the most complex magneto-quasistatic scattering behavior, including all near field, material and geometrical heterogeneity, and internal interaction effects [21, 22, 23, 24, 25]. The essential idea is that any excitation can be constructed from a set of basic inputs and, thus, the response corresponding to the complete excitation can be constructed just by superposition of responses to the basic excitations. Spheroidal modes are chosen in this work because the spheroidal coordinate system can be made to conform to the general shape of an object of interest, whether flattened or elongated, and many of our objects of interest are bodies of revolution [13, 26]. In the spheroidal coordinate system, both the primary and the secondary magnetic fields are expressed as linear superpositions of basic modes. Due to the orthogonality and the completeness of the spheroidal basic

25

modes, the scattering coefficients, in response to unitary magnitude of the primary mode excitation, are uniquely determined. They are characteristics of the object and can then be treated as discriminators in the pattern matching and classification.

Previous work has shown that many geometrically complicated elongated metallic objects can often be represented effectively in the MQS realm by a spheroid [27]. Thus we first attempt to process ultra-wide band (UWB) MQS data to infer the properties of an equivalent spheroid, thereby characterizing the material properties, general shape, and location of a subsurface object. Beyond this, the response of any discrete scatterer (including non-spheroidal objects) can be represented in terms of basic mode solutions in spheroidal coordinates. Theoretical analysis proves that the scattering coefficients are characteristics of the object, which is subsequently verified by numerical examples. The scattering coefficients are retrieved from the knowledge of the secondary fields, where both the synthetic and measurement data are used. The ill-conditioning issue is dealt with by mode truncation and Tikhonov regularization technique. Stored in a library, the scattering coefficients can produce fast forward models for use in pattern matching. Also they can be used to train a support vector machine (SVM) to sort objects into generic classes, such as elongated or not, permeable or not. The success of the retrieval from both synthetic and measurement data shows the promise of the spheroidal mode approach in the detection and classification of buried objects.

Chapter 2

Retrieval of the isotropic metamaterial

2.1 Introduction

Left-handed (LH) structures have been realized so far as metamaterials [1, 3, 4] and very quickly, researchers have been working on retrieving their effective permittivity and permeability to better characterize them [28, 29, 30]. Known methods to date [31, 32] use S parameters calculated from a wave incident normally on a slab of metamaterial, from which the effective refractive index n and impedance z are first obtained. The permittivity ϵ and permeability μ are then directly calculated from $\mu = nz$ and $\epsilon = n/z$. Note that the values of ϵ, μ and z are relative to those in free-space, thus dimensionless. The permittivity and permeability are tensors in general, but here we restrict the incidence so that we can focus only on one of their principal axes.

It is also known that this retrieval process may fail in some instances, such as when the thickness of the effective slab (exhibiting bulk properties) is not accurately estimated [28] or when reflection (S_{11}) and transmission (S_{21}) data are very small in magnitude [30]. Although these issues have been addressed to some extent in previous works, we have found that the retrieved results in some cases are still unsatisfactory. This chapter proposes four improvements over the existing method, and the improved method retrieves stable results. Some typical retrieval results are presented to show the robustness and effectiveness of the method.

2.2 Retrieval method

2.2.1 Theoretical retrieval equations

In order to retrieve the effective permittivity and permeability of a slab of metamaterial, we need to characterize it as an effective homogeneous slab. In this case, we can retrieve the permittivity and permeability from the reflection (S_{11}) and transmission (S_{21}) data. For a plane wave incident normally on a homogeneous slab of thickness d with the origin coinciding with the first face of the slab, S_{11} is equal to the reflection coefficient, and S_{21} is related to the transmission coefficient T by $S_{21} = Te^{ik_0d}$, where k_0 denotes the wavenumber of the incident wave in free-space. The S parameters are related to refractive index n and impedance z by [33, 31, 7]:

$$S_{11} = \frac{R_{01}\left(1 - e^{i2nk_0d}\right)}{1 - R_{01}^2 e^{i2nk_0d}}, \tag{2.1a}$$

$$S_{21} = \frac{(1 - R_{01}^2)e^{ink_0d}}{1 - R_{01}^2 e^{i2nk_0d}}, \tag{2.1b}$$

where $R_{01} = \frac{z-1}{z+1}$.

As it has been pointed out in [28, 29], the refractive index n and the impedance z are obtained by inverting Eqs. (2.1), yielding

$$z = \pm\sqrt{\frac{(1 + S_{11})^2 - S_{21}^2}{(1 - S_{11})^2 - S_{21}^2}}, \tag{2.2a}$$

$$e^{ink_0d} = X \pm i\sqrt{1 - X^2}, \tag{2.2b}$$

where $X = \frac{1}{2S_{21}}(1 - S_{11}^2 + S_{21}^2)$. Since the metamaterial under consideration is a passive medium, the signs in Eqs. (2.2) are determined by the requirement

$$z' \geq 0, \tag{2.3a}$$

$$n'' \geq 0, \tag{2.3b}$$

where $(\cdot)'$ and $(\cdot)''$ denote the real part and imaginary part operators, respectively. The

28

value of refractive index n can be determined from Eq. (2.2b) as:

$$n = \frac{1}{k_0 d} \left\{ \left[\left[\mathrm{Ln}(e^{ink_0 d}) \right]'' + 2m\pi \right] - i \left[\mathrm{Ln}(e^{ink_0 d}) \right]' \right\}, \tag{2.4}$$

where m is an integer related to the branch index of n'. As mentioned above, the imaginary part of n is uniquely determined, but the real part is complicated by the branches of the logarithm function.

Eqs. (2.2) can be directly applied in the case of a homogeneous slab for which the boundaries of the slab are well-defined and the S parameters are accurately known. However, since a metamaterial itself is not homogeneous, the two apparently straightforward issues mentioned above need to be carefully addressed. First, the location of the two boundaries of the effective slab need to be determined, which we do here by ensuring a constant impedance for various slab thicknesses. Second, the S parameters obtained from numerical computation or measurements are noisy which can cause the retrieval method to fail, especially at those frequencies where z and n are sensitive to small variations of S_{11} and S_{21}. These two problems are examined in detail in the following sections.

2.2.2 Determination of the first boundary and the thickness of the effective slab

A homogeneous slab of material can be characterized by the fact that its impedance does not depend on its thickness. My understanding of the physical meaning of the first effective boundary is a plane beyond which the reflected wave behaves like a plane wave for a plane wave incidence. When a plane wave is incident on a metamaterial, currents will be induced on the metals creating a scattered field. The field produced by the induced currents is not uniform: it is strongest around the metal and decay at a certain distance. By definition, the first effective boundary is a plane beyond which the reflected wave is a plane wave in free space, and it has to be determined. We use z_1 and z_2 to represent the impedances of two slabs of metamaterial of different thicknesses. The reflection S_{11} depends on the defined position of the first boundary and the transmission S_{21} depends on the thickness of the slab. In addition, since the impedance z is also a function of S_{11} and S_{21}, z depends on the first

boundary and the thickness of the slab as well. Taking into account the above-mentioned properties, we propose a method whereby the first boundary and the thickness of the sample are determined by optimization so that z_1 matches z_2 at all frequencies. Fig. 2-1 illustrates the configuration of the problem for a metamaterial made of two cells in the propagation direction (x direction). The geometry of the metamaterial has been taken from [34, 35], in which the dimensions have been slightly modified for ease of discretization in FDTD simulations. With the split-ring resonator (SRR) and rod in the center of the unit cell, the periodicity in $\hat{x}$ direction is d_0, as shown in Fig. 2-1. The first boundary of the effective homogeneous medium is located at x_1 below ($x_1 \geq 0$) or above ($x_1 < 0$) the first unit cell boundary, and the thickness of the effective medium is $Nd_0 + x_2 - x_1$ for a N-cell metamaterial ($N = 2$ in the case shown in Fig. 2-1). The optimization model is set up to minimize the mismatch of impedances of different numbers of cells of metamaterial:

$$\min \quad f(\overline{x}) \; = \; \frac{1}{N_f} \sum_{i=1}^{N_f} \frac{|z_1(f_i, \overline{x}) - z_2(f_i, \overline{x})|}{\max\{|z_1(f_i, \overline{x})|, |z_2(f_i, \overline{x})|\}}, \qquad (2.5)$$

$$\text{s.t.} : \qquad -0.5d_0 \leq x_1, x_2 \leq 0.5d_0, \qquad \overline{x} = (x_1, x_2),$$

where N_f is the total number of sample frequencies and $z_j(f_i)$ represents the impedance of slab j ($j = 1, 2$) at frequency f_i.

In the ideal case, z_1 matches z_2 for all frequencies with the objective function value equal to zero. We use the differential evolution (DE) algorithm [36] to optimize the objective function. For the structure shown in Fig. 2-1, we optimize the effective boundaries in order to match the impedances of one and two cells of metamaterial, and the obtained optimization solution is $\overline{x}_{opt} = (3.8565 \times 10^{-4}d_0, 1.0479 \times 10^{-4}d_0)$. For this optimized effective boundaries, the impedances of one, two, and three cells of the metamaterial retrieved from the S parameters (obtained from FDTD simulations) are shown in Fig. 2-2. It can be seen that the retrieved impedances for 1, 2 and 3 cells of metamaterial match well for most frequencies, while matching was not as satisfactory when the method in [28] was used (which corresponds to $x_1 = 0.5d_0$ in our formulation). We also calculated the impedance z for the case of $\overline{x} = (0, 0)$ and found that the results are almost the same
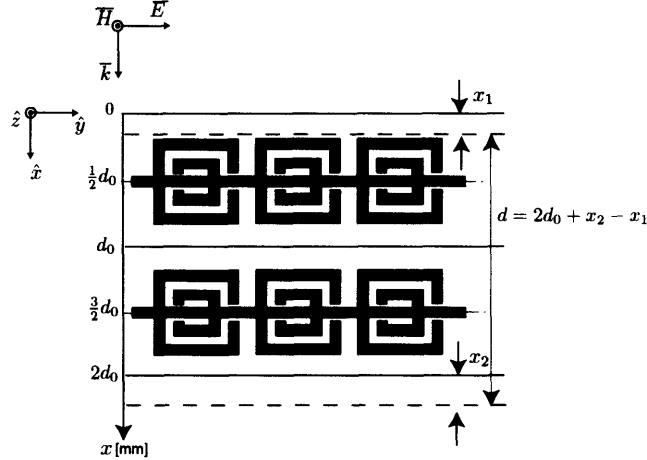
Figure 2-1: Illustration of the effective boundaries of a 2-cell metamaterial. The SRRs and rods are periodic along $\hat{y}$ and $\hat{z}$ directions with periodicity $a_y = 4\text{mm}, a_z = 3\text{mm}$. The unit-cell thickness (d_0) in the direction of wave incidence is 4 mm. We choose the first and the last unit cell boundary as the reference plane for the parameters x_1 and x_2, respectively. The value of x_1 and x_2 are positive/negative if the dash lines are below/above their reference planes. The thickness of the effective homogeneous medium is $2d_0 + x_2 - x_1$ [mm].

as the optimized ones. We have corroborated this result with many other metamaterial thicknesses and geometries (periodic rod structure and the geometry shown in the inset of Fig. 2-8(a)) to eventually conclude empirically that the first effective boundary of a symmetric one-dimensional (1D) metamaterial (one pair of ring and rod within each unit cell) [28, 3, 82] coincides with the first unit cell boundary and the second effective boundary coincides with the last unit cell boundary. For 2D (two pairs of ring and rod within each unit cell) [34, 82] and asymmetric 1D metamaterials, no such rule could be found and the effective boundaries of the slab need to be determined from optimization.

2.2.3 Determination of n and z from S_{11} and S_{21}

It is a common method to determine z and n from Eqs. (2.2) with the requirement of Eqs. (2.3), where z and n are determined independently. However this method may fail in practice when z' and n'' are close to zero: a little perturbation of S_{11} and S_{21}, easily produced in experimental measurements or numerical simulations, may change the sign of z' and n'',

31

(a) Real part of z (b) Imaginary part of z
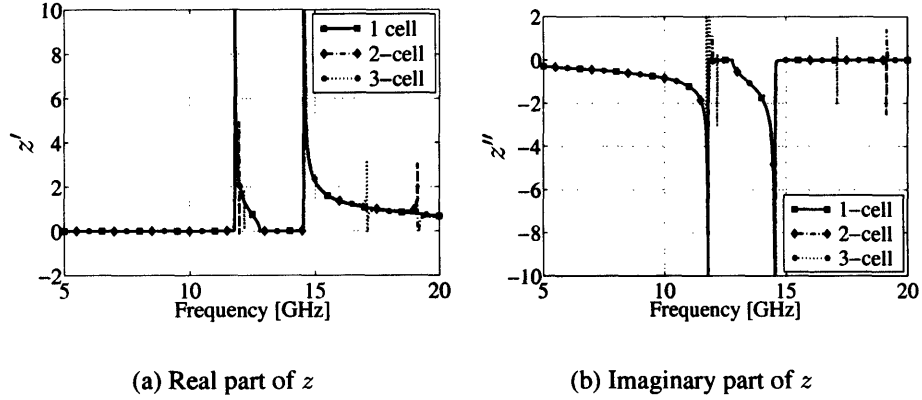
Figure 2-2: Optimized impedance z for 1, 2 and 3 cells of metamaterial of Fig. 2-1 in the direction of propagation.

making it unreliable to apply the requirement of Eqs. (2.3), as discussed in [30]. In fact, z and n are related and we should use their relationship to determine the signs in Eqs. (2.2). In order to determine the correct sign of z, we distinguish two cases. The first is for $|z'| \geq \delta_z$, where δ_z is a positive number, for which we apply Eq. (2.3a). In the second case, for $|z'| < \delta_z$, the sign of z is determined so that the corresponding refractive index n has a non-negative imaginary part, or equivalently $|e^{ink_0d}| \leq 1$, where n is derived from Eqs. (2.1):

$$e^{ink_0d} = \frac{S_{21}}{1 - S_{11}\frac{z-1}{z+1}}.$$ (2.6)

Note that once we obtain the value of z, the value of e^{ink_0d} is obtained from Eq. (2.6), so that we avoid the sign ambiguity in Eq. (2.2b). When the z in Eq. (2.2a) with a positive sign is plugged into Eq. (2.6), Eq. (2.6) is simplified by straightforward algebraic manipulation to Eq. (2.2b) with a negative sign. Correspondingly, the z in Eq. (2.2a) with a negative sign leads to a positive sign in Eq. (2.2b). Fig. 2-3 shows the retrieved impedance using the method presented in this chapter and using only the condition of Eq. (2.3a). It is noted that the discontinuities obtained when only applying the criterion $z' \geq 0$ are removed.

32
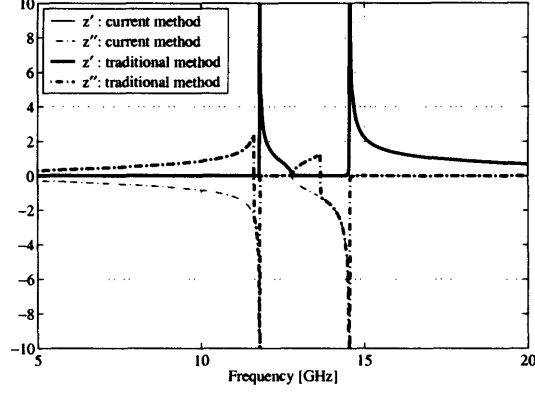
Figure 2-3: Comparison of the retrieved impedance z (real and imaginary parts) for one cell of metamaterial shown in Fig. 2-1 by the method presented in this chapter and a traditional method using only the requirement $z' \geq 0$.

2.2.4 Determination of the branch of n'

We have presented in the previous sections a method of solving for z and n'', but n' remains ambiguous because of the branches of logarithm function as seen in Eq. (2.4). In order to address this problem, it has been suggested to use a slab of small thickness and applying the requirement that $\epsilon(f)$ and $\mu(f)$ are continuous functions of frequency [28, 29]. However, no further details on the continuity argument were provided. In our method, we determine the proper branch by using the mathematical continuity of the parameters, with special attention to possible discontinuities due to resonances. The method is an iterative one: assuming we have obtained the value of the refractive index $n(f_0)$ at frequency f_0, we obtain $n(f_1)$ at the next frequency sample f_1 by expanding the function $e^{in(f_1)k_0(f_1)d}$ in a Taylor series:

$$e^{in(f_1)k_0(f_1)d} \approx e^{in(f_0)k_0(f_0)d}\left(1 + \Delta + \frac{1}{2}\Delta^2\right), \tag{2.7}$$

where $\Delta = in(f_1)k_0(f_1)d - in(f_0)k_0(f_0)d$ and $k_0(f_0)$ denotes the wavenumber in free-space at frequency f_0.

In Eq. (2.7), the branch index (m in Eq. (2.4)) of the real part of $n(f_1)$ is the only unknown. Since the left-hand side of Eq. (2.7) is obtained from Eq. (2.6), Eq. (2.7) is a binomial function of the unknown $n(f_1)$. Out of the two roots, one of them is an approx-

33

imation of the true solution. Since we have obtained $n''(f_1)$, we choose the correct root among the two by comparing their imaginary parts with $n''(f_1)$. The root whose imaginary part is closest to $n''(f_1)$ is the correct one, and we denote it as n_0. Since n_0 is a good approximation of $n(f_1)$, we choose the integer m in Eq. (2.4) so that $n'(f_1)$ is as close to n'_0 as possible.

The branch of n' at the initial frequency is determined as follows: from $\mu = nz$ and $\epsilon = n/z$, we have

$$\mu'' = n'z'' + n''z', \tag{2.8a}$$

$$\epsilon'' = \frac{1}{|z|^2} \left(-n'z'' + n''z' \right). \tag{2.8b}$$

The requirements $\mu'' \geq 0$ and $\epsilon'' \geq 0$ lead to

$$|n'z''| \leq n''z'. \tag{2.9}$$

In particular, when $n''z'$ is close to zero but z'' is not, n' should be close to zero. At the initial frequency, we solve for the branch integer m satisfying Eq. (2.9). If there is only one solution, it is the correct branch. In case of multiple solutions, for each of the candidate branch index m, we determine the value of n' at all subsequent frequencies using the above-mentioned iterative method. Because the requirement of Eq. (2.9) applies to n' at all frequencies, we use it to check the validity of n' at all frequencies produced by the candidate initial branch. Note in the special case when $n''z'$ is close to zero but z'' is not, the checking process can easily be carried out. Therefore, the initial branch that satisfies Eq. (2.9) at both the initial frequency and the subsequent frequencies is the correct one.

For the metamaterial structure shown in Fig. 2-1, we found that there is a frequency region at which there is no branch index m satisfying Eq. (2.9). We call this frequency region the resonance band. The properties of the resonance band are still disputed by researchers. Some papers [37, 38, 39] mention the existence of multiple modes in this region since the real part of n is large, yielding a wavelength comparable to or smaller than

34

the unit size of the metamaterial thereby rendering the retrieval of the effective parameters of the metamaterials impossible. Other papers [29, 40] state that retrieval is possible and the retrieved permittivity ϵ has a negative imaginary part in the resonance band. Here, we do not address this issue and for this reason the retrieved results presented here are interrupted in frequency by the resonance region (see for example Fig. 2-4). In this case, since $n(f)$ is not continuous through all frequencies, we have to determine the initial branches for two frequency regions: below and above the resonance band. Note that below the resonant band, the retrieved branch index is zero, which confirms the validity of the traditional method used for low frequency retrieval. The retrieved refractive indexes n for 1, 2 and 3 cells in the propagation direction are shown in Fig 2-4, where the resonance band is seen to extend between 11 GHz and 12 GHz. We observe that the values of n for different cell numbers are identical above the resonant region. Below the resonant band, however, the retrieved n for 1 and 2 cells match well, but the result for 3 cells differs significantly from the previous two. This discrepancy is due to the small magnitude of S_{21} in this frequency band, as we shall discuss in the next section.
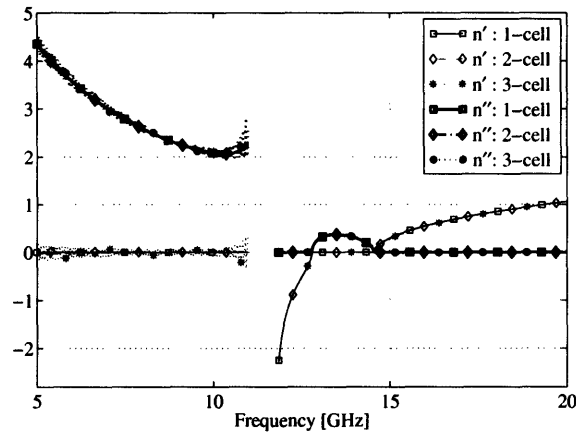
Figure 2-4: Retrieved refractive index n (real and imaginary parts) for 1, 2 and 3 cells of the metamaterial structure shown in Fig. 2-1.

2.2.5   Sensitivity analysis

Although the retrieved z and n for 1, 2, 3 cells of metamaterial presented so far match well for most of frequencies, a close examination shows that the three results do not match well

35

at some specific frequencies. There are two cases of discrepancies. The first is that the retrieved refractive index n for 3 cells of metamaterial does not match the value for 1 and 2 cells at low frequencies (5 GHz $\sim$ 11 GHz in Fig. 2-4). The second is that the impedance z appears to spike at some frequencies (around 12.2 GHz, 17 GHz, 19.5 GHz in Fig. 2-2). We shall show here that these discrepancies are due to the sensitivity of z and n to the accuracy of S_{11} and S_{21}.

The first case appears when $|S_{21}|$ is close to zero. In the region below the resonance band, the transmission is usually small, especially for thicker metamaterials. From Eq. (2.2b), we see that S_{21} appears in the denominator, so that the values of n are very sensitive to small perturbations of S_{21}. Yet, a small transmission has little influence on the retrieval of z, which can be seen by computing:

$$\frac{\partial z^2}{\partial S_{21}} = \frac{8 S_{21} S_{11}}{\left[(1 - S_{11})^2 - S_{21}^2\right]^2},\qquad (2.10)$$

from which it is clear that a small $|S_{21}|$ makes $\frac{\partial z^2}{\partial S_{21}}$ small (approximately zero). In addition, we can see from Eq. (2.1b) that if n'' is not small, S_{21} will decrease exponentially with d, i.e. with an increasing number of cells in the propagation direction. Therefore, the smaller S_{21}, the higher the computation and measurement relative errors, which leads to less accurate retrieval results.

The second case appears when S_{21}^2 is close to unity while S_{11} is close to zero. Similar to the first case, the denominator in the expression of z (see Eq. (2.2a)) approaches zero, thus making it difficult to retrieve z. However, in this case the value of n is stable. In this situation, instead of solving for n and z which exactly satisfy Eqs. (2.1), we solve for the following inequalities:

$$\left| S_{11} - \frac{R_{01}\left(1 - e^{i2nk_0 d}\right)}{1 - R_{01}^2 e^{i2nk_0 d}} \right| \leq \delta_r, \qquad (2.11\text{a})$$

$$\left| S_{21} - \frac{(1 - R_{01}^2) e^{ink_0 d}}{1 - R_{01}^2 e^{i2nk_0 d}} \right| \leq \delta_t, \qquad (2.11\text{b})$$

where δ_r and δ_t are small positive numbers. Fig. 2-5 shows the range of z satisfying Eqs. (2.11) for $\delta_r = 0.015$ and $\delta_t = 0.0$. At each frequency, all the z having a real and

imaginary parts between the bounds shown in Fig. 2-5 satisfy Eqs. (2.11). It can be seen that the magnitude of the spikes is within the tolerance error, which implies that they are due to the noise in the S_{11} and S_{21} data.
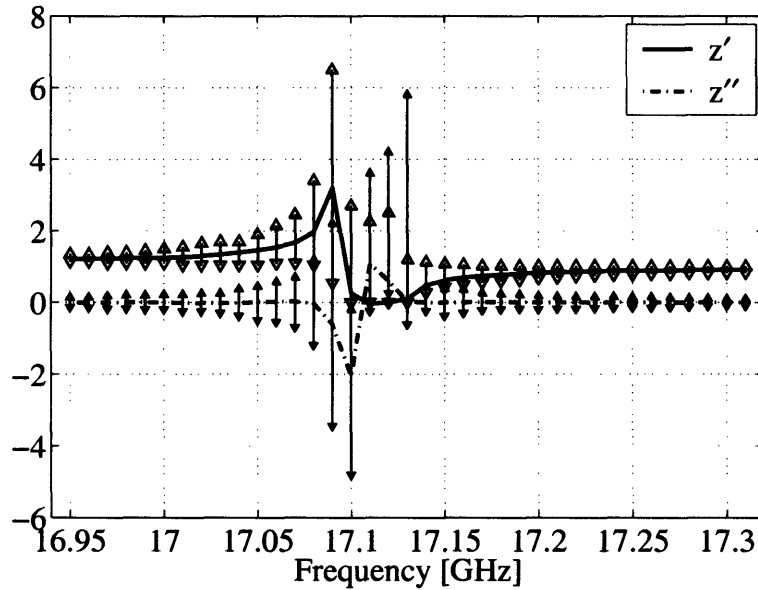
Figure 2-5: Range of z (real and imaginary parts) for tolerance $\delta_r = 0.015$ and $\delta_t = 0.0$ in Eqs. (2.11). The impedance is for a 3-cell metamaterial shown in Fig. 2-1.

Finally, note that although the retrieved n and z for multiple cells may be different from that for one cell at some specific frequencies, the calculated S_{11} and S_{21} for multiple cells using the retrieved ϵ and μ from one cell data match well with the S_{11} and S_{21} data computed for multiple cells directly from numerical simulation, as is illustrated in Fig. 2-6.

2.2.6 Results

The retrieved permittivity ϵ and permeability μ of a one-cell of SRR-rod structure of Fig. 2-1 are shown in Fig. 2-7. Note that although the results satisfy the condition $\epsilon'' \geq 0$ and $\mu'' \geq 0$, the positive energy requirement $\partial(\epsilon\omega)/\partial\omega > 0$ [84, 2] is violated in the frequency band 12 GHz $\sim$ 12.2 GHz. As a result, the resonance band is extended to 11 GHz $\sim$ 12.2 GHz, as shown by the vertical dashed lines in Fig. 2-7(a). The value of ϵ and μ are both negative in the frequency range 12.2 GHz $\sim$ 12.8 GHz, showing that in this band, the metamaterial exhibits a left-handed behavior. We also retrieved the effective parameters of
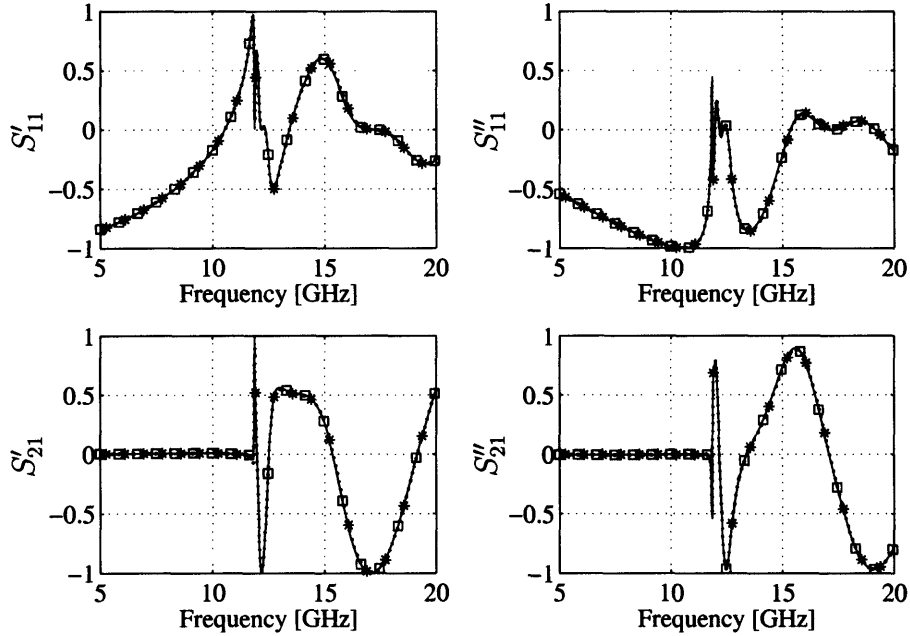
Figure 2-6: S_{11} and S_{21} (real and imaginary parts) for 3 cells: comparison between FDTD results (dot line with $*$) and calculated S parameters based on the retrieved ϵ and μ (solid line with $\square$) for a one-cell metamaterial shown in Fig. 2-1.

4 and 5 cells of metamaterial shown in Fig. 2-1, and the retrieval results are close to those for 1, 2, and 3 cells.

In addition, we also applied our method to retrieve the effective parameters of the structure taken from [82, 83], as shown in the inset of Fig. 2-8(a). For a 1D structure, by matching the impedance z for 1 and 2 cells of the metamaterial using the previously described method, we obtain $\overline{x}_{opt} = (2.2053 \times 10^{-3}d_0, 1.1356 \times 10^{-3}d_0)$, where d_0 is the length of unit cell. Again, we find that the two boundaries of the effective homogeneous medium are close to the outer unit cell boundaries of the 1D metamaterial. Fig. 2-8 shows the retrieved z, n, ϵ and μ for 1 cell of this metamaterial. It can be seen that the frequencies range 13.8 GHz $\sim$ 14.5 GHz is a left-handed band, which agrees with the conclusion in [82]. It should be noted, however, that for a 2D version of this metamaterial, the effective boundaries should be obtained from the optimization process, as they do not necessarily match the unit cell boundaries of the metamaterial.

2.2.7 Estimation of the error

In this section, we estimate the error of the retrieved n and z due to the noise contained in the S parameters. For a metamaterial, the S parameters calculated from FD-TD contain noise, but we do not know the exact value of z and n to compare with in order to estimate the error of the retrieved solution. Therefore, we choose a slab of a homogeneous medium with analytical ϵ and μ, which is used to compare with the retrieved results in the presence of the noise.

Consider a slab of homogeneous medium with the following constitutive parameters:

$$\epsilon = 1 - \frac{f_{pe}^2}{f^2 + i\gamma_e f}, \tag{2.12a}$$

$$\mu = 1 - \frac{f_{pm}^2}{f^2 - f_{0m}^2 + i\gamma_m f}, \tag{2.12b}$$

where $f_{pe} = 10$ GHz, $\gamma_e = 0.2$ GHz, $f_{pm} = 9$ GHz, $f_{0m} = 8$ GHz, and $\gamma_m = 1.0$ GHz.

The thickness of the slab is 0.01 (m), and the operating frequency ranges from 3 GHz to 15 GHz.

The refractive index n and the impedance z are functions of S_{11} and S_{21}, as shown in Eqs. (2.1). In what follows, we estimate the errors in the retrieved n and z in the presence of noise.

Applying a Taylor expansion of the first order to Eqs. (2.1), we approximately obtain the errors of the retrieved n and z due to the errors contained in the S parameters.

$$\begin{aligned}
\Delta z &\approx \frac{\partial z}{\partial S_{11}}\Delta S_{11} + \frac{\partial z}{\partial S_{21}}\Delta S_{21} \\
&= A_{11}\Delta S_{11} + A_{21}\Delta S_{21}
\end{aligned} \tag{2.13}$$

where

$$A_{11} = \frac{1}{z}\frac{2(1 - S_{11}^2 - S_{21}^2)}{[(1 - S_{11})^2 - S_{21}^2]^2}, \tag{2.14a}$$

$$A_{21} = \frac{1}{z} \frac{4S_{11}S_{21}}{[(1 - S_{11})^2 - S_{21}^2]^2}. \tag{2.14b}$$

Separating the real and the imaginary parts, we have

$$\Delta z' = A'_{11}\Delta S'_{11} - A''_{11}\Delta S''_{11} + A'_{21}\Delta S'_{21} - A''_{21}\Delta S''_{21} \tag{2.15a}$$

$$\Delta z'' = A'_{11}\Delta S''_{11} + A''_{11}\Delta S'_{11} + A'_{21}\Delta S''_{21} + A''_{21}\Delta S'_{21} \tag{2.15b}$$

Thus, we obtain the bounds of error of z due to the errors contained in S_{11} and S_{21}:

$$|\Delta z'| \leq |A'_{11}\Delta S'_{11}| + |A''_{11}\Delta S''_{11}| + |A'_{21}\Delta S'_{21}| + |A''_{21}\Delta S''_{21}| \tag{2.16a}$$

$$|\Delta z''| \leq |A'_{11}\Delta S''_{11}| + |A''_{11}\Delta S'_{11}| + |A'_{21}\Delta S''_{21}| + |A''_{21}\Delta S'_{21}| \tag{2.16b}$$

Similarly, we obtain the bounds of the error of n,

$$|\Delta n'| \leq |B'_{11}\Delta S'_{11}| + |B''_{11}\Delta S''_{11}| + |B'_{21}\Delta S'_{21}| + |B''_{21}\Delta S''_{21}|, \tag{2.17a}$$

$$|\Delta n''| \leq |B'_{11}\Delta S''_{11}| + |B''_{11}\Delta S'_{11}| + |B'_{21}\Delta S''_{21}| + |B''_{21}\Delta S'_{21}|, \tag{2.17b}$$

where

$$B_{11} = \frac{1}{k_0 d \sqrt{1 - X^2}} \left(-\frac{S_{11}}{S_{21}} \right) \tag{2.18a}$$

$$B_{21} = \frac{1}{k_0 d \sqrt{1 - X^2}} \left(\frac{1}{2} \frac{S_{11}^2 + S_{21}^2 - 1}{S_{21}^2} \right) \tag{2.18b}$$

and $X = \frac{1}{2S_{21}}(1 - S_{11}^2 + S_{21}^2)$.

In the numerical simulations, we retrieve the refractive index and impedance in the presence of five percent Gaussian noise in both the real and the imaginary parts of S_{11} and S_{21}. The retrieved and the true n and z, together with the lower and upper bounds from the error analysis are shown in Figs. 2-9 and 2-10.

It can be seen that the retrieved results in the presence of noise are within the lower and upper bounds at most of frequencies, which shows that the first order estimation of errors is efficient and accurate.

The retrieved permittivity and permeability are also shown in Fig. 2-11, where we ob-

serve that the retrieved permittivity and permeability randomly oscillate around the true solutions.

2.2.8 Some comments

There are some comments about the proposed retrieval method.

Limitation of the retrieval method

Although the proposed retrieval method works well at most of frequencies, it cannot retrieve the constitutive parameters of metamaterials around the resonance frequency (see the blocked frequency ranges in Fig. 2-4 and Fig. 2-7), which still remains an unsolved problem. For this issue, there are mainly two explanations in the literature. The first one is the existence of multiple modes in this region since the real part of n is large, yielding a wavelength comparable to or smaller than the unit size of the metamaterial thereby rendering the retrieval of the effective parameters of the metamaterials impossible [37, 38, 39]. The second explanation is that retrieval is possible in this case and the retrieved permittivity ϵ has a negative imaginary part in the resonance band [29, 40] state. In my opinion, I prefer the first explanation, and thus leave the retrieved results around the resonance blank, as shown in Figs. 2-4 and 2-7.

Dependence on the unit cell length

Note that for a given metamaterial structure, its effective constitutive parameters depend on the length of the unit cell, i.e., d_0 in Fig. 2-1. This property can be illustrated by the following example, periodic wire structure, where the ring is removed in Fig. 2-1. The study in [5] proves that the periodic metallic wires can be effectively modeled as a dilute plasma. When the length of the unit cell d_0 increases, the density of the electrons decreases, thus, the plasma frequency also decreases due to the fact that the plasma frequency is proportional to the square-root of the density of the electron.

2.3 Conclusion

We have proposed an improved method to retrieve the effective parameters (index of refraction, impedance, permittivity, and permeability) of metamaterials from transmission and reflection data. The successful retrieval results for various metamaterial structures show the effectiveness of the method. Our main conclusions are as follows:

1. The first boundary and the thickness of the effective media can be determined by matching z through all sample frequencies for different lengths of slabs in the propagation direction. For symmetric 1D metamaterials, we have drawn the empirical conclusion that the first boundary coincides with the first boundary of the unit cell facing the incident wave, and the thickness of the effective medium is approximately equal to the number of unit cells multiplied by the length of a unit cell. For 2D and asymmetric 1D metamaterials, the effective boundaries have to be determined by optimization.

2. The requirement $z' \geq 0$ cannot be used directly for practical retrievals when z' is close to zero because the numerical or measurement errors may flip the sign of z', making the result unreliable. In this case, we have to determine the sign of z by the value of its corresponding n so that $n'' \geq 0$.

3. There is a resonance band characterized by the fact that the requirement $\mu'' \geq 0$ and $\epsilon'' \geq 0$ cannot be satisfied at those frequencies. On each side of the resonance, the branch of n' can be obtained by a Taylor expansion approach considering the fact that the refractive index n is a continuous function of frequency. Since the refractive index n at the initial frequency determines the values of n' at the subsequent frequencies, we determine the branch of the real part of n at the initial frequency by requiring that μ'' and ϵ'' are non-negative across all the frequency band.

4. Due to the noise contained in the S parameters, the retrieved n and z at some specific frequencies are not reliable, especially for thicker metamaterials at lower frequencies. In spite of this, the fact that S_{11} and S_{21} for multiple cells of metamaterial calculated from the retrieved ϵ and μ for a unit cell metamaterial match the S_{11} and S_{21} computed directly from numerical simulation confirms that the metamaterials can be treated as an effective homogeneous material.

(a) Permittivity   (b) Permeability

Figure 2-7: Retrieved ϵ and μ (real and imaginary parts) for a one-cell metamaterial shown in Fig. 2-1. The vertical dashed lines denote the limits of the resonance band.
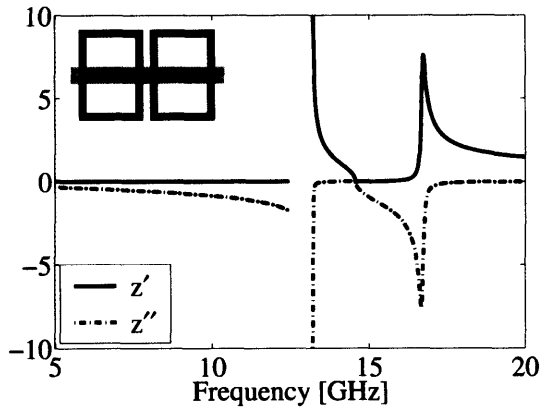
(a) Impedance
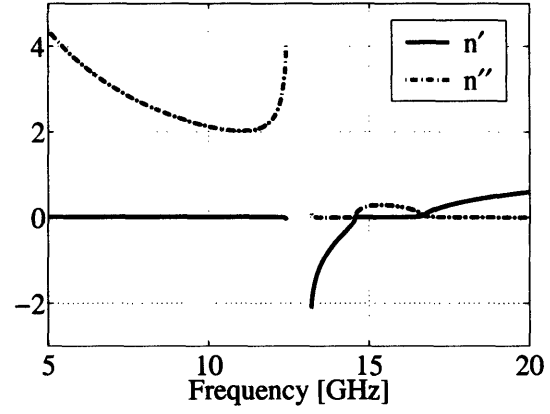
(b) Refractive index
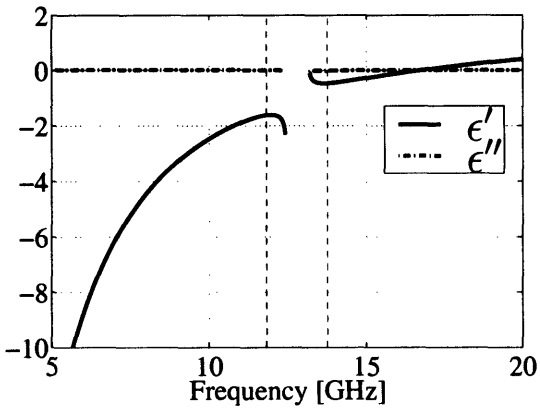
(c) Permittivity
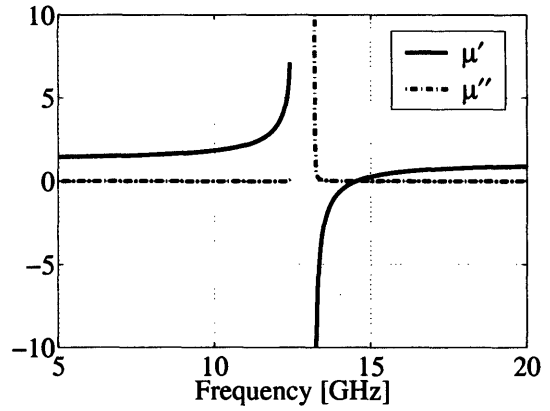
(d) Permeability

Figure 2-8: Retrieved z, n, ϵ and μ (real and imaginary parts) for a one-cell metamaterial structure taken from [82, 83] and shown in the inset of Fig. 2-8(a). The vertical dashed lines denote the limits of the resonance band.
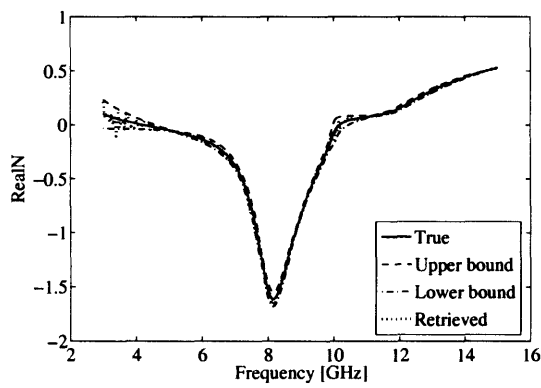
(a) Real part of n
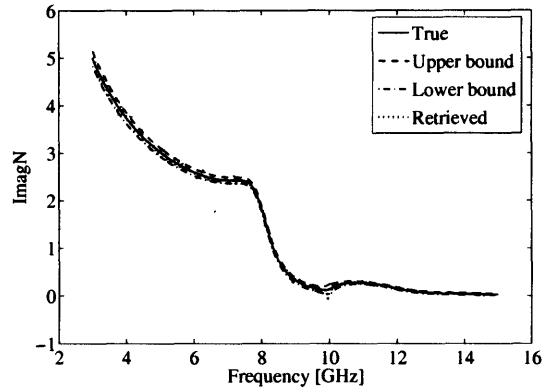
(b) Imaginary part of n

Figure 2-9: Comparison of the retrieved and the true results for n in the presence of five percent noise in S parameters.
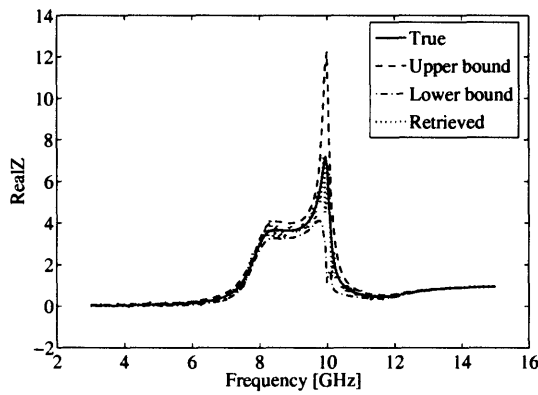
(a) Real part z
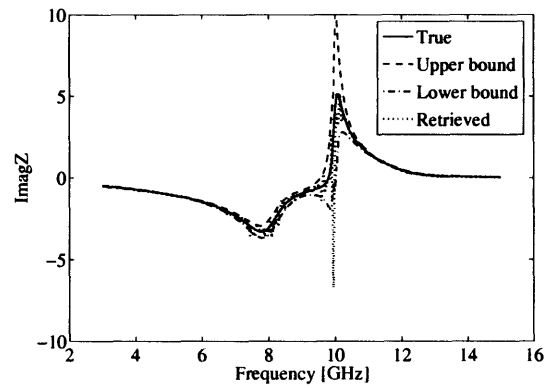
(b) Imaginary part of z

Figure 2-10: Comparison of the retrieved and the true results for z in the presence of five percent noise in S parameters.
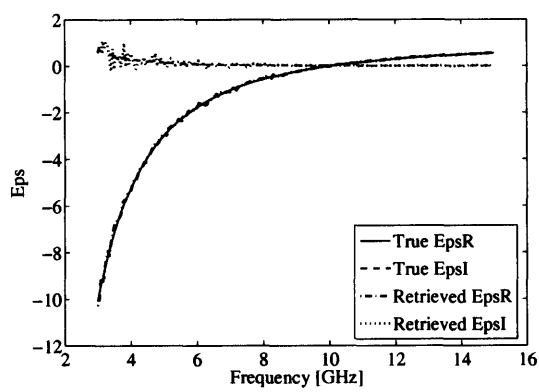
(a) Permittivity
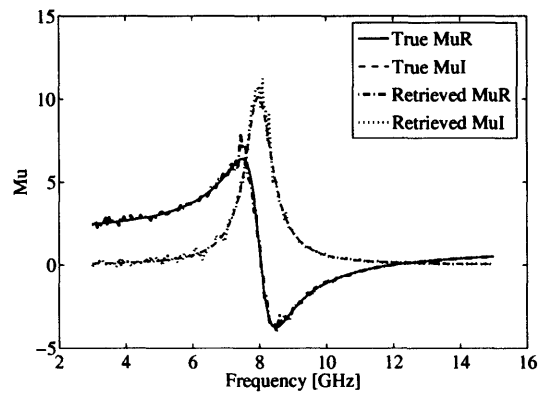
(b) Permeability

Figure 2-11: Comparison of the retrieved and the true results for ϵ and μ in the presence of five percent noise in S parameters.

Chapter 3

Retrieval of the bianisotropic metamaterial

3.1 Introduction

The retrieval methods applied to metamaterials as presented in the previous chapter and published so far [28, 29, 30] deal with isotropic permittivities and permeabilities. However, it is known already that the metamaterials are intrinsically anisotropic because of the orientations of the rings and rods in space, and that they are also possibly bianisotropic because of the specific properties of their split-rings. For example, it has been shown in [41, 42] that the original concentric split-ring exhibits a bianisotropic behavior, directly due to its geometry. Consequently, the existing retrieval algorithms need to be improved to take into account these additional properties.

In this chapter, we extend the work presented in the previous chapter and present a methodology to retrieve bianisotropic parameters as well. Although our approach is general, we derive it here for the specific retrieval of the bianisotropic term expected from the original concentric split-ring resonator [1], shown in Fig. 3-1(a). The SRR structure is made of two concentric rings, each interrupted by a small gap. For convenience, we refer to this SRR structure as the edge-coupled SRR [41]. It has been pointed out [43, 42] that this structure presents bianisotropy: The magnetic field in the $\hat{y}$ direction induces an electrical dipole in the $\hat{z}$ direction due to the asymmetry of the inner and outer rings, and the electric

47

field in the $\hat{z}$ direction, producing an unbalanced current distribution in the rings, induces a magnetic dipole in the $\hat{y}$ direction. Supposing that the medium is reciprocal [33, 44, 42, 84], the constitutive relationships can be written as

$$\overline{D} = \overline{\overline{\epsilon}} \cdot \overline{E} + \overline{\overline{\xi}} \cdot \overline{H}, \tag{3.1}$$

$$\overline{B} = \overline{\overline{\mu}} \cdot \overline{H} + \overline{\overline{\zeta}} \cdot \overline{E}, \tag{3.2}$$

where

$$\overline{\overline{\epsilon}} = \epsilon_0 \begin{pmatrix} \epsilon_x & 0 & 0 \\ 0 & \epsilon_y & 0 \\ 0 & 0 & \epsilon_z \end{pmatrix}, \overline{\overline{\mu}} = \mu_0 \begin{pmatrix} \mu_x & 0 & 0 \\ 0 & \mu_y & 0 \\ 0 & 0 & \mu_z \end{pmatrix},$$

$$\overline{\overline{\xi}} = \frac{1}{c} \begin{pmatrix} 0 & 0 & 0 \\ 0 & 0 & 0 \\ 0 & -i\xi_0 & 0 \end{pmatrix}, \overline{\overline{\zeta}} = \frac{1}{c} \begin{pmatrix} 0 & 0 & 0 \\ 0 & 0 & i\xi_0 \\ 0 & 0 & 0 \end{pmatrix}, \tag{3.3}$$

where ϵ_0 and μ_0 are the permittivity and permeability of free space respectively, and c is the speed of light in free space. Note that ϵ_x, ϵ_y, ϵ_z, μ_x, μ_y, μ_z, and ξ_0 are all dimensionless quantities. Since there are seven complex unknowns to be determined, at least seven equations are required. In order to obtain these, we resort to multiple incidences as shown in Fig. 3-1(b), where each incidence gives two complex equations, one for the reflection (S_{11}) and and the other one for the transmission (S_{21}).

We propose a method to retrieve the above-mentioned constitutive parameters of a homogeneous material from the measured S parameters. The analytical inversion equations are proposed for homogeneous lossless bianisotropic media, and a numerical retrieval approach is presented for the case of lossy bianisotropic media. Both methods are verified by numerical examples, where analytical ϵ, μ and ξ_0 are supposed and are retrieved from the S parameters. Finally, we use the retrieval method to study the properties of various SRR-based metamaterials. The retrieval results corroborate the conclusions found in the previously published work [41, 42, 45, 43].

Although the retrieval method proposed in this chapter is used to retrieve the constitu-

48
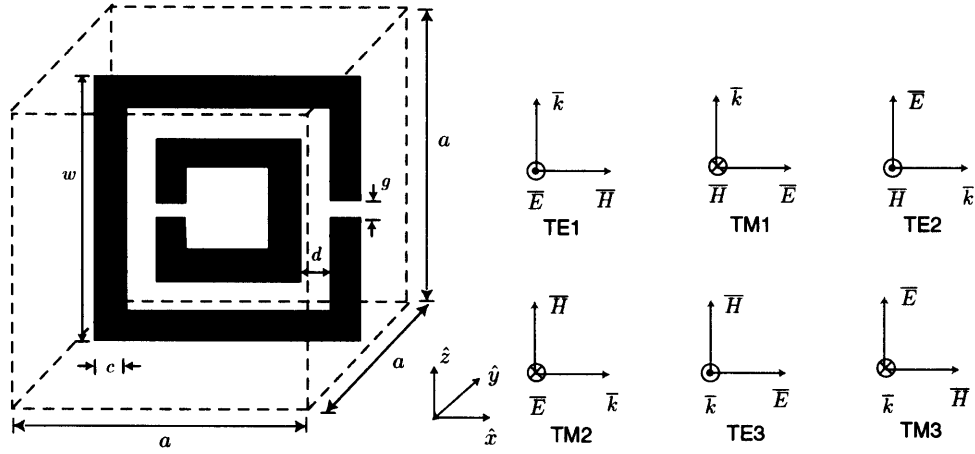
(a) Structure of the edge-coupled SRR: The unit cell is a cube of edge $a = 5.25$ mm. The parameters of the SRR are $g = d = 0.125$ mm, $c = 0.25$ mm, and $w = 3.75$ mm. The background medium is free space.

(b) Modes of multiple incidences: When the wave is incident normally on the unit cell, the unit cell is periodically repeated in the plane perpendicular to the incidence direction, thus forming a slab.

Figure 3-1: Unit cell of the metamaterial composed of the edge-coupled SRR upon which six incidences are used to obtain the S parameters from finite-difference time-domain simulations.

tive parameters of media with the bianisotropy in the yz position (see Eq. (3.3)), it can be easily generalized to retrieve the constitutive parameters of a medium with the bianisotropy coupling other field components. Therefore, a general analysis tool can be constructed for the study of the bianisotropic properties of metamaterials.

3.2 Retrieval methods

In this section, we present the retrieval equations for media described by Eq. (3.3) from the knowledge of the S parameters. Two main cases are identified: if the medium is lossless or if it is lossy. In the former case, the retrieved constitutive parameters can be obtained analytically while in the later case, although the equations are analytical, their solution has to be obtained numerically. Among the six incidences desired as shown in Fig. 3-1(b), three are TE modes and three are TM modes. The definition of TE and TM is as follows:

The plane of incidence is chosen to be $xy/yz/zx$ plane for incidence in the $x/y/z$ direction, respectively. Note that the S parameters are defined in terms of the electric and magnetic fields for the TE and TM incidences, respectively. We see from Eqs. (3.1) and (3.3) that only the y component of $\overline{H}$ contributes to $\overline{D}$, and similarly only the z component of $\overline{E}$ contributes to $\overline{B}$. Thus, among the six incidences, only TM1, TE2, and TM3 see the bianisotropy, while the other three waves are propagating as if the material were isotropic. The incidence TE2, containing both H_y and E_z, is more complicated than all the other incidences and the retrieval method in this case has to be studied independently.

3.2.1 Incidences other than TE2

As mentioned above, the incidence TE2 is very particular, and we shall study it in the next section. We show here that all the other incidences share the same retrieval equations, upon properly defining the effective impedance and the refractive index. For each incidence, the dispersion relationship, together with the redefined impedance and refractive index, is listed in Table 3.1.

Since the incidences TE1, TM2 and TE3 do not contain H_y or E_z components that cause the bianisotropy, they behave as if the medium were isotropic. In order to retrieve the constitutive parameters in these cases, we use the previously published retrieval methods that deal with isotropic media [28, 30, 29, 46]. The S parameters for a plane wave incident normally on a slab of an isotropic medium are expressed by [33, 7]

$$S_{11} = \frac{R_{01}\left(1 - e^{i2nk_0 d}\right)}{1 - R_{01}^2 e^{i2nk_0 d}}, \tag{3.4a}$$

$$S_{21} = \frac{(1 - R_{01}^2)e^{ink_0 d}}{1 - R_{01}^2 e^{i2nk_0 d}}, \tag{3.4b}$$

where k_0 denotes the wavenumber of the incidence wave in free space, d is the thickness of the slab, n is the refractive index, $R_{01} = (z - 1)/(z + 1)$ is the half-space reflection coefficient, and z is the impedance and the admittance for TE and TM waves, respectively. The retrieval equations are [46]

Table 3.1: Dispersion relationship, redefined impedance and redefined refractive index for each incidence of Fig. 3-1(b).

Case	Dispersion relationship	z	n	Solved components
TE1	$k_z^2 = k_0^2 \epsilon_y \mu_x$	$\sqrt{\mu_x/\epsilon_y}$	$\sqrt{\epsilon_y \mu_x}$	ϵ_y, μ_x
TM1	$k_z^2 = k_0^2(\epsilon_x \mu_y - \frac{\epsilon_x}{\epsilon_z}\xi_0^2)$	$\frac{\epsilon_x}{\sqrt{\epsilon_x\mu_y - \frac{\epsilon_x}{\epsilon_z}\xi_0^2}}$	$\sqrt{\epsilon_x\mu_y - \frac{\epsilon_x}{\epsilon_z}\xi_0^2}$	ϵ_x
TE2	$k_x^2 = k_0^2(\epsilon_z\mu_y - \xi_0^2)$	$\frac{\mu_y}{\sqrt{\epsilon_z\mu_y - \xi_0^2 + i\xi_0}}$	$\sqrt{\epsilon_z\mu_y - \xi_0^2}$	
TM2	$k_x^2 = k_0^2\epsilon_y\mu_z$	$\sqrt{\epsilon_y/\mu_z}$	$\sqrt{\epsilon_y\mu_z}$	ϵ_y, μ_z
TE3	$k_y^2 = k_0^2\epsilon_x\mu_z$	$\sqrt{\mu_z/\epsilon_x}$	$\sqrt{\epsilon_x\mu_z}$	ϵ_x, μ_z
TM3	$k_y^2 = k_0^2(\epsilon_z\mu_x - \frac{\mu_x}{\mu_y}\xi_0^2)$	$\frac{\epsilon_z}{\sqrt{\epsilon_z\mu_x - \frac{\mu_x}{\mu_y}\xi_0^2}}$	$\sqrt{\epsilon_z\mu_x - \frac{\mu_x}{\mu_y}\xi_0^2}$	ϵ_z

$$z = \pm\sqrt{\frac{(1 + S_{11})^2 - S_{21}^2}{(1 - S_{11})^2 - S_{21}^2}}, \tag{3.5a}$$

$$e^{ink_0d} = X \pm i\sqrt{1 - X^2}, \tag{3.5b}$$

where $X = \frac{1}{2S_{21}}(1 - S_{11}^2 + S_{21}^2)$. The sign in Eq. (3.5) is determined by the conditions for passive media,

$$z' \geq 0, \tag{3.6a}$$

$$n'' \geq 0, \tag{3.6b}$$

where $(\cdot)\prime$ and $(\cdot)\prime\prime$ denote the real part and imaginary part operators, respectively. The issues of the effective boundaries and the branch cut of the real part of n are solved in the way descried in [46].

For incidences TM1 and TM3, we use the method proposed in [47, 48, 49] to calculate the S parameters, and find that they take the same form as in the isotropic case, provided that the impedance z and the refractive index n are properly redefined as shown in Table 3.1. Consequently, z and n for incidences TM1 and TM3 can also be retrieved using Eq. (3.5).

3.2.2 Incidence TE2

Since the incidence TE2 contains both H_y inducing an electric dipole in the $\hat{z}$ direction, and E_z inducing a magnetic dipole in the $\hat{y}$ direction, it shows stronger bianisotropy than

51

the incidences TM1 and TM3. The S parameters for incidence TE2 can be obtained by using the method presented in [47, 48], and their analytical expressions are as follows:

$$S_{11} = \frac{\frac{\mu_y - k_x/k_0 - i\xi_0}{\mu_y + k_x/k_0 + i\xi_0}\left(1 - e^{i2k_x d}\right)}{1 - \frac{(k_x/k_0 - \mu_y)^2 + \xi_0^2}{(k_x/k_0 + \mu_y)^2 + \xi_0^2}e^{i2k_x d}},$$ (3.7a)

$$S_{21} = \frac{\left(1 - \frac{(k_x/k_0 - \mu_y)^2 + \xi_0^2}{(k_x/k_0 + \mu_y)^2 + \xi_0^2}\right)e^{ik_x d}}{1 - \frac{(k_x/k_0 - \mu_y)^2 + \xi_0^2}{(k_x/k_0 + \mu_y)^2 + \xi_0^2}e^{i2k_x d}},$$ (3.7b)

where k_x is the wavenumber in the incidence direction inside the medium, and the dispersion relationship is given in Table 3.1. In general, we cannot define an impedance z and a refractive index n in order to simplify Eq. (3.7) and solve z and n analytically, like in the cases of incidences TM1 and TM3. Therefore, we resort to a numerical approach to solve for μ_y and ξ_0 in Eq. (3.7).

As mentioned previously, using six incidences yields 12 equations for seven unknowns to be solved. Five of the unknowns are therefore solved twice in this overdetermined problem. We see from Table 3.1 that ϵ_x, ϵ_y and μ_z are each retrieved twice. Also since ϵ_z is obtained from the incidence TM3, we solve for μ_y and ξ_0 twice using the following two methods:

Method 1

From the incidences TM1 and TM3, we obtain the expressions of μ_y and ξ_0:

$$\mu_y = \frac{\epsilon_x \mu_x z_{TM3}^2}{\epsilon_z z_{TM1}^2},$$ (3.8)

$$\xi_0^2 = \epsilon_z \mu_y \left(1 - \frac{\epsilon_z}{\mu_x z_{TM3}^2}\right),$$ (3.9)

where z_{TM3} denotes the redefined impedance in the case of incidence TM3 (other variables with the incidence mode in the subscript are defined similarly). There exist two roots of ξ_0^2, and the one that yields a better match between the calculated (by Eq. (3.7)) and the measured (or simulated) S parameters is identified as the correct ξ_0 value of the medium.

Method 2

We use an optimization approach to obtain ξ_0. For a given ξ_0, we have the following

relationship from the incidence TM3:

$$\mu_y = \frac{\xi_0^2}{\epsilon_z\left(1 - \frac{\epsilon_z}{\mu_{xz}z_{TM3}^2}\right)}.$$ (3.10)

Thus, the S parameters for the case TE2 can be calculated using Eq. (3.7) for the given ξ_0. The value of ξ_0 is obtained by optimizing its real and imaginary parts so that the calculated S parameters match the measured (or simulated) ones. The optimization method we are using here is the differential evolution algorithm [36].

While method 1 uses the TM1, TE2, and TM3 incidences to solve for μ_y and ξ_0, method 2 uses only TE2 and TM3 incidences. Yet, we expect these two different mathematical approaches to yield the same retrieval results, which will be shown later in the numerical verification.

3.2.3 Incidence TE2: Lossless media

It is worth mentioning that there is an analytical approach to solve for μ_y and ξ_0 in a special case. When the wavenumber k_x and the constitutive parameters are real numbers, which refers to a propagating wave inside a lossless medium, it can be shown that the S parameters in Eq. (3.7) reduce to

$$S_{11} = \frac{R_{01}\left(1 - e^{i2nk_0d}\right)}{1 - |R_{01}|^2 e^{i2nk_0d}},$$ (3.11a)

$$S_{21} = \frac{(1 - |R_{01}|^2)e^{ink_0d}}{1 - |R_{01}|^2 e^{i2nk_0d}},$$ (3.11b)

where the refractive index n and the impedance z are redefined as in Table 3.1. For convenience, we call the retrieval method in this case a lossless retrieval, while the retrieval method in the previous section is referred to as a lossy retrieval. In what follows, we solve for n and z by inverting Eq. (3.11) as:

$$\frac{S_{11}}{S_{21}} = \left(e^{ink_0d} - e^{-ink_0d}\right)\frac{R_{01}}{|R_{01}|^2 - 1},$$ (3.12a)

$$\frac{1}{S_{21}} = e^{ink_0d} + \left(e^{ink_0d} - e^{-ink_0d}\right)\frac{1}{|R_{01}|^2 - 1}.$$ (3.12b)

Eliminating $e^{ink_0 d} - e^{-ink_0 d}$, we find

$$e^{ink_0 d} = \frac{R_{01} - S_{11}}{S_{21} R_{01}}.$$ (3.13)

Plugging Eq. (3.13) into Eq. (3.12a), and using $|R_{01}|^2 = R_{01} R_{01}^*$, we eventually obtain the value of z as:

$$z' = \sqrt{\frac{DC'' - B'}{A'} - \frac{D^2}{4}},$$ (3.14a)

$$z'' = \frac{1}{2} D,$$ (3.14b)

where

$$A = 2S_{11} - (S_{11}^2 + 1 - S_{21}^2),$$ (3.15a)

$$B = 2S_{11} + (S_{11}^2 + 1 - S_{21}^2),$$ (3.15b)

$$C = S_{11}^2 + S_{21}^2 - 1,$$ (3.15c)

$$D = \frac{A'' B' - A' B''}{A'' C'' + A' C'}.$$ (3.15d)

Once z is obtained, n can be solved via Eq. (3.13). Similarly to the lossy case, we have two different methods to solve for μ_y and ξ_0 in the lossless case.

Method 1

The component μ_y is calculated from the incidences TM1 and TM3, as shown in Eq. (3.8). From z_{TE2} listed in Table 3.1, we obtain

$$\xi_0 = \frac{1}{2i} \left(\frac{\mu_y}{z_{TE2}} - \epsilon_z z_{TE2} \right).$$ (3.16)

Method 2

From the results for the cases TE2 and TM3, we get

$$\mu_y = \frac{n_{TE2}^2 \mu_x z_{TM3}^2}{\epsilon_z^2}$$ (3.17)

Consequently, the value of ξ_0 is calculated using Eq. (3.16).

54

3.3 Numerical validation

The retrieval equations presented in the previous section have first been validated using analytical models. In this process, a slab of a given thickness is assigned the constitutive parameters of Eq. (3.3), where each component of the constitutive tensors is described by a frequency dispersive model (or by a positive constant in some cases), either lossy or lossless. The S-parameters are computed analytically, and are used as input to the retrieval algorithms. The retrieved parameters are obviously expected to match exactly the input functions.

Retrieval for lossless media

For a lossless medium, the constitutive parameters are chosen to follow the form proposed in [42] (Note the difference in the coordinate systems used in this chapter and in [42]),

$$\epsilon_x(f) = C_1,$$

$$\epsilon_z(f) = \epsilon_x + C_2(f_0^2/f^2 - 1)^{-1},$$

$$\mu_y(f) = 1 + C_3(f_0^2/f^2 - 1)^{-1},$$

$$\xi_0(f) = C_4 f_0/f \left(f_0^2/f^2 - 1\right)^{-1},$$

$$\epsilon_y(f) = \mu_x(f) = \mu_z(f) = 1,$$

where the coefficients are chosen arbitrarily to be $C_1 = 1.5$, $C_2 = 1.0$, $C_3 = 2.0$, $C_4 = 0.5$, and $f_0 = 5.0$ GHz.

The constitutive parameters are retrieved using the lossless retrieval method presented in the previous section. For the non-dispersive components, the retrieval results agree exactly with the above given values. For the dispersive components, the retrieved results are compared with the analytical ones in Fig. 3-2. The retrieval results near the resonance are divergent and become numerically unstable, thus they are not shown here. Slightly away from this resonant region, however, the retrieved results are in perfect agreement with the input functions, which validates the proposed lossless retrieval method.

(a) ϵ_z

(b) μ_y
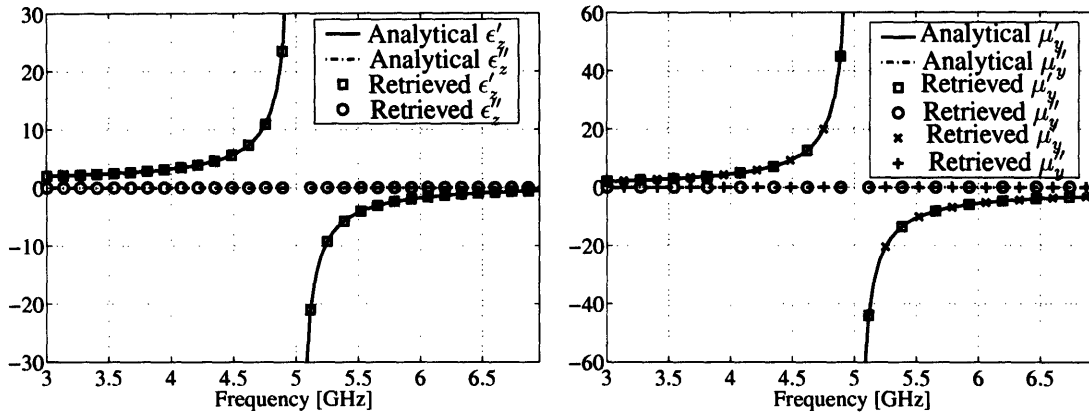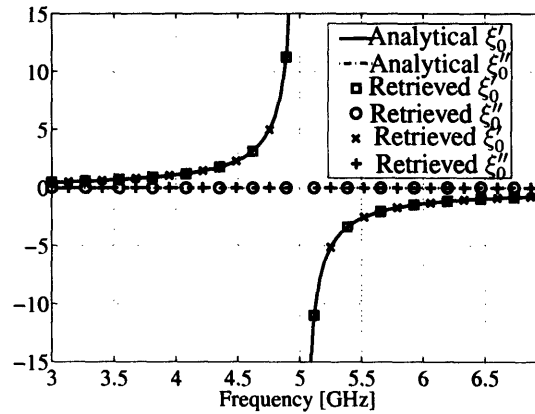
(c) ξ_0

Figure 3-2: Comparison of the analytical and the retrieved results for a lossless homogeneous medium. The curves with □ and ○ are the retrieval results using method 1, and the curves with × and + are from method 2. Note that the markers in the figure are hard to distinguish because the results are almost identical for the two methods.

Retrieval for Lossy media

In order to prove the validity of the proposed retrieval method for lossy media, we retrieve the constitutive parameters of the following homogeneous lossy bianisotropic medium

$$\epsilon_x(f) = C_1,$$

$$\epsilon_z(f) = 1 - F_e f^2/(f^2 - f_e^2 + i\gamma_e f),$$

$$\mu_y(f) = 1 - F_m f^2/(f^2 - f_m^2 + i\gamma_m f),$$

$$\xi_0(f) = 1 - F_\xi f^2/(f^2 - f_\xi^2 + i\gamma_\xi f),$$

$$\epsilon_y(f) = \mu_x(f) = \mu_z(f) = C_2.$$

Here we choose arbitrarily $C_1 = 2.0$, $C_2 = 1$, $f_e = 6.0\,\text{GHz}$, $f_m = f_\xi = 5.0\,\text{GHz}$, $\gamma_e = 0.4$ GHz, $\gamma_m = 0.2\,\text{GHz}$, $\gamma_\xi = 0.6\,\text{GHz}$, and $F_e = F_m = F_\xi = 0.4$.

The constitutive parameters are retrieved using the lossy retrieval method proposed previously. For the dispersive components, the retrieved results are compared with the analytical ones in Fig. 3-3, where a perfect agreement can be seen. It is worth mentioning that the losses avoid the divergence of ϵ_z, μ_y and ξ_0, which is advantageous for the retrieval algorithm.

3.4 Retrieval results for SRR-based metamaterials

The edge-coupled SRR-based metamaterial shown in Fig. 3-1(a) has been studied and proven to exhibit bianisotropy [41, 42], which has been corroborated by the studies in [45, 43]. In this section, we apply our retrieval method to a metamaterial composed of edge-coupled SRRs in order to quantify rigorously the magnitude of the bianisotropic term as a function of frequency. Note that the S parameters are calculated from FDTD simulation. The retrieval results show that the edge-coupled SRR structure indeed presents a strong bianisotropy, while a slight modification of it exhibits no bianisotropy, which agrees with the conclusion found in [41, 42].

(a) ϵ_z

(b) μ_y
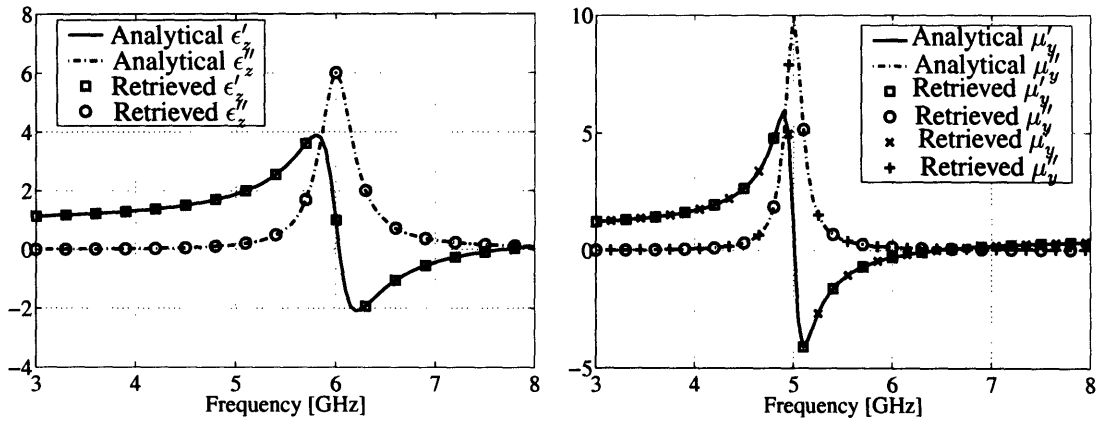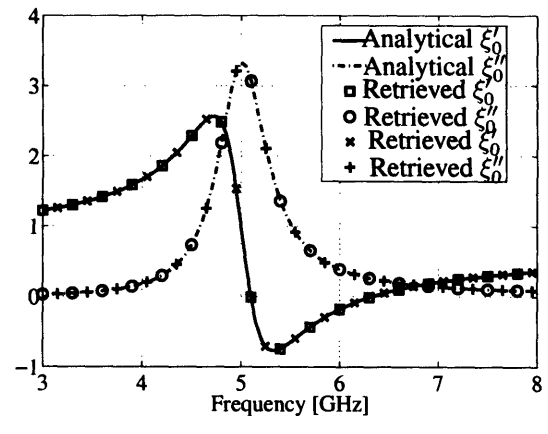
(c) ξ_0

Figure 3-3: Comparison of the analytical and the retrieved results for a lossy homogeneous medium. The curves with □ and ○ are the retrieval results using method 1, and the curves with × and + are from method 2. Note that the markers in the figure are hard to distinguish because the results are almost identical for the two methods.

3.4.1 Evidence of bianisotropy

In order to illustrate the necessity of using a retrieval method in which bianisotropy is considered, we first retrieve the effective constitutive parameters of an edge-coupled SRR metamaterial shown in Fig. 3-1(a) using the isotropic retrieval method [46]. Each component of the permittivity and the permeability tensor is retrieved exactly twice since an isotropic retrieval is carried out for each of the six incidences, where the S parameters are obtained using the periodic finite-difference time-domain method [50]. The retrieved results are shown in Fig. 3-4. While we observe good agreements in the retrieved μ_x, μ_z, ϵ_x, and ϵ_y (except around the resonance), there is a noticeable mismatch between the two retrieval methods for the parameters ϵ_z and μ_y, which indicates that the anisotropic model is not sufficient to describe the homogeneity of an edge-coupled SRR metamaterial shown in Fig. 3-1(a). Therefore, a better model is needed. Since the y component of the magnetic field produces an electric dipole in the $\hat{z}$ direction and the z component of the electric field produces a magnetic dipole in the $\hat{y}$ direction, the bianisotropy terms in Eq. (3.3) can not be neglected [42]. It is not surprise to see the unsuccessful retrieval of ϵ_z and μ_y, since ξ_0 is coupled with both of them in the incidences TM1, TE2 and TM3 (see Table 3.1).

When a lossless retrieval for bianisotropic media is applied, the retrieved μ_x, μ_z, ϵ_x and ϵ_y are identical to the ones shown in Fig. 3-4, while the retrieved ϵ_z, μ_y and ξ_0 are shown in Fig. 3-5. Unlike in the situation when an anisotropic retrieval is used, we observe a good match between the two retrieved values for both μ_y and ξ_0, except around the resonance frequencies, a range known to be hard to deal with in the retrieval of metamaterial's parameters [29, 46]. To show quantitatively a better match in Fig. 3-5, we define the relative mismatch (RM) of μ_y as

$$RM(\mu_y) = \begin{cases} 0 & \text{if } \frac{|\mu_{y1}|+|\mu_{y2}|}{2} < \alpha, \\ \frac{|\mu_{y1}-\mu_{y2}|}{\frac{1}{2}(|\mu_{y1}|+|\mu_{y2}|)} & \text{otherwise}, \end{cases} \tag{3.18}$$

where α is a small positive number. The smaller the RM, the better the matching between the two results. The relative mismatch for ϵ_z and ξ_0 can be defined similarly. We refer to the frequency where RM is larger than a constant β as the unsatisfactory matching frequency.

59
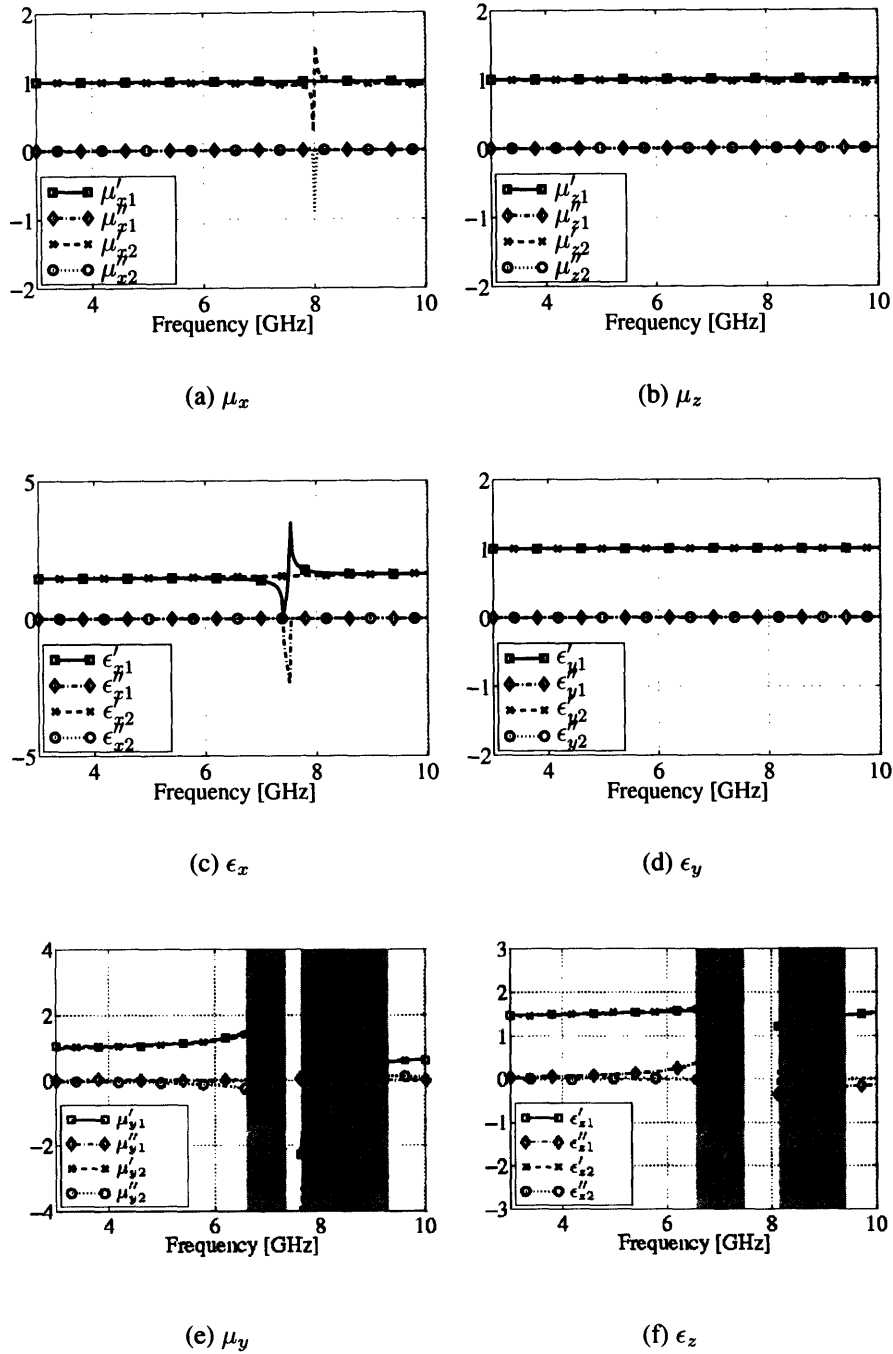
Figure 3-4: Retrieval results for a lossless edge-coupled SRR metamaterial whose unit cell is shown in Fig. 3-1(a), using a retrieval method not considering the bianisotropy. The retrieved μ_x (Fig. 3-4(a)) and ϵ_x (Fig. 3-4(c)) show negative imaginary parts around the resonance, which violates physical laws [84] and therefore indicates that the results are not reliable in the corresponding region. Those results difficult to read within the resonance band are not shown in Fig. 3-4(e) and Fig. 3-4(f). The shaded region indicates the frequency range where the mismatch of either μ_y or ϵ_z exceeds the threshold ($RM > 0.25$).

Table 3.2: Frequency ranges (in GHz) of unsatisfactory match for the retrieved μ_y, ϵ_z and ξ_0.

	For μ_y	For ϵ_z or ξ_0	Total Range
Fig. 3-4	6.9-9.3	6.6-8.5	6.6-9.3
Fig. 3-5	7.2-7.9, 8.1-8.5	7.2-7.5, 8.1-8.5	7.2-7.9, 8.1-8.5
Fig. 3-6	3.9-4.8	4.1-4.5	3.9-4.8
Fig. 3-7	5.9-6.7	6.0-6.5	5.9-6.7

For the parameter $\alpha = 0.25$ and $\beta = 0.25$, the unsatisfactory matching frequency ranges for μ_y, ϵ_z in Fig. 3-4 and μ_y, ξ_0 in Fig. 3-5 are listed in Table 3.2. The total unsatisfactory frequency range in which either μ_y or ϵ_z (or ξ_0) does not match well are also given in Table 3.2. We find that the unsatisfactory matching frequency range in Fig. 3-5 is narrower than that in Fig. 3-4.

Compared to [41, 42], we see that the shapes of the retrieved μ_y and ϵ_z agree with the models proposed in [41, 42], but that the resonances of ϵ_z and μ_y are not equal to each other (μ_y at 7.5 GHz, ϵ_z at 8.0 GHz). The fact that the two retrieval results now match well for both μ_y and ξ_0 and that the retrieved ξ_0 is not negligible proves the existence of the bianisotropy in the edge-coupled SRR metamaterial.

3.4.2 Lossy retrieval

Next, we apply the lossy retrieval method to retrieve the effective constitutive parameters of a lossy metamaterial. The SRR structure and the unit cell are same as shown in Fig. 3-1(a), but the whole unit cell is filled with a lossy material with the relative permittivity $\epsilon_r = 3.4$ and the conductivity $\sigma = 0.042$ S/m (yielding an imaginary part of ϵ of $0.01\epsilon_0$ at 7.5 GHz, the resonance frequency of the SRR structure, which is shown in Fig. 3-5). The retrieval results are shown in Fig. 3-6, where we observe a good match between the two retrieved values for both μ_y and ξ_0 (except around the resonance: $3.9 \sim 4.8$ GHz, see also Table 3.2). We also see noticeable imaginary parts in the retrieved parameters.

(a) μ_y

(b) ϵ_z

(c) ξ_0
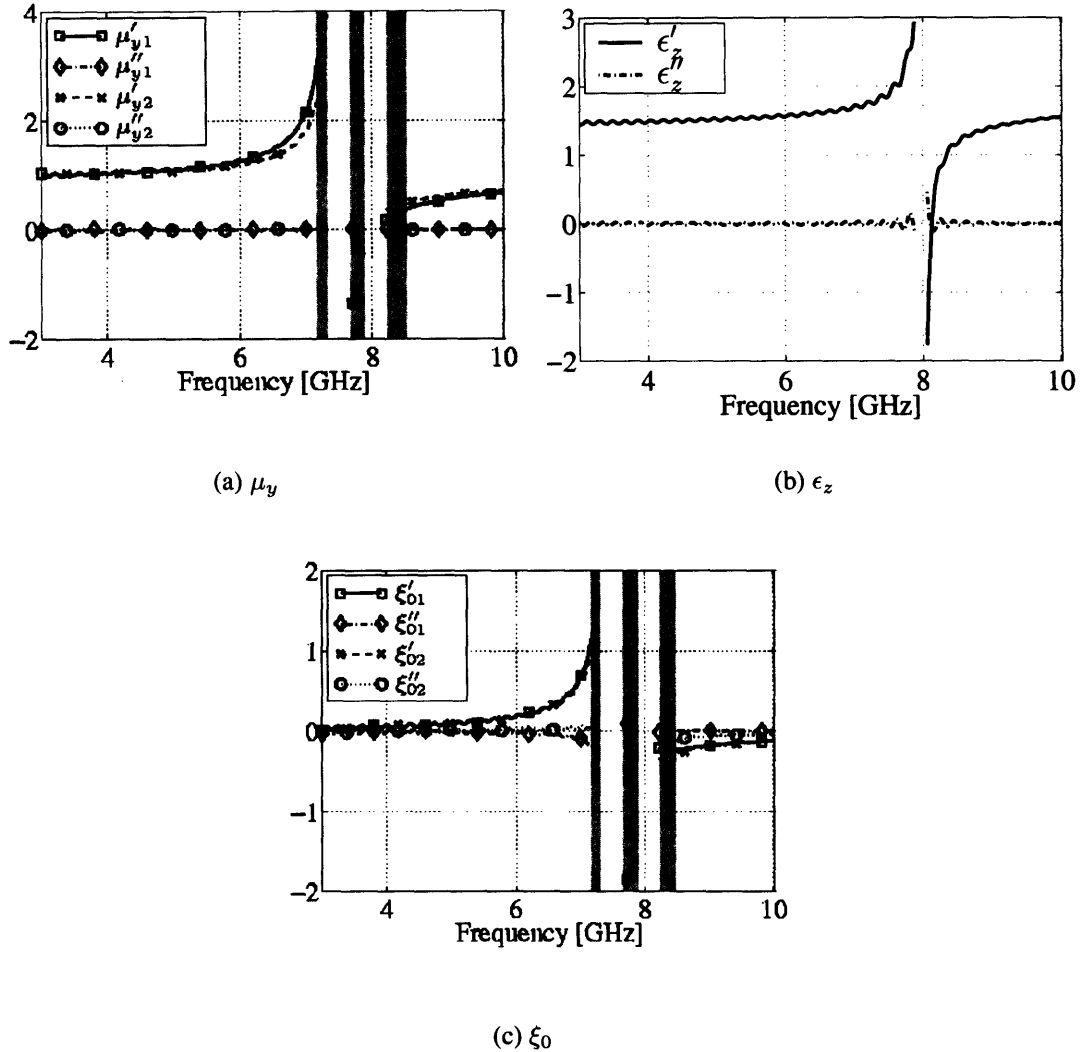
Figure 3-5: Retrieval results for a lossless edge-coupled SRR metamaterial whose unit cell is shown in Fig. 3-1(a), using a lossless retrieval for bianisotropic media. The subscripts '1' and '2' denote the results obtained from the proposed method 1 and method 2, respectively. Those results difficult to read within the resonance band are not shown here. The shaded region indicates the frequency range where the mismatch of either μ_y or ξ_0 exceeds the threshold ($RM > 0.25$).

(a) μ_y (b) ξ_0
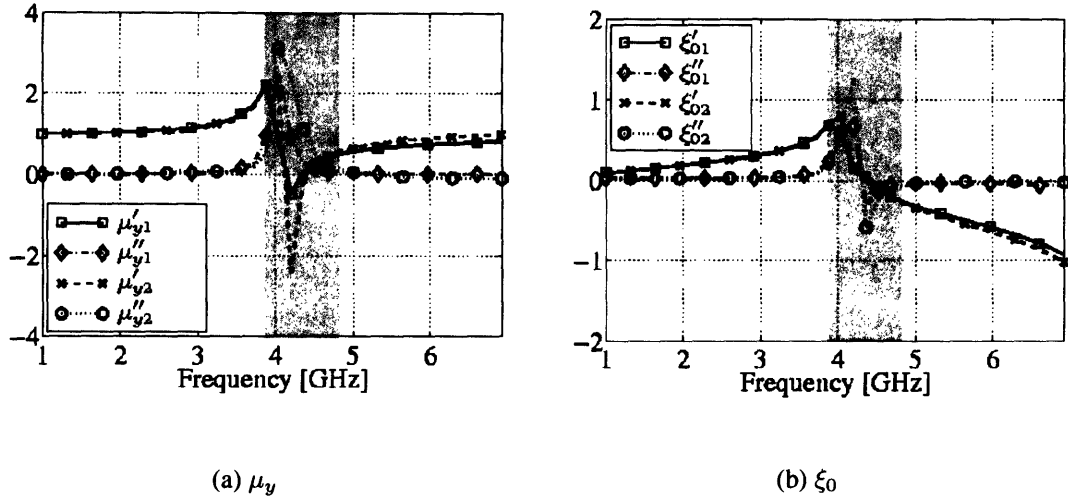
Figure 3-6: Retrieval results for a lossy edge-couple SRR metamaterial, whose unit cell is the same that in Fig. 3-1(a) except that the background material is lossy ($\sigma = 0.042$ S/m, $\epsilon_r = 3.4$). Those results difficult to read within the resonance band are not shown here. The shaded region indicates the frequency range where the mismatch of either μ_y or ξ_0 exceeds the threshold ($RM > 0.25$).

3.4.3   Retrieval of the broadside-coupled SRR metamaterial

The proposed retrieval method is a tool not only for studying the properties of bianisotropic media, but also for anisotropic media in which the retrieved bianisotropic term is expected to be close to zero. We retrieve here the effective constitutive parameters of a broadside-coupled SRR metamaterial, which is anisotropic as proposed in [41, 42]. The edge-coupled SRR shown in Fig. 3-1(a) can be slightly modified to be a broadside-coupled SRR (See Fig. 3 of [42]) by increasing the inner SRR to the size of the outer one and by separating the two rings by a certain distance (0.125 mm in our simulation). For this anisotropic structure, we expect to retrieve zero or negligible bianisotropy term using the proposed retrieval method.

Since there is no loss in the system, we apply the lossless retrieval method to obtain the results shown in Fig. 3-7. It is seen that the retrieved ξ_0 is close to zero in most frequencies except around the resonance, which agrees with the argument in [41, 42] that the broadside-coupled SRR does not present bianisotropy due to the symmetry of the electric charges and the currents. The successful retrieval results show that although the proposed retrieval

(a) μ_y (b) ξ_0
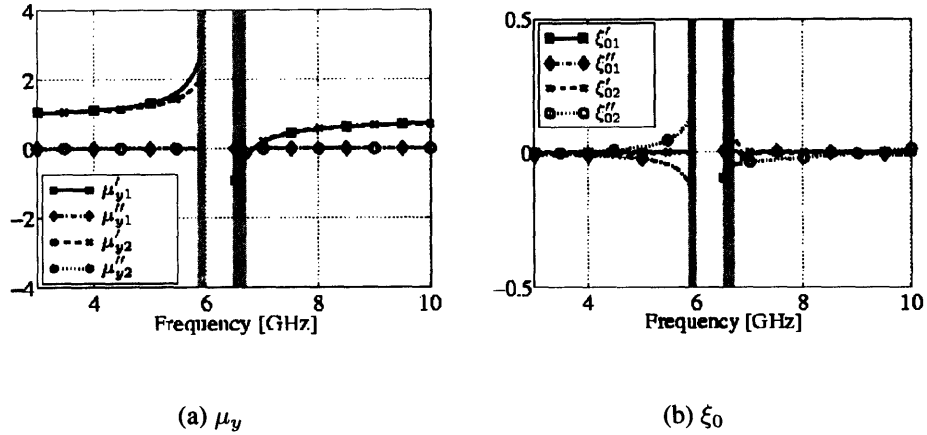
Figure 3-7: Retrieved results for a broadside-coupled SRR metamaterial, where a negligible ξ_0 is observed (except around the resonance: 5.9 GHz $\sim$ 6.7 GHz. See Table 3.2). Those results difficult to read within the resonance band are not shown here. The shaded region indicates the frequency range where the mismatch of either μ_y or ξ_0 exceeds the threshold ($RM > 0.25$).

method was initially constructed for the retrieval of bianisotropic media, it can also be applied to anisotropic media.

3.5 Conclusions

A useful tool is proposed to study the properties of bianisotropic metamaterials by retrieving their effective constitutive parameters from the measurements of the S parameters. Analytical inversion equations are proposed to retrieve the constitutive parameters of homogeneous lossless bianisotropic media, while a numerical approach is proposed for lossy bianisotropic media. Both methods have been first validated using analytical functions as input values for the constitutive parameters and second, using simulated S parameters of real split-ring structures. The retrieval results qualitatively corroborate the conclusions of previously published articles, proving the existence of the bianisotropy in the edge-coupled SRR metamaterials, but not in the broadside-coupled SRR metamaterials.

Chapter 4

Optimization approach to the retrieval of the constitutive parameters of a slab of general bianisotropic medium

4.1 Introduction

Constitutive parameters are important in quantitatively characterizing the wave propagation inside metamaterials [33, 44], but they are usually unknown to us. As stated in [51], the retrieval method from the reflection and transmission data as presented in the previous chapters is the prime approach in characterizing the constitutive parameters of metamaterials. While there are many approaches to retrieve their isotropic parameters [46, 28, 30], only [52] deals with the retrieval of the bianisotropic parameters. It should be noted, however, that in this study, the cross-polarization properties of the medium are known a priori, which is the reason why a semi-analytical solution could be developed. For more complicated metamaterial structures, the cross-polarization properties remain unknown and a more general retrieval method is needed.

This chapter presents a method to retrieve the constitutive parameters of a general bianisotropic slab from the knowledge of the reflection and transmission matrix via an optimization approach. Note that each of the permittivity tensor $(\bar{\bar{\epsilon}})$, permeability tensor $(\bar{\bar{\mu}})$,

and cross-polarization tensors $(\bar{\bar{\xi}}, \bar{\bar{\zeta}})$ is a three by three matrix with complex elements, so that there are 72 parameters to be retrieved. While many methods have been proposed to retrieve specific bianisotropic media in the literature [53, 54, 55], only [56], to be best on the author's knowledge, deals with the retrieval of general bianisotropic media. However, the optimization method proposed in [56] is based on the conjugate gradient, a deterministic method, which often gives local-minima solution. In this chapter, differential evolution (DE) and simplex optimization methods are used in order to obtain the global-minimum solution. In the optimization, we minimize the relative mismatch between the measured reflection/transmission data and the calculated ones from the forward approach, where the reflection and transmission coefficients for a plane weave obliquely or normally incident upon a slab in free space are calculated by the notion of propagators and wave-splitting technique [48].

The proposed method is applied for to not only general media with unknown constitutive properties, but also media with known constitutive properties. In our numerical validation, we first apply our method to the retrieval of a rotated biaxial medium, where 15 parameters need to be optimized. Then we retrieve a rotated omega medium, where 17 parameters need to be optimized. Finally, we apply the proposed method to the retrieval of two general bianisotropic media, where 72 parameters are optimized. In all the cases, we obtain a group of solutions, instead of a single one. The fact that all the obtained solutions are close to the true one shows the robustness of the proposed optimization method.

4.2 Problem formulation and forward approach

Consider a time-harmonic electromagnetic plane wave obliquely (or normally) impinging from the region $z < 0$ onto a homogeneous slab located in the region $z \in [0, d]$. Both sides of the slab are free space. The incident wave vector $\bar{k}_i$ is expressed as $\bar{k}_i = (\hat{x} \sin\theta \cos\phi + \hat{y} \sin\theta \sin\phi + \hat{z} \cos\theta)k_0$, where $\theta \in [0, \pi/2]$ and ϕ are the polar and azimuthal angle of the incident wave, respectively, and k_0 denotes the wave number in free space.

The homogeneous slab is characterized by the electromagnetic parameters $\bar{\bar{\epsilon}}, \bar{\bar{\mu}}, \bar{\bar{\xi}}$, and $\bar{\bar{\zeta}}$, and its constitutive relationships are

$$\overline{D} = \overline{\overline{\epsilon}} \cdot \overline{E} + \overline{\overline{\xi}} \cdot \overline{H}, \tag{4.1}$$

$$\overline{B} = \overline{\overline{\mu}} \cdot \overline{H} + \overline{\overline{\zeta}} \cdot \overline{E}, \tag{4.2}$$

Note that we do not assume anything on $\overline{\overline{\epsilon}}, \overline{\overline{\mu}}, \overline{\overline{\xi}},$ and $\overline{\overline{\zeta}}$, which are taken to be fully populated complex tensors, yielding 72 unknown real parameters.

In the forward problem, the reflection and transmission coefficients are calculated by the notion of propagators and wave-splitting technique [48]. Inside the slab, the tangential electric and magnetic fields satisfy the following equations,

$$\frac{d}{dz} \begin{pmatrix} \overline{E}_{xy}(z) \\ \eta_0 \overline{\overline{J}} \cdot \overline{H}_{xy}(z) \end{pmatrix} = ik_0 \overline{\overline{M}}(z) \begin{pmatrix} \overline{E}_{xy}(z) \\ \eta_0 \overline{\overline{J}} \cdot \overline{H}_{xy}(z) \end{pmatrix} \tag{4.3}$$

Upon integrating, we map the field on the left-hand side boundary ($z = 0$) to the right-hand side boundary ($z = d$) as

$$\begin{pmatrix} \overline{E}_{xy}(d) \\ \eta_0 \overline{\overline{J}} \cdot \overline{H}_{xy}(d) \end{pmatrix} = \overline{\overline{P}} \cdot \begin{pmatrix} \overline{E}_{xy}(0) \\ \eta_0 \overline{\overline{J}} \cdot \overline{H}_{xy}(0) \end{pmatrix} \tag{4.4}$$

where

$$\overline{\overline{P}} = e^{ik_0 d \overline{\overline{M}}} \tag{4.5}$$

is known as the propagator, and $\overline{\overline{M}}$, a function of $\overline{\overline{\epsilon}}, \overline{\overline{\mu}}, \overline{\overline{\xi}},$ and $\overline{\overline{\zeta}}$, is the fundamental dyad of the bianisotropic medium whose explicit expression can be found in [48]. In both sides of the slab, the wave splitting technique is used in free space,

$$\begin{cases} \overline{E}_{xy}(z) = \overline{E}^+(z) + \overline{E}^{-1}(z) \\ \eta \overline{\overline{J}} \cdot \overline{H}_{xy}(z) = -\overline{\overline{O}}^{-1} \cdot \overline{E}^+(z) + \overline{\overline{O}}^{-1} \cdot \overline{E}^-(z) \end{cases} \tag{4.6}$$

where

$$\overline{\overline{O}} = \hat{e}_\parallel \hat{e}_\parallel \cos\theta_i + \hat{e}_\perp \hat{e}_\perp \frac{1}{\cos\theta_i} \tag{4.7}$$

is assimilated to an impedance dyad, where $\hat{e}_\parallel$ is the unit vector in the direction of the pro-

jection of $\overline{k}_i$ onto the (xy) plane and $(\hat{e}_{\parallel}, \hat{e}_{\perp}, \hat{z})$ forms the basis of an orthogonal coordinate system.

By combining Eqs. (4.4) and (4.6), we obtain the scattering relation,

$$
\begin{pmatrix} \overline{E}^+(d) \\ \overline{E}^-(d) \end{pmatrix} = \overline{\overline{T}} \cdot \begin{pmatrix} \overline{E}^+(0) \\ \overline{E}^-(0) \end{pmatrix}
\tag{4.8}
$$

where

$$
\overline{\overline{T}} = \frac{1}{2} \begin{pmatrix} \overline{\overline{I}}_2 & -\overline{\overline{O}} \\ \overline{\overline{I}}_2 & \overline{\overline{O}} \end{pmatrix} \cdot \begin{pmatrix} \overline{\overline{P}}_{11} & \overline{\overline{P}}_{12} \\ \overline{\overline{P}}_{21} & \overline{\overline{P}}_{22} \end{pmatrix} \cdot \begin{pmatrix} \overline{\overline{I}}_2 & \overline{\overline{I}}_2 \\ -\overline{\overline{O}} & \overline{\overline{O}} \end{pmatrix}
\tag{4.9}
$$

The reflection and transmission dyads for the tangential electric field are defined by

$$
\begin{cases} \overline{\overline{r}} = -\overline{\overline{T}}_{22}^{-1} \cdot \overline{\overline{T}}_{21} \\ \overline{\overline{t}} = \overline{\overline{T}}_{11} + \overline{\overline{T}}_{12} \cdot \overline{\overline{r}} \end{cases}
\tag{4.10}
$$

In terms of the strengths of the fields of TE and TM waves, the reflection and transmission coefficients are defined to be

$$
r_{EE} = r_{22}, \quad r_{EM} = r_{21} \cos\theta_i, \quad r_{ME} = -r_{12}/\cos\theta_i, \quad r_{MM} = -r_{11}
\tag{4.11}
$$

$$
t_{EE} = t_{22}, \quad t_{EM} = t_{21} \cos\theta_i, \quad t_{ME} = t_{12}/\cos\theta_i, \quad t_{MM} = t_{11}
\tag{4.12}
$$

and the reflection and transmission tensors in terms of the fields strengths are

$$
\overline{\overline{r}} = \begin{pmatrix} r_{EE} & r_{EM} \\ r_{ME} & r_{MM} \end{pmatrix}, \quad \overline{\overline{t}} = \begin{pmatrix} t_{EE} & t_{EM} \\ t_{ME} & t_{MM} \end{pmatrix}
\tag{4.13}
$$

The results obtained by the aforementioned method have been compared with those obtained by the method in [47] for a variety of cases. In all of them, the two methods yielded identical results, validating in this way the forward method used in this chapter.

4.3 Optimization approach to inverse problem

4.3.1 Objective function

In the inverse problem, we optimize the constitutive parameters so that the calculated reflection and transmission data match the measured data. We denote all the parameters to be optimized as $\overline{x}$, and define the objective function as,

$$\text{Min.} : f(\overline{x}) = \sum_{\{\theta,\phi\}} \sum_{i,j \in \{1,2\}} \left\{ W_{ij}^r(\theta,\phi) |\tilde{r}_{ij}(\theta,\phi) - \tilde{r}_{ij}^m(\theta,\phi)|^2 + W_{ij}^t(\theta,\phi) |\tilde{t}_{ij}(\theta,\phi) - \tilde{t}_{ij}^m(\theta,\phi)|^2 \right\},$$

(4.14)

where $\tilde{r}_{ij}(\theta,\phi)$, $\tilde{t}_{ij}(\theta,\phi)$ are the calculated reflection and transmission coefficients as function of incident angles, and $\tilde{r}_{ij}^m(\theta,\phi)$, $\tilde{t}_{ij}^m(\theta,\phi)$ are the measured reflection and transmission coefficients. The weighting factor are chosen as

$$W_{ij}^r(\theta,\phi) = \frac{1}{|\tilde{r}_{ij}^m(\theta,\phi)| + \alpha},$$

(4.15)

where α is a positive parameter that avoids an infinite weight for small magnitudes of $\tilde{r}_{ij}^m(\theta,\phi)$. Note that W_{ij}^t is defined similarly.

The optimization method seeks at minimizing the objective function whose global-minimum value is zero, which is obtained when the measured and computed data are identical, indicating that the retrieved constitutive tensors are identical to the original ones.

4.3.2 Optimization methods

We note that the optimization problem Eq. (4.14) is highly non-linear: from Eq. (4.5) it can be seen that all the unknown parameters are in the argument of the exponential function. The objective function has many local minima, which makes the search for a global minimum intractable with deterministic optimization methods and stochastic optimization methods should be used instead. However, the stochastic methods are often slowly-convergent, sometimes resulting in intolerable computation burden. Therefore, we design here a hybrid optimization algorithm, which combines the differential evolution

(DE) [36] algorithm to the simplex method.

Differential evolution algorithm is a stochastic parallel direct search optimization algorithm, which utilizes a number of parameter vectors, known as individuals, as a generation to explore the search space [36, 57]. It is similar to genetic algorithm (GA), but there are differences between them. In each generation, mutation and crossover operators are applied to the individuals of the current generation to generate a trial population. The corresponding individuals in the two populations compete in the selection operation to become members of the next generation. The mutation operator of DE generates new parameter vectors by adding the weighted difference between two parameter vectors to a third one. The algorithm stops when a specified maximum number of evolution generations is reached. The DE algorithm can be applied to nonlinear and multi-modal problems with continuous variables, with good global searching ability [36, 57, 58].

Simplex method [59, 60] is a direct search optimization algorithm, i.e., there is no need for gradient information of the objective function. The geometric figure formed by a set of $n + 1$ points in an n-dimensional space is called a simplex, such as a triangle in two dimensions and a tetrahedron in three dimensions. The basic idea of simplex optimization method is to compare the values of the objective function at the $n + 1$ vertices of a simplex and rearrange the simplex gradually toward the optimum point during the iterative process. The movement of the simplex is achieved by using three operations: reflection, contractions, and expansion. The movement stops when the standard deviation of the function at the $n + 1$ vertices of the current simplex is smaller than a prescribed small quantity. Simplex method is good at searching local minimum and converges fast compared with DE algorithm.

In the retrieval of the bianisotropy media, DE is first used to perform a parallel search in order to explore the entire solution space, and yields a set of solutions bearing good genes. The simplex method, which is good at obtaining local minimum, is used subsequently, taking the solution set from DE as initial guesses.

4.4 Numerical reconstruction

In this section, numerical examples are presented to show the feasibility and the robustness of the proposed optimization method. In the first two examples, we suppose that we know a priori some properties of the medium, so that the total number of unknowns is reduced and the optimization problem becomes relatively easier. In the subsequent examples, we apply a 72-parameter retrieval method to two arbitrarily chosen media. In all the cases, we show that the proposed method is able to reconstruct the constitutive tensors despite the high nonlinearity of the problem. Note that in all the following numerical examples, I first calculate S parameters using the forward problem solver, and then treat them as the measured ones to evaluate the optimized ones in the inverse process.

4.4.1 Rotated biaxial medium

In this first example, prior knowledge of the medium is assumed: we know that the medium to be retrieved is biaxial in both permittivity and permeability, yet, the numerical values and the axes of the medium are unknown. Hence, we characterize the medium through the tensors,

$$\bar{\bar{\epsilon}} = U^T Diag\{\epsilon_x, \epsilon_y, \epsilon_z\} U \tag{4.16}$$

$$\bar{\bar{\mu}} = U^T Diag\{\mu_x, \mu_y, \mu_z\} U \tag{4.17}$$

where $Diag\{\epsilon_x, \epsilon_y, \epsilon_z\}$ and $Diag\{\mu_x, \mu_y, \mu_z\}$ are the unrotated permittivity and permeability tensors, respectively, and U is rotation matrix defined by

$$U = \begin{pmatrix} \cos\alpha\cos\beta\cos\gamma - \sin\alpha\sin\gamma & \sin\alpha\cos\beta\cos\gamma + \cos\alpha\sin\gamma & -\sin\beta\cos\gamma \\ -\cos\alpha\cos\beta\sin\gamma - \sin\alpha\cos\gamma & -\sin\alpha\cos\beta\sin\gamma + \cos\alpha\cos\gamma & \sin\beta\sin\gamma \\ \cos\alpha\sin\beta & \sin\alpha\sin\beta & \cos\beta \end{pmatrix} \tag{4.18}$$

71

where (α, β, γ) are the Euler angles [61]. Consequently, the optimization vector contains 15 unknowns,

$$\overline{x} = (\alpha, \beta, \gamma, \epsilon_x', \epsilon_y', \epsilon_z', \epsilon_x'', \epsilon_y'', \epsilon_z'', \mu_x', \mu_y', \mu_z', \mu_x'', \mu_y'', \mu_z'')$$

where $(\cdot)\prime$ and $(\cdot)\prime\prime$ denote the real part and imaginary part operators, respectively.

Various values and frequency dependent functions have been successfully retrieved with our method although these are not shown here. For the sake of illustration, we choose here the following parameters,

$$
\begin{aligned}
\epsilon_x(f) &= 1 - F_{ex}f^2/(f^2 - f_{ex}^2 + i\gamma_{ex}f), \\
\epsilon_y(f) &= 1 - F_{ey}f^2/(f^2 - f_{ey}^2 + i\gamma_{ey}f), \\
\epsilon_z(f) &= 1 - F_{ez}f^2/(f^2 - f_{ez}^2 + i\gamma_{ez}f), \\
\mu_x(f) &= 1 - F_{mx}f^2/(f^2 - f_{mx}^2 + i\gamma_{mx}f), \\
\mu_y(f) &= 1 - F_{my}f^2/(f^2 - f_{my}^2 + i\gamma_{my}f), \\
\mu_z(f) &= 1 - F_{mz}f^2/(f^2 - f_{mz}^2 + i\gamma_{mz}f)
\end{aligned}
\tag{4.19}
$$

where $f_{ex} = 4.0$ GHz, $f_{ey} = 5.0$ GHz, $f_{ez} = 3.5$ GHz, $f_{mx} = 5.0$ GHz, $f_{mx} = 4.0$ GHz, $f_{mx} = 3.5$ GHz, $\gamma_{ex} = 0.5$ GHz, $\gamma_{ey} = 0.4$ GHz, $\gamma_{ez} = 0.3$ GHz, $\gamma_{mx} = 0.4$ GHz, $\gamma_{my} = 0.3$ GHz, $\gamma_{mz} = 0.2$ GHz, $F_{ex} = 0.5$, $F_{ey} = 0.3$, $F_{ez} = 0.4$ $F_{mx} = 0.3$, $F_{my} = 0.2$, $F_{mz} = 0.3$. The operating frequency range is from 2 GHz to 8 GHz. The rotation angles are $\alpha = \pi/4$, $\beta = \pi/4$, $\gamma = \pi/6$. The thickness of the slab is $\lambda_0/20$, where λ_0 is the wavelength in free space at the initial frequency. The slab is illuminated under normal incidence as well as oblique incidences with the incidence angle $(\theta, \phi) \in \{(45°, 0°), (45°, 45°), (45°, 90°)\}$.

For the initial frequency of 2 GHz, we use DE and simplex methods to optimize for the constitutive parameters and the rotation angles. In the first stage of the optimization, DE runs for 1600 generations, with a total population of 150 individuals in each generation. Subsequently, half of the population of the last generation are used in the simplex method,

where each of the individuals is treated as an initial guess. After the first round of simplex, about half of the solutions are chosen as initial guesses for the second round of simplex optimization. The above procedure is iterated until solutions with small objective functions are achieved.

Table 4.1: Optimization results for rotated biaxial medium

	Exact	Optimized 1st	Optimized 2nd	Optimized 3rd	Optimized 4th	Optimized 5th	Optimized 6th
α_0	7.8540e-01	1.4699e+00	2.7443e+00	1.4701e+00	5.8853e+00	5.8855e+00	3.9271e+00
β_0	7.8540e-01	1.4699e+00	2.7443e+00	1.4701e+00	5.8853e+00	5.8855e+00	3.9271e+00
γ_0	5.2360e-01	3.6048e+00	2.2869e+00	4.6372e-01	3.9991e+00	8.5830e-01	5.7600e+00
ϵ'_x	1.1655e+00	1.1930e+00	1.1654e+00	1.1929e+00	1.1655e+00	1.1656e+00	1.1656e+00
ϵ'_y	1.0571e+00	1.0571e+00	1.1931e+00	1.0571e+00	1.1929e+00	1.1928e+00	1.0570e+00
ϵ'_z	1.1929e+00	1.1655e+00	1.0572e+00	1.1656e+00	1.0570e+00	1.0568e+00	1.1928e+00
ϵ''_x	1.3793e-02	1.3981e-02	1.2996e-02	1.5983e-02	1.3797e-02	1.3560e-02	1.3827e-02
ϵ''_y	2.1737e-03	2.0648e-03	1.5481e-02	3.3855e-03	1.4023e-02	1.4372e-02	2.1341e-03
ϵ''_z	1.4030e-02	1.3905e-02	3.0442e-03	1.2894e-02	2.1709e-03	2.2321e-03	1.4041e-02
μ'_x	1.0571e+00	1.1452e+00	1.0569e+00	1.1451e+00	1.0571e+00	1.0572e+00	1.0571e+00
μ'_y	1.0665e+00	1.0665e+00	1.1451e+00	1.0665e+00	1.1451e+00	1.1451e+00	1.0664e+00
μ'_z	1.1451e+00	1.0571e+00	1.0667e+00	1.0571e+00	1.0665e+00	1.0664e+00	1.1451e+00
μ''_x	2.1737e-03	7.2363e-03	4.8521e-04	7.5070e-03	2.1787e-03	1.5714e-03	2.1361e-03
μ''_y	3.3250e-03	3.2994e-03	7.4335e-03	3.1615e-03	7.0300e-03	7.1437e-03	3.3202e-03
μ''_z	7.0358e-03	1.9964e-03	3.2429e-03	3.5834e-07	3.3240e-03	3.3025e-03	7.0225e-03
$f(\bar{x})$	0	1.4525e-05	6.1939e-05	7.8181e-05	1.0325e-06	2.7679e-05	7.6682e-06

In the present numerical example, we obtain the six solutions as shown in Table 4.1 by using the DE and four rounds of simplex method. The fact that the coordinate axes are labeled differently (for example, the $\hat{x}$, $\hat{y}$, and $\hat{z}$ are labeled as $-\hat{x}$, $-\hat{y}$, and $-\hat{z}$, respectively, in the sixth solution) makes the solutions seemingly different from each other. In fact, the six solutions are almost identical as shown in Table 4.2 when expressed in the rotated form (see Eqs. (4.16) and (4.17)). Note that the full tensors of $\bar{\bar{\epsilon}}$ and $\bar{\bar{\mu}}$ are both symmetric matrices, thus only the elements in the left lower part of the tensors are shown in Table 4.2.

For the retrieval at higher frequencies, we choose the linear extrapolation of the results at the previous two frequencies as a initial guess for the simplex optimization. Note that for the second frequency, the initial guess is just the result obtained at the initial frequency.

To quantitatively describe the match between the true and the retrieved constitutive parameters, we define the relative mismatch (RM) to be

$$RM(\rho) = \begin{cases} \frac{|\rho_t - \rho_r|}{|\rho_t|} & \text{if } |\rho_t| > \tau, \\ |\rho_r| & \text{otherwise,} \end{cases} \qquad (4.20)$$

where ρ can be any component of $\bar{\bar{\epsilon}}$ and $\bar{\bar{\mu}}$, subscript "t" and "r" denote "true" and "re-

Table 4.2: Optimization results for rotated biaxial medium (in full tensor form)

ϵ'_{xx}	1.0917e+00	1.0917e+00	1.0917e+00	1.0917e+00	1.0917e+00	1.0916e+00	1.0917e+00
ϵ''_{xx}	5.2111e-03	5.1162e-03	6.2015e-03	6.5960e-03	5.2097e-03	5.3432e-03	5.1840e-03
ϵ'_{yx}	4.0725e-02	4.0754e-02	4.0757e-02	4.0746e-02	4.0743e-02	4.0769e-02	4.0737e-02
ϵ''_{yx}	3.6903e-03	3.7194e-03	3.7333e-03	3.7442e-03	3.6896e-03	3.7398e-03	3.7099e-03
ϵ'_{zx}	4.2738e-02	4.2750e-02	4.2632e-02	4.2749e-02	4.2776e-02	4.2870e-02	4.2682e-02
ϵ''_{zx}	3.6265e-03	3.6346e-03	3.8996e-03	3.9914e-03	3.6266e-03	3.7476e-03	3.6379e-03
ϵ'_{yy}	1.1581e+00	1.1581e+00	1.1582e+00	1.1581e+00	1.1581e+00	1.1581e+00	1.1581e+00
ϵ''_{yy}	1.2326e-02	1.2369e-02	1.2319e-02	1.2417e-02	1.2326e-02	1.2276e-02	1.2343e-02
ϵ'_{zy}	-4.2006e-03	-4.1730e-03	-3.9746e-03	-4.2372e-03	-4.2592e-03	-4.3667e-03	-4.2756e-03
ϵ''_{zy}	-1.4048e-03	-1.4889e-03	-3.8719e-04	-1.2679e-04	-1.4107e-03	-1.1672e-03	-1.4219e-03
ϵ'_{zz}	1.1656e+00	1.1657e+00	1.1658e+00	1.1657e+00	1.1656e+00	1.1656e+00	1.1656e+00
ϵ''_{zz}	1.2459e-02	1.2465e-02	1.3001e-02	1.3249e-02	1.2455e-02	1.2545e-02	1.2475e-02
μ'_{xx}	1.0861e+00	1.0861e+00	1.0861e+00	1.0861e+00	1.0861e+00	1.0861e+00	1.0860e+00
μ''_{xx}	4.2454e-03	4.2745e-03	4.2688e-03	4.2283e-03	4.2439e-03	4.2532e-03	4.2379e-03
μ'_{yx}	1.9063e-02	1.9075e-02	1.9067e-02	1.9057e-02	1.9062e-02	1.9071e-02	1.9083e-02
μ''_{yx}	8.5575e-04	9.0211e-04	8.8027e-04	8.8887e-04	8.5429e-04	8.5041e-04	8.5113e-04
μ'_{zx}	2.8247e-02	2.8279e-02	2.8111e-02	2.8240e-02	2.8275e-02	2.8320e-02	2.8275e-02
μ''_{zx}	1.3680e-03	1.4552e-03	1.6096e-03	1.6904e-03	1.3669e-03	1.4443e-03	1.3667e-03
μ'_{yy}	1.0803e+00	1.0803e+00	1.0804e+00	1.0803e+00	1.0803e+00	1.0803e+00	1.0803e+00
μ''_{yy}	3.5404e-03	3.4773e-03	2.6017e-03	2.2922e-03	3.5398e-03	3.1852e-03	3.5135e-03
μ'_{zy}	3.2317e-02	3.2370e-02	3.2561e-02	3.2308e-02	3.2292e-02	3.2224e-02	3.2328e-02
μ''_{zy}	1.8665e-03	2.0198e-03	2.8171e-03	3.0589e-03	1.8610e-03	2.1893e-03	1.8795e-03
μ'_{zz}	1.1023e+00	1.1023e+00	1.1021e+00	1.1022e+00	1.1023e+00	1.1024e+00	1.1023e+00
μ''_{zz}	4.7487e-03	4.7803e-03	4.2911e-03	4.1484e-03	4.7490e-03	4.5791e-03	4.7275e-03

trieved", respectively, and τ is a small positive parameter, below which the relative mismatch is defined in an alternative way. In the present and all subsequent numerical examples, we choose τ to be 0.05. To represent the mismatch across all sample frequencies, we define an averaged relative mismatch (A_{RM}) to be the mean of RM across all sample frequencies.

The optimization results, not shown here, show that the true and the optimized results are almost identical for both the real and imaginary parts at all frequencies. The maximum A_{RM} among the six components being retrieved is 0.0063, which is small and indicates a good match between the true and retrieved results.

4.4.2 Rotated Omega medium

In the second example, we reconstruct the parameters of a rotated Omega medium, which is a bianisotropic medium with the following constitutive parameters

$$\bar{\bar{\epsilon}} = \epsilon_0 \begin{pmatrix} \epsilon_x & 0 & 0 \\ 0 & \epsilon_y & 0 \\ 0 & 0 & \epsilon_z \end{pmatrix}, \quad \bar{\bar{\mu}} = \mu_0 \begin{pmatrix} \mu_x & 0 & 0 \\ 0 & \mu_y & 0 \\ 0 & 0 & \mu_z \end{pmatrix},$$

$$\bar{\bar{\xi}} = \frac{1}{c} \begin{pmatrix} 0 & 0 & 0 \\ 0 & 0 & 0 \\ 0 & -i\xi_0 & 0 \end{pmatrix}, \quad \bar{\bar{\zeta}} = \frac{1}{c} \begin{pmatrix} 0 & 0 & 0 \\ 0 & 0 & i\xi_0 \\ 0 & 0 & 0 \end{pmatrix}, \tag{4.21}$$

For the forward problem, the constitutive parameters for $\bar{\bar{\epsilon}}$ and $\bar{\bar{\mu}}$ are taken to be the same as in the rotated biaxial case (see Eq. (4.19)), and the value of ξ_0 is chosen to be

$$\xi_0(f) = 1 - F_\xi f^2 / (f^2 - f_\xi^2 + i\gamma_\xi f)$$

where $f_{xi} = 4.0$ GHz, $\gamma_\xi = 0.5$ GHz, $F_\xi = 0.4$. The rotation angles are arbitrarily set to $\alpha = \pi/5$, $\beta = \pi/4$, $\gamma = \pi/6$, and the incidence and the thickness of the slab are identical to those in the rotated biaxial case. The total number of unknowns in this case is seventeen, where the real and the imaginary part of ξ_0 are added compared to the rotated biaxial case.

The constitutive parameters are reconstructed using the same procedure as the one described in the biaxial case. For the initial frequency, DE algorithm runs for 2000 generations, with a population of 170 individuals in each generation. Simplex method runs for five rounds and obtain four solutions listed in Table 4.3. Here again, all the solutions are almost identical to the true one when expressed in the rotated form (see Eqs. (4.16) and (4.17) for ϵ and μ, and the rotation for ξ and ζ is defined similarly). For higher frequencies, the linear extrapolation are used in the simplex method. The true and the optimized results are almost identical at most frequencies for the components of $\bar{\bar{\epsilon}}$, $\bar{\bar{\mu}}$, and $\bar{\bar{\xi}}$, and only ξ_0 is shown in Fig. 4-1 for the purpose of illustration. The maximum A_{RM} among the seven components is 0.0096, which is for ξ_0.

Table 4.3: Optimization results for Omega medium

	Exact	Optimized 1st	Optimized 2nd	Optimized 3rd	Optimized 4th
α_0	6.2832e-01	6.2964e-01	6.2978e-01	6.2844e-01	3.7698e+00
β_0	7.8540e-01	7.8695e-01	7.8708e-01	7.8554e-01	2.3563e+00
γ_0	5.2360e-01	6.8059e+00	5.2259e-01	3.6651e+00	2.6179e+00
ϵ'_x	1.1655e+00	1.1651e+00	1.1650e+00	1.1654e+00	1.1655e+00
ϵ'_y	1.0571e+00	1.0571e+00	1.0571e+00	1.0571e+00	1.0571e+00
ϵ'_z	1.1929e+00	1.1936e+00	1.1936e+00	1.1928e+00	1.1929e+00
ϵ''_x	1.3793e-02	1.5862e-02	1.6209e-02	1.3972e-02	1.3662e-02
ϵ''_y	2.1737e-03	2.1362e-03	2.1529e-03	2.1664e-03	2.1756e-03
ϵ''_z	1.4030e-02	1.4184e-02	1.4285e-02	1.3988e-02	1.3987e-02
μ'_x	1.0571e+00	1.0570e+00	1.0570e+00	1.0571e+00	1.0571e+00
μ'_y	1.0665e+00	1.0660e+00	1.0662e+00	1.0665e+00	1.0665e+00
μ'_z	1.1451e+00	1.1446e+00	1.1448e+00	1.1451e+00	1.1451e+00
μ''_x	2.1737e-03	2.2299e-03	2.1899e-03	2.2087e-03	2.1763e-03
μ''_y	3.3250e-03	4.2892e-04	4.9731e-06	3.2113e-03	3.4997e-03
μ''_z	7.0358e-03	6.7278e-03	6.5528e-03	7.0260e-03	7.0613e-03
ξ'_0	1.1324e+00	1.1330e+00	1.1331e+00	-1.1324e+00	-1.1324e+00
ξ''_0	1.1034e-02	1.0586e-02	1.0560e-02	-1.1077e-02	-1.1043e-02
$f(\overline{x})$	0	2.5906e-05	2.8427e-05	3.7121e-06	1.6790e-06

4.4.3 General bianisotropic medium

In the following two numerical examples, we consider the problem of parameter recon-struction in media with arbitrary constitutive parameters. Both the real and the imaginary parts of the $\overline{\overline{\epsilon}}$, $\overline{\overline{\mu}}$, $\overline{\overline{\xi}}$, and $\overline{\overline{\zeta}}$ tensors are optimized, 72 parameters altogether, in order to match the measured reflection and transmission data. In the forward problem, we consider two media, known as Chiroferrite $D_\infty(C_\infty)$ and Omegaferrite $C_{2v}(C_s)$ [62]. Note that in these numerical examples, although specific media are considered in the forward problem, we still optimize 72 parameters in the inverse problem.

Case 1: Chiroferrite $D_\infty(C_\infty)$
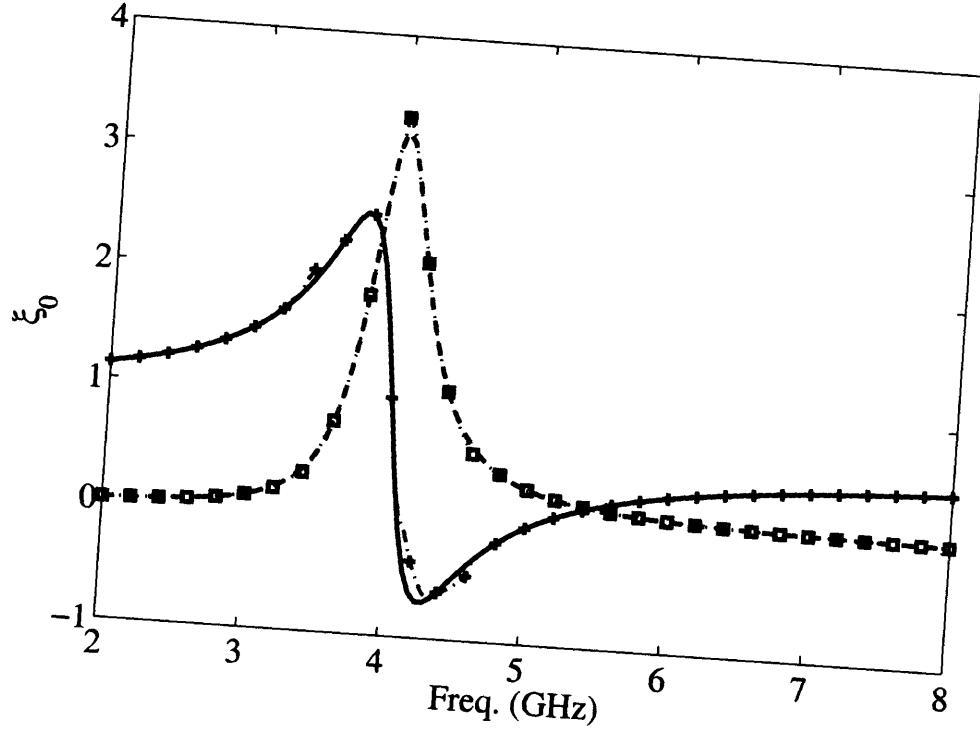
Figure 4-1: Comparison of the retrieved and the true ξ_0 of an Omega medium

The constitutive tensors of the Chiroferrite $D_\infty(C_\infty)$ is given by

$$\bar{\bar{\epsilon}} = \epsilon_0 \begin{pmatrix} \epsilon_{xx} & \epsilon_{xy} & 0 \\ -\epsilon_{xy} & \epsilon_{xx} & 0 \\ 0 & 0 & \epsilon_{zz} \end{pmatrix}, \ \bar{\bar{\mu}} = \mu_0 \begin{pmatrix} \mu_{xx} & \mu_{xy} & 0 \\ -\mu_{xy} & \mu_{xx} & 0 \\ 0 & 0 & \mu_{zz} \end{pmatrix},$$

$$\bar{\bar{\xi}} = \frac{1}{c} \begin{pmatrix} \xi_{xx} & \xi_{xy} & 0 \\ -\xi_{xy} & \xi_{xx} & 0 \\ 0 & 0 & \xi_{zz} \end{pmatrix}, \ \bar{\bar{\zeta}} = \frac{1}{c} \begin{pmatrix} -\xi_{xx} & -\xi_{xy} & 0 \\ \xi_{xy} & -\xi_{xx} & 0 \\ 0 & 0 & -\xi_{zz} \end{pmatrix}, \quad (4.22)$$

It is important to highlight again that although the tensors have some zero components, this is not an information used by our method and we optimize 72 parameters, thus obtaining a

77

value of zero whenever necessary. The non-zero parameters are chosen to be

$$\epsilon_{xx}(f) = 1 - f_{pexx}^2/(f^2 - f_{0exx}^2 + i\gamma_{exx}f),$$

$$\epsilon_{xy}(f) = 0.1 + 0.05i \qquad\qquad (4.23)$$

$$\epsilon_{zz}(f) = 1 - f_{pezz}^2/(f^2 - f_{0ezz}^2 + i\gamma_{ezz}f),$$

$$\mu_{xx}(f) = 1 - f_{pmxx}^2/(f^2 - f_{0mxx}^2 + i\gamma_{mxx}f),$$

$$\mu_{xy}(f) = 0.1i$$

$$\mu_{zz}(f) = 1$$

$$\xi_{xx}(f) = 1 - e^{-f/10^{10}}$$

$$\xi_{xy}(f) = 1 - f_{p\xi}^2/(f^2 - f_{0\xi}^2 + i\gamma_\xi f),$$

$$\xi_{zz}(f) = (0.1 + 0.05i)f/10^9$$

with $f_{pexx} = 4.5$ GHz, $f_{pezz} = 3.5$ GHz, $f_{pmxx} = 4.0$ GHz, $f_{p\xi} = 3.0$ GHz, $f_{0exx} = 4.0$ GHz, $f_{0ezz} = 3.0$ GHz, $f_{0mxx} = 3.5$ GHz, $f_{0\xi} = 2.5$ GHz, $\gamma_{exx} = 2.0$ GHz, $\gamma_{ezz} = 1.2$ GHz, $\gamma_{mxx} = 1.5$ GHz, and $\gamma_\xi = 1.1$ GHz

We first optimize the parameters at the initial frequency of 0.1 GHz. Totally unconstrained optimization problems with 72 unknowns are difficult to deal with, and parallel computing is helpful in order to get good results in a reasonable time period. This being not available to us, we resort to a physical assumption that simplifies the optimization problem and make it manageable on a single PC within a few hours. Our assumption is that the bianisotropy is weak, namely, $\overline{\overline{\xi}}$ and $\overline{\overline{\zeta}}$ approach to zero at relatively low frequencies. Although this assumption does not hold for some media, it is true for most materials. Hence, in the first stage of the approach, $\overline{\overline{\epsilon}}$ and $\overline{\overline{\mu}}$ are optimized with $\overline{\overline{\xi}}$ and $\overline{\overline{\zeta}}$ being zero. When a good match in reflection and transmission is achieved, i.e.,$\overline{\overline{\epsilon}}$ and $\overline{\overline{\mu}}$ are close to the exact solution, we start the second-stage of optimization, where $\overline{\overline{\xi}}$ and $\overline{\overline{\zeta}}$, together with $\overline{\overline{\epsilon}}$ and $\overline{\overline{\mu}}$ are optimized at low frequencies, with the solution obtained in the first stage treated as the initial guess. The two-stage process ensures that if the bianisotropic parameters are not exactly zero at low frequencies, non-zero but small values are used as initial guesses.

In the numerical simulation, we take a slab thickness of $\lambda_0/30$, where λ_0 denotes the

wavelength in free space at the initial frequency. Note that a thickness of $\lambda_0/30$ is not too restrictive because of the very large wavelength at 0.1 GHz. Note also the importance of the thickness of the slab in the optimization: if the slab is too thin compared with the wavelength, it is almost transparent so that the reflection is almost zero and the transmission is almost unity. In this case, the constitutive parameters have little influence in determining the reflection and transmission coefficients, which yields an ill-conditioned problem. On the other hand, if the slab is too thick, the problem becomes dramatically nonlinear, and is difficult to optimize. From our experience, thicknesses within $\lambda_0/30$ to $\lambda_0/10$ are good for the optimization at the initial frequency.

There are two important issues in solving the inverse problem with 72 parameters, namely uniqueness and computational burden. Fewer incidences are likely to result in non-uniqueness, while too many incidences require intractable computation power. Therefore, it would be valuable to know the number of the incidence directions that are necessary and sufficient to obtain a unique solution with a manageable computational burden. Unfortunately, it is difficult or even impossible to answer this question and we have to choose the incidence directions and number empirically. In our numerical simulations, we choose different number of incidences at different optimization stages. Since DE algorithm explores the search space using a group of individuals as a generation, it is characterized by the properties of good global searching abilities but is also time-consuming. In this respect, we choose few incidences in the DE optimization. On the other hand, since there are fewer individuals in the simplex method and we aim at obtaining the unique solution at this optimization stage, we choose more diverse incidences in the simplex optimization.

At the first stage of optimization, *i.e.*, looking for $\bar{\bar{\epsilon}}$ and $\bar{\bar{\mu}}$ with $\bar{\bar{\xi}}$ and $\bar{\bar{\zeta}}$ being zero, DE is applied first and simplex method is used subsequently. In the DE optimization, the slab is illuminated at normal incidence as well as oblique incidences with $\theta = 80°$ and seven ϕ evenly distributed from $0°$ to $360°$, which is written in shorthand as $< 80°, 7 >$. The population in each generation is 360 and the total generation of the evolution is 2000. Then, the simplex method is used to realize the local searching, where more incidences $(< 72°, 5 >, < 60°, 4 >)$ are added in addition to the original ones. Simplex method is sequentially carried out until there is no significant improvement over the results obtained

from the previous round. We finally obtain 6 solutions, all of which have an objective functions smaller than 0.003.

At the second stage of the optimization, with the results obtained in the first stage as initial guesses, we optimize 72 constitutive parameters to further match the reflection and transmission coefficients. During the sequential application of the simplex method, we drop the worst one due to its slow convergence, and finally obtain 5 solutions, all of which are close to the exactly solution. The best one $\overline{x}_{opt}$, with the objective function value $8.2819e - 05$, is expressed in tensor form as

$$\overline{\overline{\epsilon}} = \begin{pmatrix} 2.2574 \times 10^0 + i3.1142 \times 10^{-2} & 1.0004 \times 10^{-1} + i5.0110 \times 10^{-2} & -1.7325 \times 10^{-3} - i1.3521 \times 10^{-3} \\ -1.0003 \times 10^{-1} - i5.0050 \times 10^{-2} & 2.2574 \times 10^0 + i3.1087 \times 10^{-2} & 2.0543 \times 10^{-3} - i1.6488 \times 10^{-3} \\ -1.6469 \times 10^{-3} - i1.3089 \times 10^{-3} & -1.0716 \times 10^{-3} - i1.1411 \times 10^{-3} & 2.4240 \times 10^0 - i5.9698 \times 10^{-2} \end{pmatrix},$$

$$\overline{\overline{\mu}} = \begin{pmatrix} 2.2978 \times 10^0 + i2.9986 \times 10^{-2} & -7.0558 \times 10^{-5} + i1.0007 \times 10^{-1} & -6.1793 \times 10^{-4} - i5.2777 \times 10^{-4} \\ 2.9643 \times 10^{-5} - i1.0006 \times 10^{-1} & 2.2979 \times 10^0 + i2.9957 \times 10^{-2} & -3.7733 \times 10^{-4} - i5.2512 \times 10^{-4} \\ -7.6239 \times 10^{-4} - i5.6321 \times 10^{-4} & 8.6050 \times 10^{-4} - i7.3461 \times 10^{-4} & 1.0101 \times 10^0 - i1.4723 \times 10^{-2} \end{pmatrix},$$

$$\overline{\overline{\xi}} = \begin{pmatrix} 9.6879 \times 10^{-3} + i4.9159 \times 10^{-5} & 2.5333 \times 10^{-3} + i1.8333 \times 10^{-2} & -4.3811 \times 10^{-5} + i3.2369 \times 10^{-5} \\ -2.5505 \times 10^{-3} - i1.8330 \times 10^{-2} & 9.6820 \times 10^{-3} + i1.9989 \times 10^{-5} & 1.1471 \times 10^{-5} + i1.6218 \times 10^{-5} \\ -6.7776 \times 10^{-4} + i1.1243 \times 10^{-4} & 3.8108 \times 10^{-4} + i4.0342 \times 10^{-4} & 1.0602 \times 10^{-2} + i4.3711 \times 10^{-3} \end{pmatrix},$$

$$\overline{\overline{\zeta}} = \begin{pmatrix} -9.9637 \times 10^{-3} + i - 1.4234 \times 10^{-4} & -3.0222 \times 10^{-3} - i1.9711 \times 10^{-2} & 7.8364 \times 10^{-5} + i3.3801 \times 10^{-5} \\ 3.0341 \times 10^{-3} + i1.9728 \times 10^{-2} & -9.9609 \times 10^{-3} - i1.2851 \times 10^{-4} & 9.5813 \times 10^{-5} + i3.3791 \times 10^{-5} \\ -1.0464 \times 10^{-4} + i1.3586 \times 10^{-4} & -1.4829 \times 10^{-4} - i6.8296 \times 10^{-5} & -1.1364 \times 10^{-2} - i4.6567 \times 10^{-3} \end{pmatrix}.$$

We find that the solution is pretty close to the true solution $\overline{x}_{tr}$:

$$\overline{\overline{\epsilon}} = \begin{pmatrix} 2.2662 \times 10^0 + i1.5838 \times 10^{-2} & 1.0000 \times 10^{-1} + i5.0000 \times 10^{-2} & 0 \\ -1.0000 \times 10^{-1} - i5.0000 \times 10^{-2} & 2.2662 \times 10^0 + i1.5838 \times 10^{-2} & 0 \\ 0 & 0 & 2.3624 \times 10^0 + i1.8185 \times 10^{-2} \end{pmatrix},$$

$$\overline{\overline{\mu}} = \begin{pmatrix} 2.3070 \times 10^0 + i1.6017 \times 10^{-2} & i1.0000 \times 10^{-1} & 0 \\ -i1.0000 \times 10^{-1} & 2.3070 \times 10^0 + i1.6017 \times 10^{-2} & 0 \\ 0 & 0 & 1.0000 \times 10^0 \end{pmatrix},$$

$$\overline{\overline{\xi}} = \begin{pmatrix} 9.9502 \times 10^{-3} & 1.8596 \times 10^{-3} + i2.5417 \times 10^{-2} & 0 \\ -1.8596 \times 10^{-3} - i2.5417 \times 10^{-2} & 9.9502 \times 10^{-3} & 0 \\ 0 & 0 & 1.0000 \times 10^{-2} + i5.0000 \times 10^{-3} \end{pmatrix},$$

$$\overline{\overline{\zeta}} = \begin{pmatrix} -9.9502 \times 10^{-3} & -1.8596 \times 10^{-3} - i2.5417 \times 10^{-2} & 0 \\ 1.8596 \times 10^{-3} + i2.5417 \times 10^{-2} & -9.9502 \times 10^{-3} & 0 \\ 0 & 0 & -1.0000 \times 10^{-2} - i5.0000 \times 10^{-3} \end{pmatrix}.$$

Finally, for the retrieval at higher frequencies, we choose the linear extrapolation of the results at the previous two frequencies as a initial guess for the simplex optimization. We observe that at 2.1 GHz, the thickness of the slab is seventy percent of the wavelength, consequently making the optimization very hard. Thus starting at 2.1 GHz, we choose a thinner slab whose thickness is five percent of the wave length at 2.1 GHz. The optimization results are shown in the following figures.
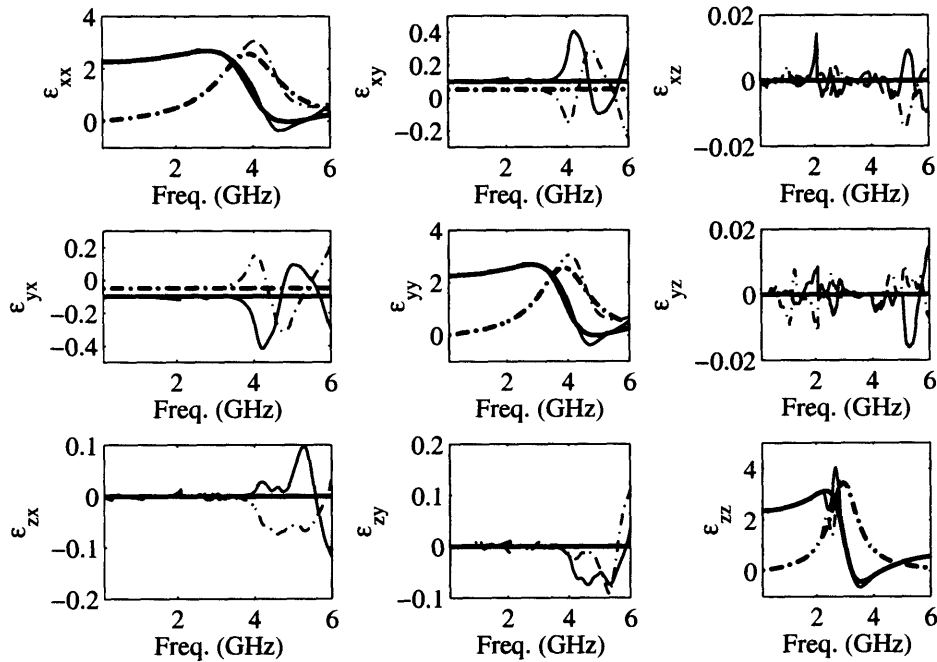
Figure 4-2: Comparison of the retrieved and the true $\bar{\bar{\epsilon}}$ of a Chiroferrite medium. The solid and dotted-dashed lines are for the real and imaginary parts, respectively. The thick and thin lines are for the true and the retrieved results, respectively.

The results show that most of the constitutive parameters are retrieved successfully, although there are some discrepancy around the resonant frequencies. The averaged relative mismatch of each component of the constitutive tensors is

81
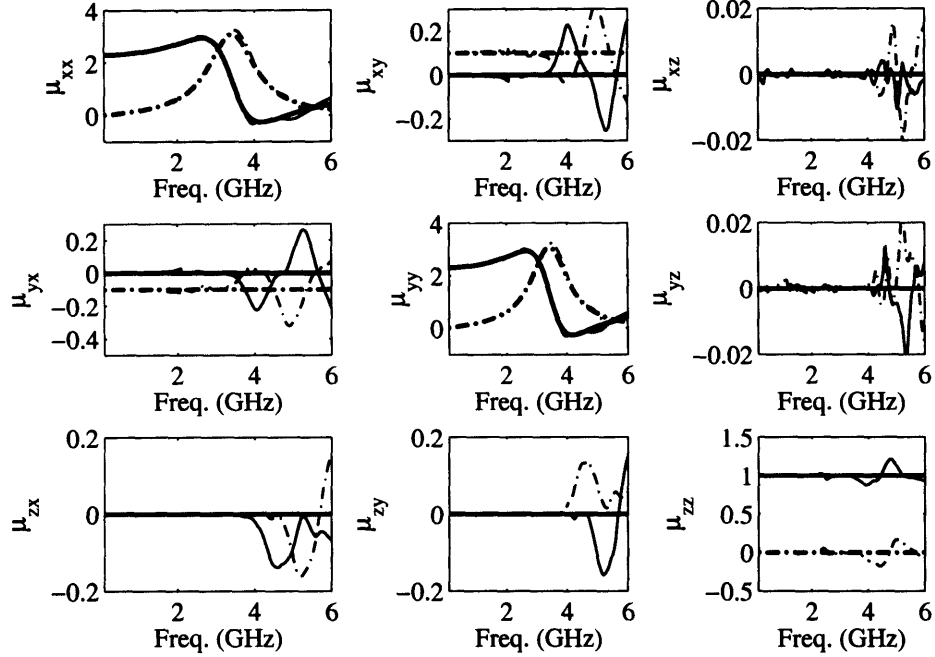
Figure 4-3: Comparison of the retrieved and the true $\overline{\overline{\mu}}$ of a Chiroferrite medium. The solid and dotted-dashed lines are for the real and imaginary parts, respectively. The thick and thin lines are for the true and the retrieved results, respectively.

$$A_{RM}(\epsilon) = \begin{pmatrix} 1.1300 \times 10^{-1} & 8.2992 \times 10^{-1} & 3.7724 \times 10^{-3} \\ 8.1024 \times 10^{-1} & 1.0968 \times 10^{-1} & 4.4050 \times 10^{-3} \\ 2.8004 \times 10^{-2} & 2.8105 \times 10^{-2} & 6.4340 \times 10^{-2} \end{pmatrix} ,$$

$$A_{RM}(\mu) = \begin{pmatrix} 1.0085 \times 10^{-1} & 8.1866 \times 10^{-1} & 3.3510 \times 10^{-3} \\ 8.1150 \times 10^{-1} & 9.6367 \times 10^{-2} & 3.8351 \times 10^{-3} \\ 3.9807 \times 10^{-2} & 3.9184 \times 10^{-2} & 6.1089 \times 10^{-2} \end{pmatrix} ,$$

$$A_{RM}(\xi) = \begin{pmatrix} 2.1845 \times 10^{-1} & 7.8352 \times 10^{-2} & 3.7047 \times 10^{-3} \\ 7.7722 \times 10^{-2} & 2.1225 \times 10^{-1} & 4.0030 \times 10^{-3} \\ 2.8407 \times 10^{-2} & 2.6761 \times 10^{-2} & 1.1346 \times 10^{-1} \end{pmatrix} ,$$

$$A_{RM}(\zeta) = \begin{pmatrix} 2.5459 \times 10^{-1} & 4.8066 \times 10^{-2} & 3.7612 \times 10^{-3} \\ 4.7054 \times 10^{-2} & 2.5468 \times 10^{-1} & 3.4552 \times 10^{-3} \\ 4.1100 \times 10^{-2} & 4.0474 \times 10^{-2} & 7.6319 \times 10^{-2} \end{pmatrix} ,$$

We see that most components have an averaged relative mismatch smaller than 0.012.

Case 2: Omegaferrite $C_{2v}(C_s)$

As a second example, we consider an Omegaferrite $C_{2v}(C_s)$ medium in the forward
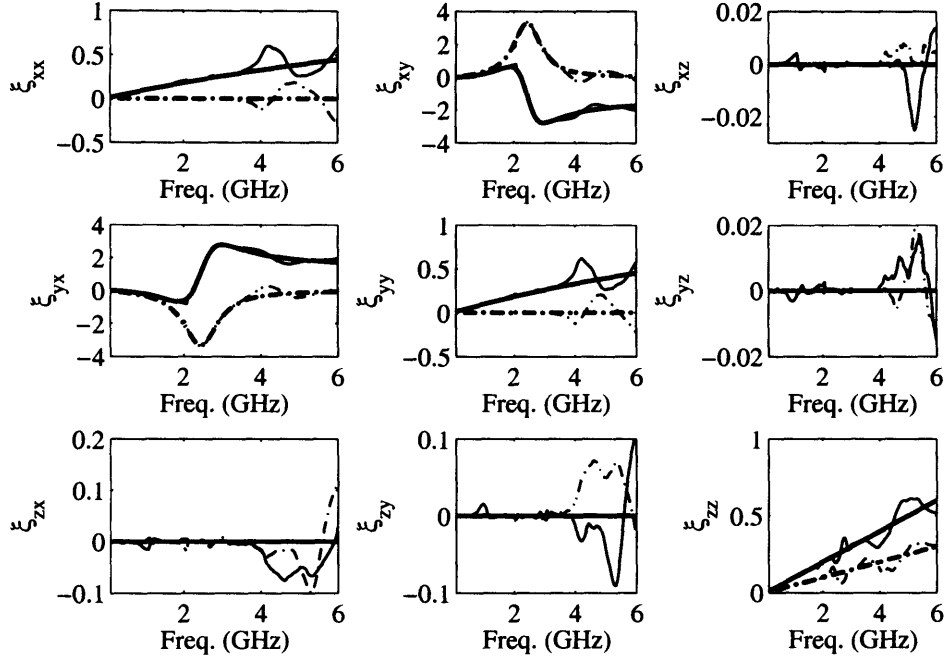
Figure 4-4: Comparison of the retrieved and the true $\overline{\overline{\xi}}$ of a Chiroferrite medium. The solid and dotted-dashed lines are for the real and imaginary parts, respectively. The thick and thin lines are for the true and the retrieved results, respectively.

problem, whose constitutive parameters are

$$\overline{\overline{\epsilon}} = \epsilon_0 \begin{pmatrix} \epsilon_{xx} & 0 & \epsilon_{xz} \\ 0 & \epsilon_{yy} & 0 \\ -\epsilon_{xz} & 0 & \epsilon_{zz} \end{pmatrix}, \ \overline{\overline{\mu}} = \mu_0 \begin{pmatrix} \mu_{xx} & 0 & \mu_{xz} \\ 0 & \mu_{yy} & 0 \\ -\mu_{xz} & 0 & \mu_{zz} \end{pmatrix},$$

$$\overline{\overline{\xi}} = \frac{1}{c} \begin{pmatrix} 0 & \xi_{xy} & 0 \\ \xi_{yx} & 0 & \xi_{yz} \\ 0 & \xi_{zy} & 0 \end{pmatrix}, \ \overline{\overline{\zeta}} = \frac{1}{c} \begin{pmatrix} 0 & -\xi_{yx} & 0 \\ -\xi_{xy} & 0 & \xi_{zy} \\ 0 & \xi_{yz} & 0 \end{pmatrix}, \tag{4.24}$$
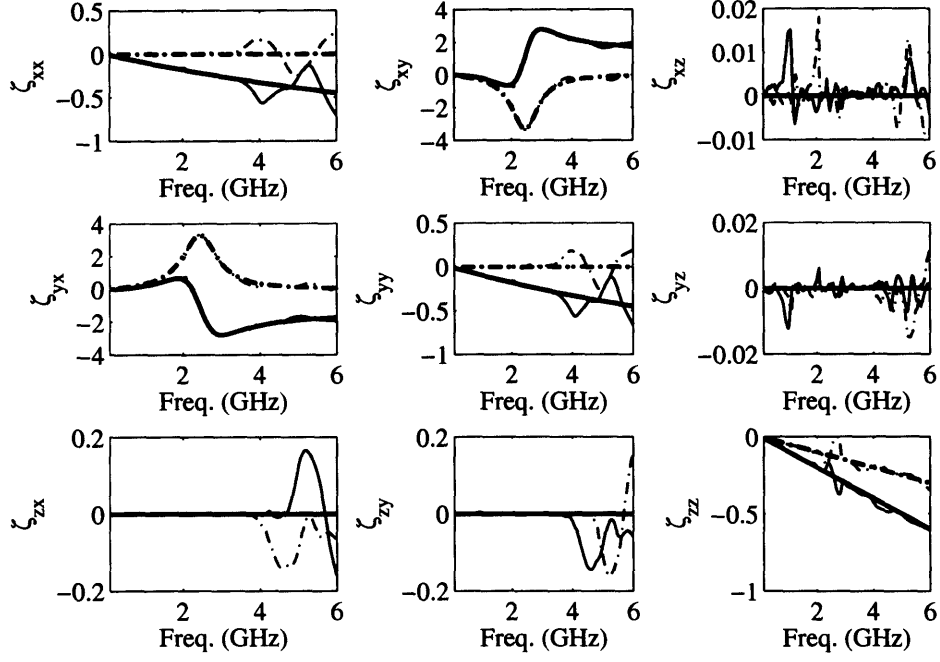
Figure 4-5: Comparison of the retrieved and the true $\overline{\overline{\zeta}}$ of a Chiroferrite medium. The solid and dotted-dashed lines are for the real and imaginary parts, respectively. The thick and thin lines are for the true and the retrieved results, respectively.

In this example, we choose the following parameters,

$$\epsilon_{xx}(f) = 1 - F_{exx}f^2/(f^2 - f_{exx}^2 + i\gamma_{exx}f),$$

$$\epsilon_{yy}(f) = 1 + 0.05i$$ (4.25)

$$\epsilon_{zz}(f) = 1 - F_{ezz}f^2/(f^2 - f_{ezz}^2 + i\gamma_{ezz}f),$$

$$\epsilon_{xz}(f) = 0.1i;$$

$$\mu_{xx}(f) = 1 - F_{mxx}f^2/(f^2 - f_{mxx}^2 + i\gamma_{mxx}f),$$

$$\mu_{yy}(f) = 1 - F_{myy}f^2/(f^2 - f_{myy}^2 + i\gamma_{myy}f),$$

$$\mu_{zz}(f) = 1$$

$$\mu_{xz}(f) = 1 - F_{mxz}f^2/(f^2 - f_{mxz}^2 + i\gamma_{mxz}f),$$

$$\xi_{xy}(f) = 1 - F_\xi f^2/(f^2 - f_\xi^2 + i\gamma_\xi f),$$

$$\xi_{yx}(f) = -\xi_{xy},$$

$$\xi_{yz}(f) = 0.05i,$$

$$\xi_{zy} = -\xi_{yz}$$ (4.26)

where $F_{exx} = 0.2$, $F_{ezz} = 0.4$, $F_{mxx} = 0.3$, $F_{myy} = 0.2$, $F_{mxz} = 0.1$, $F_\xi = 0.1$, $f_{exx} = 4.0$ GHz, $f_{ezz} = 4.5$ GHz, $f_{mxx} = 5.0$ GHz, $f_{myy} = 4.0$ GHz, $f_{mxz} = 3.5$ GHz, $f_\xi = 4.0$ GHz, $\gamma_{exx} = 0.6$ GHz, $\gamma_{ezz} = 0.7$ GHz, $\gamma_{mxx} = 0.9$ GHz, $\gamma_{myy} = 0.5$ GHz, $\gamma_{mxz} = 0.6$ GHz, $\gamma_\xi = 0.5$ GHz.

The frequencies range from 3 GHz to 6 GHz, and the thickness of the slab is $\lambda_0/20$. In this example, we aim at testing the robustness of the linear extrapolation technique in the retrieval at the higher frequencies, so we choose the parameters at the initial frequency to be the exact values. Both clean and noisy data are tested. In the simulations, 2 percent and 5 percent Gaussian random noises are added to the reflection and transmission coefficients. The optimization results are shown in the Fig. 4-6 - Fig. 4-17. We tell from the figures that most of the constitutive parameters are generally reconstructed, although there are noticeable mismatch around the resonance. In the presents of noise, although the reconstructed profiles digress more from the true one, the trends of profiles are kept in the retrieval. For the case of 5 percent noise, the averaged relative mismatch of each component of the constitutive tensors is

$$A_{RM}(\epsilon) = \begin{pmatrix} 1.4424 \times 10^{-1} & 3.2447 \times 10^{-3} & 5.7393 \times 10^{-1} \\ 2.0195 \times 10^{-3} & 9.4122 \times 10^{-2} & 1.2266 \times 10^{-3} \\ 1.0404 \times 10^{0} & 3.0988 \times 10^{-3} & 2.2166 \times 10^{-1} \end{pmatrix},$$

$$A_{RM}(\mu) = \begin{pmatrix} 1.8089 \times 10^{-1} & 5.6284 \times 10^{-5} & 1.3982 \times 10^{-1} \\ 4.8104 \times 10^{-4} & 2.5500 \times 10^{-1} & 6.3694 \times 10^{-5} \\ 1.1756 \times 10^{-1} & 3.1775 \times 10^{-3} & 6.5296 \times 10^{-2} \end{pmatrix},$$

$$A_{RM}(\xi) = \begin{pmatrix} 3.2927 \times 10^{-3} & 1.0327 \times 10^{-1} & 1.6204 \times 10^{-3} \\ 1.0999 \times 10^{-1} & 3.8406 \times 10^{-3} & 5.2166 \times 10^{-1} \\ 4.4965 \times 10^{-5} & 9.7271 \times 10^{-1} & 7.6016 \times 10^{-4} \end{pmatrix},$$

$$A_{RM}(\zeta) = \begin{pmatrix} 2.0802 \times 10^{-3} & 2.5538 \times 10^{-1} & 6.0768 \times 10^{-4} \\ 2.3189 \times 10^{-1} & 1.1890 \times 10^{-3} & 1.1775 \times 10^{0} \\ 2.0666 \times 10^{-3} & 1.1604 \times 10^{0} & 1.1904 \times 10^{-3} \end{pmatrix},$$

We see that most components have an averaged relative mismatch smaller than 0.025.
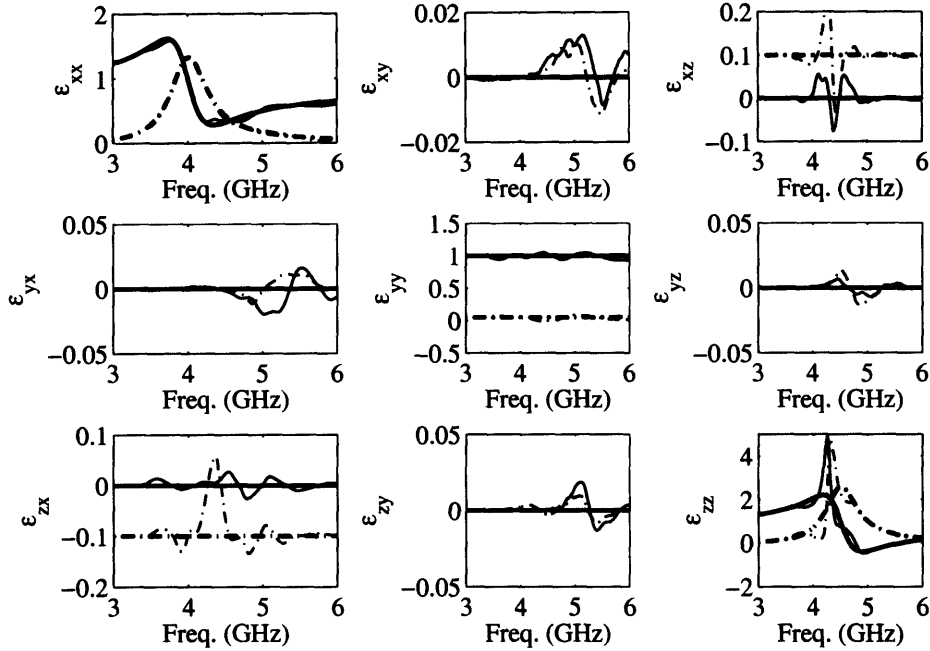
Figure 4-6: Comparison of the retrieved and the true $\bar{\bar{\epsilon}}$ of an Omegaferrite medium (clean data). The solid and dotted-dashed lines are for the real and imaginary parts, respectively. The thick and thin lines are for the true and the retrieved results, respectively.

4.5 Conclusion

An optimization approach is used to retrieve the constitutive parameters of slab of general bianisotropic medium from the knowledge of the reflection and transmission data. The method is for either rotated media with known constitutive properties or more general media with unknown constitutive properties. High dimensional inverse problems are attacked by the combination of differential evolution algorithm and simplex method. DE is used first to parallel explore the searching spacing and then simplex method is applied to accelerate the convergence. Fewer incidences are used in DE in order to reduce the computation burden and diverse incidences are used in simplex method in order to obtain the unique solution. Importantly, our method obtains a group of solutions, all of which are almost identical to the true one. Linear extrapolation of the results at the previous two frequencies are used as an initial guess for the retrieval of dispersive medium using simplex optimization method. Both clean and noisy data are tested. Optimization results show that the

86
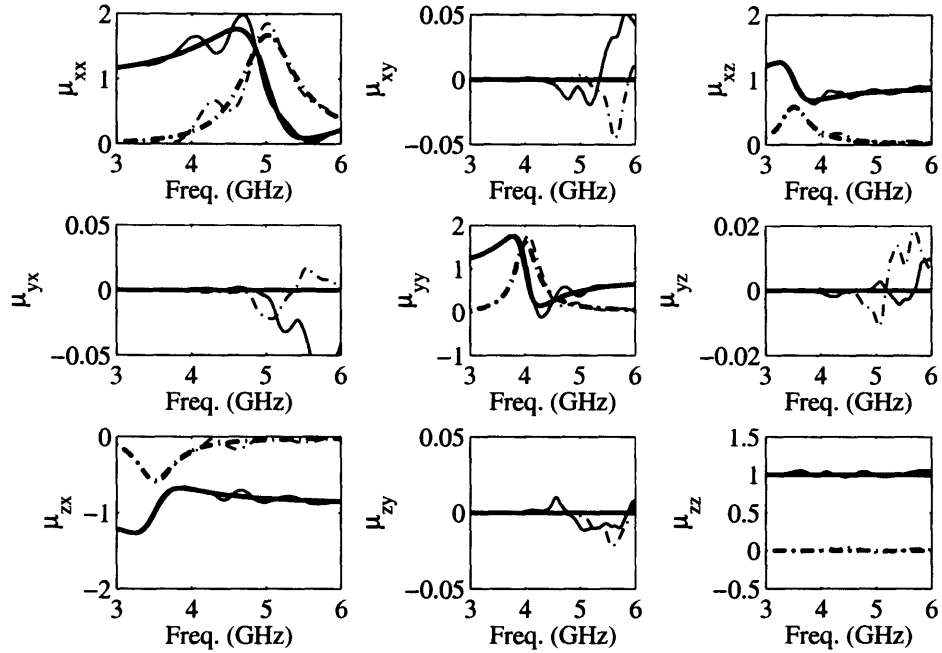
Figure 4-7: Comparison of the retrieved and the true $\bar{\bar{\mu}}$ of an Omegaferrite medium (clean data). The solid and dotted-dashed lines are for the real and imaginary parts, respectively. The thick and thin lines are for the true and the retrieved results, respectively.

constitutive parameters are reconstructed successfully. It should be noted that slabs with different thickness should be used for the broad-band retrieval. The limitation of the proposed method is that it cannot deal with the bianisotropic media whose cross-polarization terms are not close to zero at low frequencies.
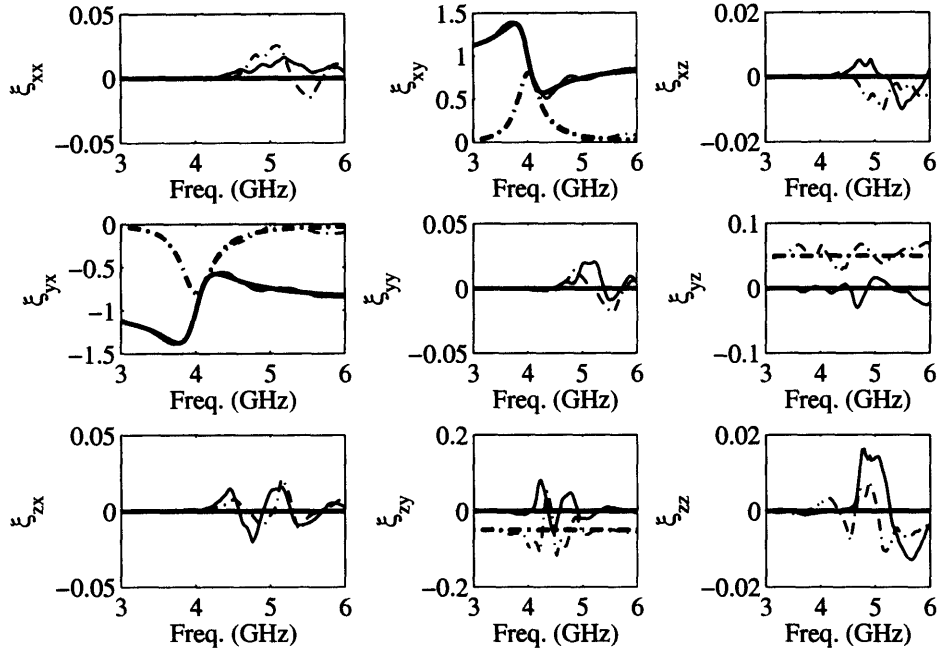
Figure 4-8: Comparison of the retrieved and the true $\bar{\bar{\xi}}$ of an Omegaferrite medium (clean data). The solid and dotted-dashed lines are for the real and imaginary parts, respectively. The thick and thin lines are for the true and the retrieved results, respectively.
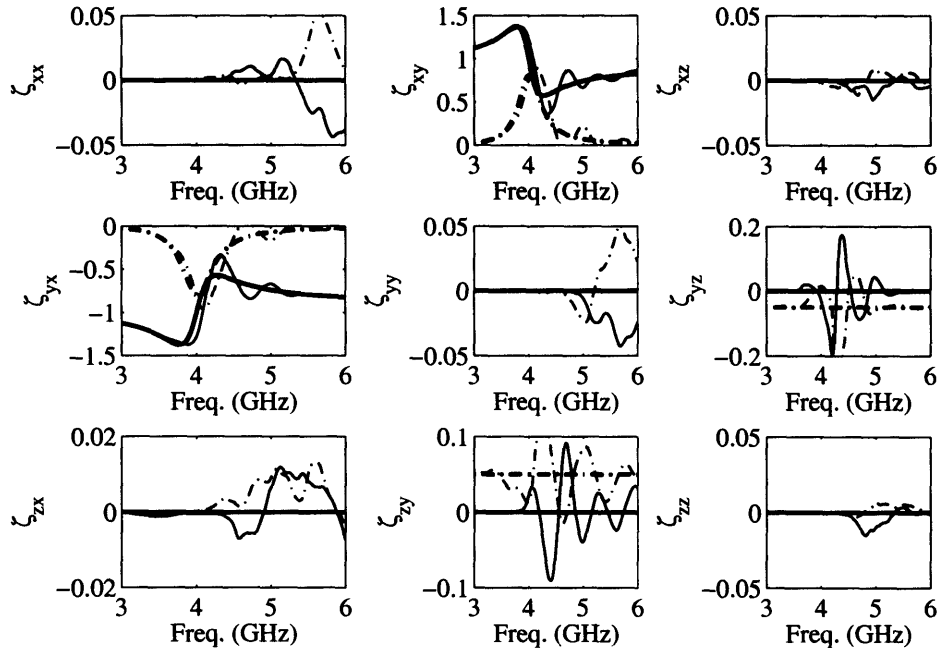
Figure 4-9: Comparison of the retrieved and the true $\bar{\bar{\zeta}}$ of an Omegaferrite medium (clean data). The solid and dotted-dashed lines are for the real and imaginary parts, respectively. The thick and thin lines are for the true and the retrieved results, respectively.
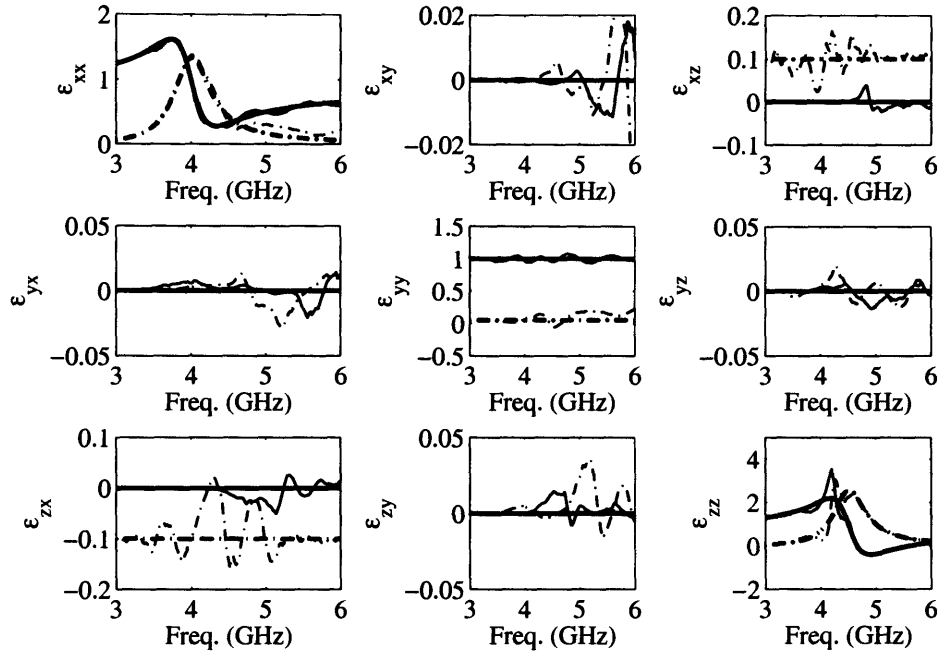
Figure 4-10: Comparison of the retrieved and the true $\overline{\overline{\epsilon}}$ of an Omegaferrite medium (2% noise). The solid and dotted-dashed lines are for the real and imaginary parts, respectively. The thick and thin lines are for the true and the retrieved results, respectively.
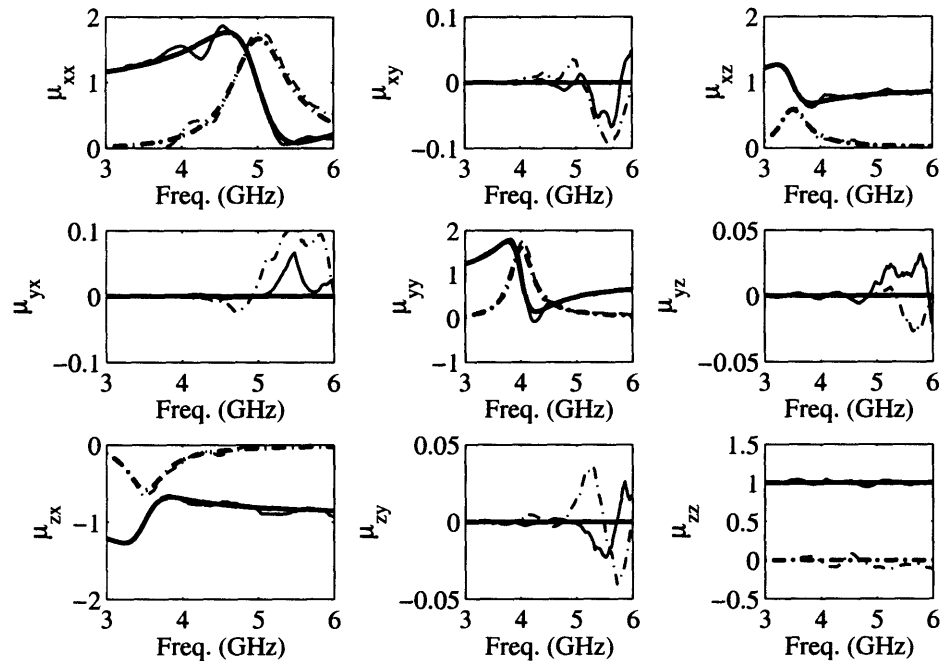
Figure 4-11: Comparison of the retrieved and the true $\overline{\overline{\mu}}$ of an Omegaferrite medium (2% noise). The solid and dotted-dashed lines are for the real and imaginary parts, respectively. The thick and thin lines are for the true and the retrieved results, respectively.
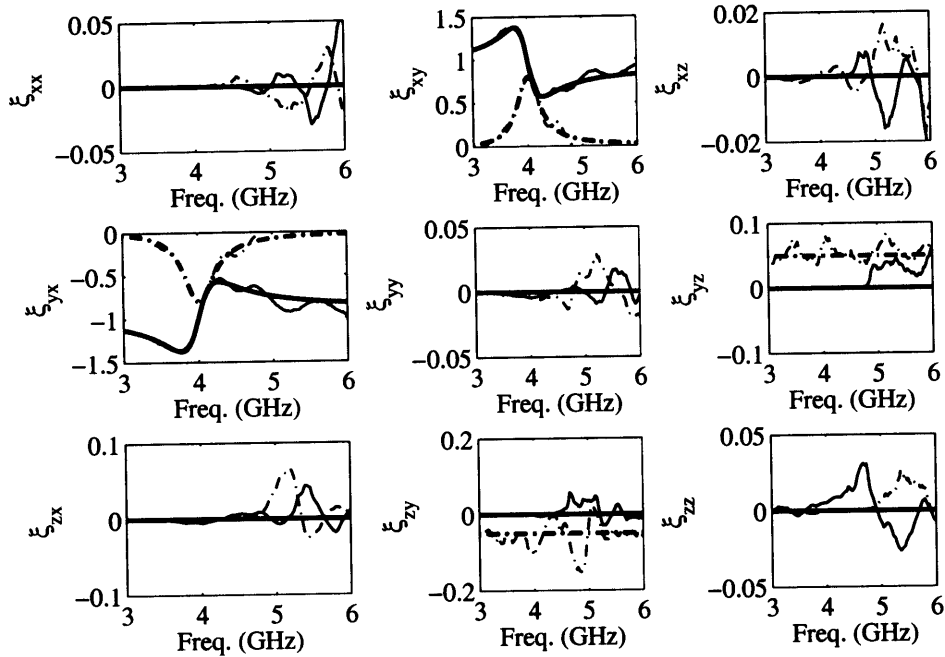
Figure 4-12: Comparison of the retrieved and the true $\overline{\overline{\xi}}$ of an Omegaferrite medium (2% noise). The solid and dotted-dashed lines are for the real and imaginary parts, respectively. The thick and thin lines are for the true and the retrieved results, respectively.
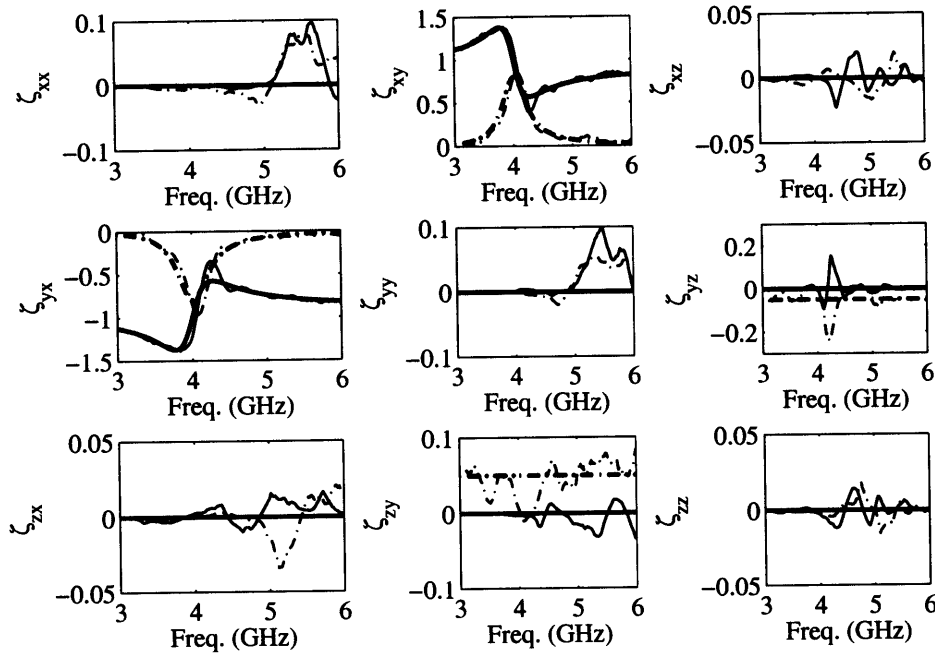
Figure 4-13: Comparison of the retrieved and the true $\overline{\overline{\zeta}}$ of an Omegaferrite medium (2% noise). The solid and dotted-dashed lines are for the real and imaginary parts, respectively. The thick and thin lines are for the true and the retrieved results, respectively.
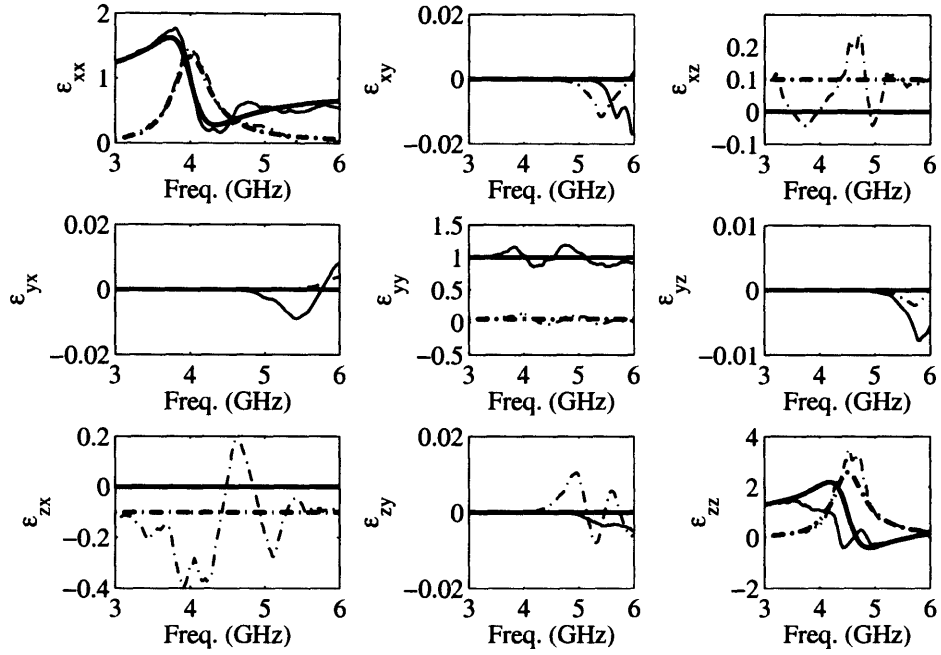
Figure 4-14: Comparison of the retrieved and the true $\bar{\bar{\epsilon}}$ of an Omegaferrite medium (5% noise). The solid and dotted-dashed lines are for the real and imaginary parts, respectively. The thick and thin lines are for the true and the retrieved results, respectively.
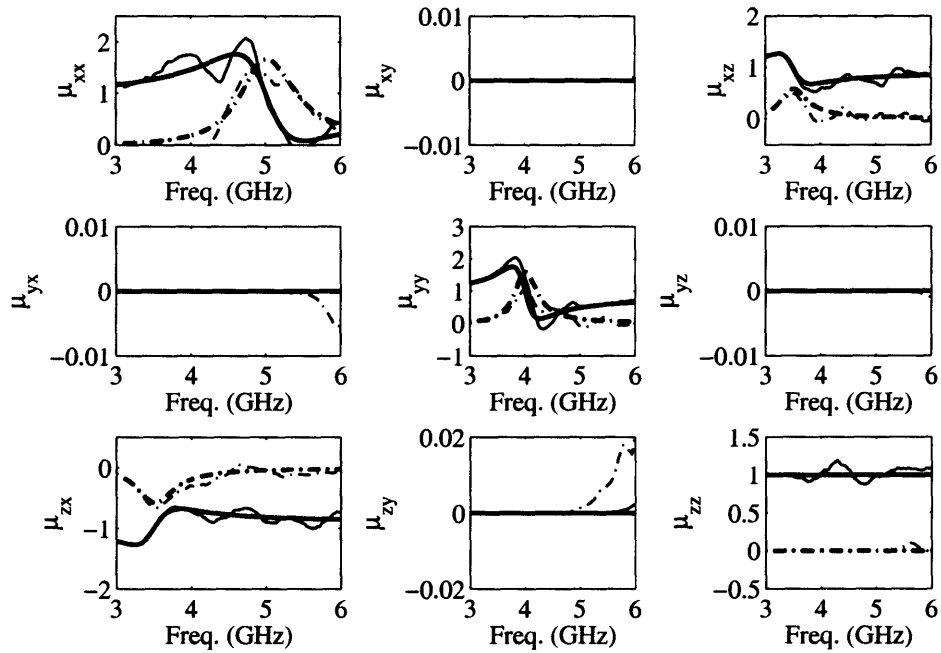
Figure 4-15: Comparison of the retrieved and the true $\bar{\bar{\mu}}$ of an Omegaferrite medium (5% noise). The solid and dotted-dashed lines are for the real and imaginary parts, respectively. The thick and thin lines are for the true and the retrieved results, respectively.

91
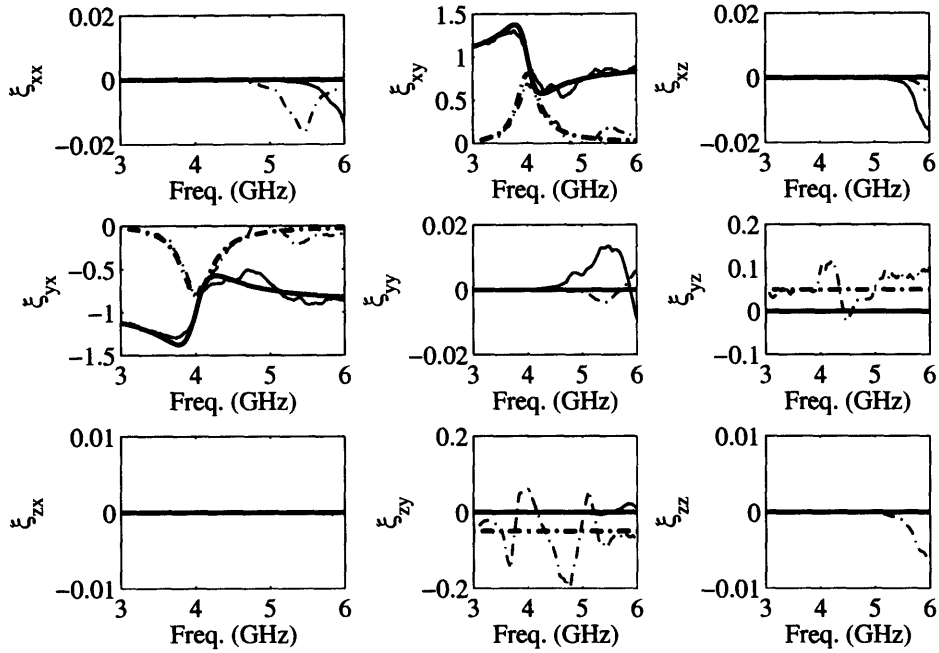
Figure 4-16: Comparison of the retrieved and the true $\overline{\overline{\xi}}$ of an Omegaferrite medium (5% noise). The solid and dotted-dashed lines are for the real and imaginary parts, respectively. The thick and thin lines are for the true and the retrieved results, respectively.
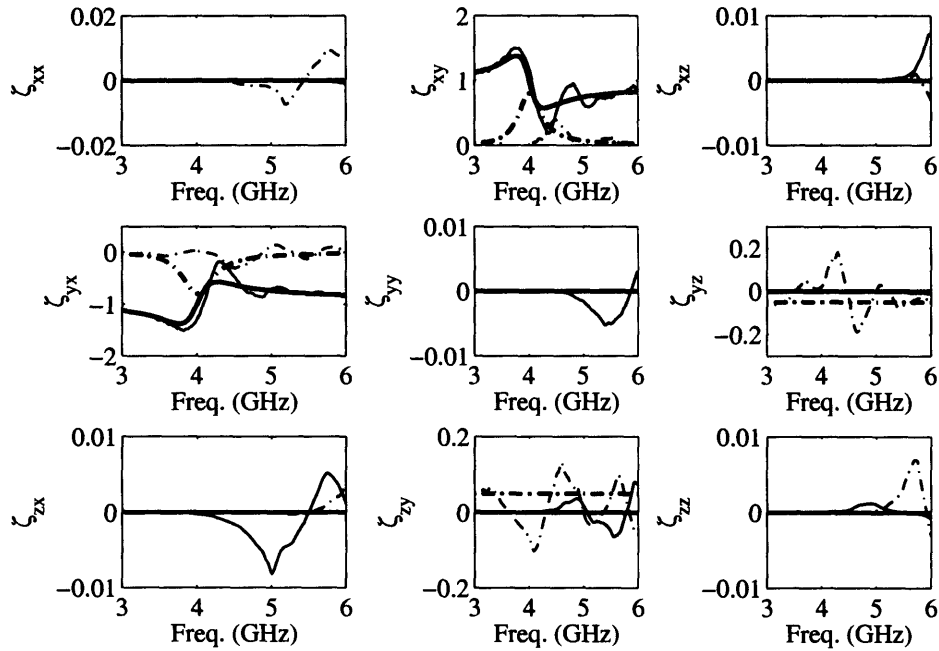
Figure 4-17: Comparison of the retrieved and the true $\overline{\overline{\zeta}}$ of an Omegaferrite medium (5% noise). The solid and dotted-dashed lines are for the real and imaginary parts, respectively. The thick and thin lines are for the true and the retrieved results, respectively.

Chapter 5

Application of a spheroidal mode approach in the detection and discrimination of buried objects

5.1 Introduction

The detection and removal of buried unexploded ordnance (UXO) is an important environmental problem, made very expensive and challenging by the high false alarm rate. Among the techniques for detecting UXOs, electromagnetic induction (EMI) is promising and has been widely explored [10, 11, 12, 13, 14, 15, 17, 18, 19, 63, 64, 65, 66, 67]. Many numerical techniques are available for EMI calculation in the magneto-quasistatic regime. Two of the most widely used models that work well for simple structures are (1) the dipole model [10, 16], in which one approximates the response of an object with one or a number of independently responding magnetic dipoles, and (2) sphere models [17], in which one approximates the object with a sphere. But many objects are complicated enough so that it is impossible or very difficult to approximate them with independent dipoles or spheres so that we need to resort to more complicated analytical geometries. Spheroidal mode approach is chosen in this work because the spheroidal coordinate system can be made to conform to the general shape of an object of interest, whether flattened or elongated, and

many of our objects of interest are bodies of revolution. Further more, the response of any discrete scatterer (including non-spheroidal objects) can be represented in terms of basic mode solutions in spheroidal coordinate system.

This chapter is organized as follows. The spheroidal mode approach is first introduced. Then we investigate the inversion of a single spheroidal object. Retrieval of the characteristic scattering coefficients from both the clean and the noisy synthetic data is addressed, and subsequently the inversion from the measurement data is presented. Finally, the characteristic scattering coefficients are used in pattern matching and classification.

5.2   Spheroid mode approach

In the frequency band we are considering (a few Hz up to a few 100 kHz), both conduction and displacement currents have a negligible influence in the relatively small region illuminated by the sensor around a sizable metallic scatterer. While the magnetic field $\overline{H}(\overline{r})$ in the metallic scatterer satisfies the Helmholtz equation, the magnetic field in the ground around the scatterer is irrotational. It can be expressed in terms of the gradient of a scalar potential, governed by the Laplace equation [68]. This applies to both the primary (transmitted) and secondary (scattered) fields. Thus, outside of the scatterer, we use a linear superposition of a finite number of basic solution modes to express both excitation and response, where each mode corresponds to a solution of the Laplace equation in spheroidal coordinates. This is an extension of the previous work [27] in which only the primary field is expressed using spheroidal modes.
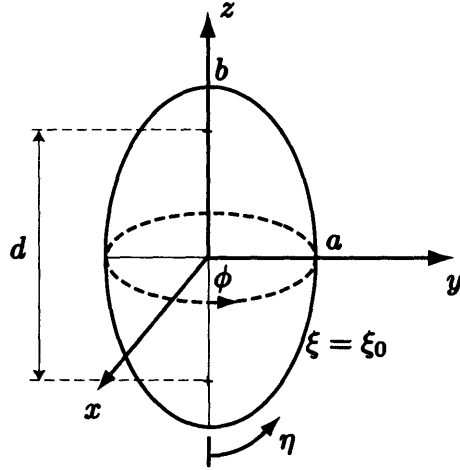
Figure 5-1: The prolate spheroidal coordinate system is specified by (η, ξ, ϕ), with $-1 \leq \eta \leq 1$, $1 \leq \xi \leq \infty$, and $0 \leq \phi < 2\pi$. The surface of a spheroid is given by $\xi = \xi_0 = b/\sqrt{b^2 - a^2}$, where a and b are minor and major semi-axis of the spheroid. The interfocal distance is given by $d = 2\sqrt{b^2 - a^2}$.

5.2.1 Formulation

In a prolate spheroidal coordinate system (see Fig. 5-1), the primary and secondary field potentials are respectively expressed by [69]:

$$
\begin{aligned}
U^{PR}(\bar{r}) &= \frac{d}{2} \sum_{m=0}^{\infty} \sum_{n=m}^{\infty} \sum_{p=0}^{1} b_{pmn} P_n^m(\eta) P_n^m(\xi) T_{pm}(\phi) \\
&\equiv \frac{d}{2} \sum_j b_j \Psi_j^{PR}(\bar{r}),
\end{aligned}
\tag{5.1}
$$

$$
\begin{aligned}
U^S(\bar{r}) &= \frac{d}{2} \sum_{m=0}^{\infty} \sum_{n=m}^{\infty} \sum_{p=0}^{1} B_{pmn} P_n^m(\eta) Q_n^m(\xi) T_{pm}(\phi) \\
&\equiv \frac{d}{2} \sum_k B_k \Psi_k^S(\bar{r}),
\end{aligned}
\tag{5.2}
$$

where d is the interfocal distance of the spheroidal coordinate system, j, k index the set $\{p, m, n\}$ and

$$
T_{pm}(\phi) = \begin{cases} \cos(m\phi), & p = 0, \\ \sin(m\phi), & p = 1. \end{cases}
$$

$P_n^m(\cdot)$ and $Q_n^m(\cdot)$ are the associated Legendre functions of the first and second kind, respectively. A time dependence of $e^{-i\omega t}$ is assumed and suppressed throughout. The primary and secondary fields are represented respectively as:

$$\overline{H}^{PR}(\overline{r}) = \frac{-d}{2} \sum_j b_j \nabla \Psi_j^{PR}(\overline{r}), \tag{5.3}$$

$$\overline{H}^S(\overline{r}) = \sum_j b_j \overline{H}_j^S(\overline{r}) = \sum_j b_j \sum_k \frac{-d}{2} B_k^{(j)} \nabla \Psi_k^S(\overline{r}), \tag{5.4}$$

where ∇ denotes the gradient operator. The coefficient b_j represents the strength of the jth primary field mode, while the coefficient $B_k^{(j)}$ represents the strength of the kth mode in the secondary field, in response to a unitary magnitude of the jth excitation mode in the primary field. Note that $\sum_j b_j B_k^{(j)}$ in Eq. (5.4) is equal to B_k in Eq. (5.2). The lower primary field modes are $(p, m, n) = (0, 0, 1), (0, 1, 1), (1, 1, 1)$, which correspond to unitary uniform excitation in the $-\hat{z}$, $\hat{x}$ and $\hat{y}$ direction, respectively.

In the laboratory coordinate system where the measurements are carried out, if the spheroidal object is not located at the origin or aligned with the z axis, a self coordinate system has to be defined based on the location and orientation of the spheroid, in which the spheroidal mode approach can be used. The secondary field clearly depends on the properties of the source, the position of measurement, and the location, orientation, size, shape, and composition material of the scatterer. In Eq. (5.4), $\nabla \Psi_k^S(\overline{r})$ is determined by the position of the measurement. The coefficients b_j depend on the characteristics of the transmitter and the location and orientation of the object, and $B_k^{(j)}$ is determined by the shape, size and composition of the object. We denote the parameters that the coefficients b_j depend on as p_b, and the parameters that the coefficients $B_k^{(j)}$ depend on as p_B. We observe that coefficients $B_k^{(j)}$ are determined by the intrinsic properties of the object and are independent of its location and orientation as the coordinate system is attached to the object. It can be proved mathematically [68, 70] that each object has a unique set of $B_k^{(j)}$ in a given spheroidal coordinate system. Thus in principle one can recognize an object from its set of $B_k^{(j)}$. Of course, if two different objects produce similar scattered fields, or if sampling is insufficient to reveal the differences in their scattered fields, the objects will

be indistinguishable in terms of $B_k^{(j)}$ as well. However, any significant difference in the scattered field data necessarily implies a difference somewhere in the set of $B_k^{(j)}$, because of the orthogonality of the associated functions.

In what follows, we address some theoretical and practical issues of the spheroidal mode approach, i.e., dealing with non-spheroidal objects, the choice of interfocal distance d of the spheroidal coordinate system, the properties of the basic spheroidal modes, and the ordering of the primary and the secondary modes.

5.2.2 Dealing with a non-spheroidal object

Note that the object in the spheroidal coordinate system is not itself necessarily a spheroid. For a general scatterer, we choose a fictitious spheroidal surface $\xi = \xi_0$ enclosing the object (see Fig. 5-2) strictly for computational purposes. The primary and secondary fields on and outside the fictitious surface are expressed by Eq. (5.3) and Eq. (5.4). We conclude from the uniqueness of the solution and the orthogonality of the modes that the coefficients b_j and $B_k^{(j)}$ in Eq. (5.3) and Eq. (5.4) are independent of the size of the enclosing spheroidal surface (ξ_0) and are unique in a given spheroidal coordinate system, i.e., the interfocal distance d is fixed [68, 70].
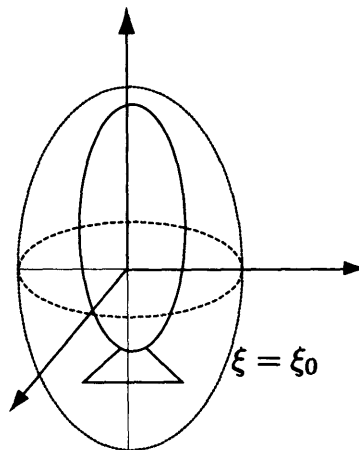
Figure 5-2: An example of a non-spheroidal object surrounded by a spheroidal surface corresponding to a particular "radial" coordinate value $\xi = \xi_0$ in the prolate spheroidal coordinate system chosen.

5.2.3 Choice of the interfocal distance

To proceed, we must choose a particular d to define the coordinate system. For a given object, the logical choice would be a value similar to its longest dimension, for an elongated object in a prolate system; or the shortest dimension, for a flattened object in an oblate system. Since most UXOs are elongated objects, we only consider the prolate system in the examples here. In principle, different d can be used for different objects considered in the same problem. This could be advantageous if we do not wish to examine or compare either the input or induced modal coefficients (b_j, $B_k^{(j)}$), but only need a forward solution system for obtaining $\overline{H}$. The advantage of proceeding in a single spheroidal coordinate system is that it allows us to examine and compare the $B_k^{(j)}$ themselves, as discriminators.

5.2.4 Properties of the spheroidal modes

From the properties of the trigonometric functions and the associated Legendre functions of the first kind, we find that the spheroidal modes have the following properties:

- For both the primary and the secondary potentials, the integer m and n determine their spatial distribution properties. From the periodic properties of the sine and cosine functions, we see that m represents the number of periods for $\phi \in [0, 2\pi]$. From the properties of the associated Legendre function of the first kind, we conclude that $n - m$ represents the number of the zeros for $\eta \in (-1, 1)$.

- For an object that is symmetric about the xy plane, when excitation is (0, 1, 1), i.e., uniform fields in the x direction, the coefficients $B_{p,m,n}^{(0,1,1)}$ are nonzero only when $n - m$ is even due to the property of the associated Legendre function of the first kind,

$$P_n^m(-\eta) = (-1)^{n-m} P_n^m(\eta).$$

The conclusion is also true for the (1, 1, 1) excitation.

- For a body of revolution (BOR), when the excitation mode is (0, 0, 1), i.e., uniform fields in the $-z$ direction, the coefficients $B_{p,m,n}^{(0,0,1)}$ are nonzero only when $p = 0$ and

98

$m = 0$, which means we expect no variation with respect to ϕ in the secondary field. More generally, making use of the orthogonality property of $\cos m\phi$ and $\sin m\phi$, we conclude that (p', m', n') primary mode excites only (p', m', n) secondary modes, i.e., those secondary modes with different p or m from the primary mode are eliminated.

- For a BOR, the scattering coefficients satisfy the following equation:

$$B_{0,1,n}^{(0,1,n')} = B_{1,1,n}^{(1,1,n')}$$

This is explained by the rotation of the spheroidal coordinate system by $\frac{\pi}{2}$ around the z axis:

$$\cos(\phi) = \sin(\phi + \frac{\pi}{2}) \equiv \sin(\phi').$$

More generally, by rotating the spheroidal coordinate system by $\frac{\pi}{2m'}$ around the z axis, we have

$$B_{0,m',n}^{(0,m',n')} = B_{1,m',n}^{(1,m',n')}. \tag{5.5}$$

5.2.5 Ordering the primary and the secondary modes

Eqs. (5.3) and (5.4) contain an infinite number of the primary and secondary modes. In practice, however, we have to use a truncated version of them. Here we address the issue of ordering the finite collection of primary and secondary modes.

Index of the primary mode (j)

Consider a finite number of primary modes ($j = \{p, m, n\}$): $p = \{0, 1\}$, $\{m = 0, 1, \ldots, M\}$, and $\{n = m, m + 1, \ldots, N\}$. A total number of $N + [N + (N - M + 1)] \cdot M$ modes are listed in Table 5.1:

We order them according to the following criteria,

- the index starts from 1 for the mode b_{001},

- in the same row, the index is increased by 1 for the next mode,

Table 5.1: Index of mode j for the primary field

	n=1		n=2		$\cdots$	n=M		$\cdots$	n=N	
m=0	b_{001}		b_{002}		$\cdots$	b_{00M}		$\cdots$	b_{00N}	
m=1	b_{011}	b_{111}	b_{012}	b_{112}	$\cdots$	b_{01M}	b_{11M}	$\cdots$	b_{01N}	b_{11N}
m=2			b_{022}	b_{122}	$\cdots$	b_{02M}	b_{12M}	$\cdots$	b_{02N}	b_{12N}
$\vdots$					$\ddots$	$\vdots$	$\vdots$	$\ddots$	$\vdots$	$\vdots$
m=M					$\cdots$	b_{0MM}	b_{1MM}	$\cdots$	b_{0MN}	b_{1MN}

- the index of the first mode in a row increases by 1 compared with that of the last mode in the previous row.

Index of the secondary mode (k)

For the same (p, m, n), the index of k is greater than that of j by one because the index of k starts from one for the mode B_{000}. The reason for this difference is that the $\{0, 0, 0\}$ primary mode potential is expressed by $P_0(\xi)$, which is always equal to one, having no contribution to the magnetic fields, while the secondary mode $Q_0(\xi)$ is not a constant potential.

5.2.6 Relationship between the spheroidal mode approach and the dipole approximation approach

In the the low frequency band where the EMI is applied, the magnetic field around a metallic object is irrotational, and can be expressed as the gradient of a scalar potential, governed by the Laplace equation [68]. If the potential is expressed in a spherical coordinate system, we get a multipole expansion, with the first term dipole, the second term quadrupole, etc [68]. When the observation is far from the metallic object, the secondary field can be well approximated by a dipole model, with the quadrupole and higher terms neglected. On the other hand, sphere is a special ellipsoid: when the interfocal distance d approaches to zeros, the length of the major axis is equation to that of the minor axis. In this case, by keeping the lower modes we reduce the spheroidal mode approach to the dipole approximation approach: modes B_{011}, B_{111} and B_{001} correspond to the dipole components in x, y and z directions, respectively [69].
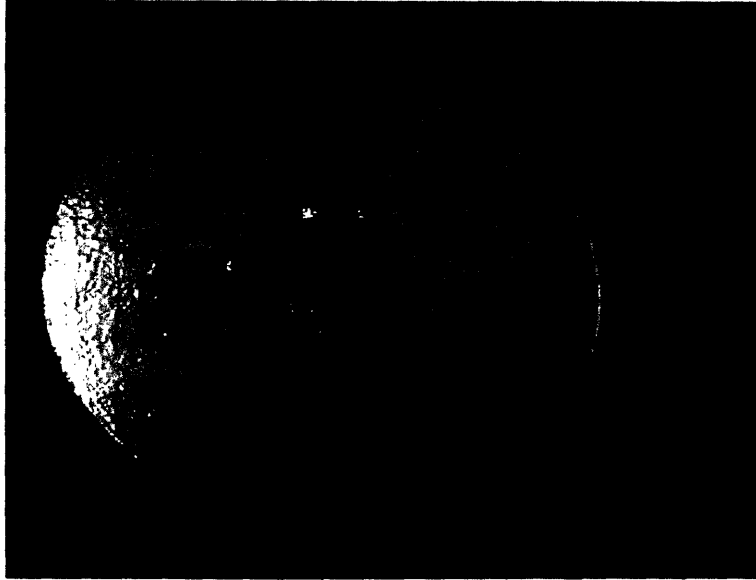
Figure 5-3: Geophex GEM-3 instrument sensor head (Courtesy of Dr. K. O'Neill)

5.3 Electromagnetic induction sensor

The measurement data used in this work were obtained using the GEM-3 electromagnetic sensor. This sensor was developed by Geophex Inc. and has been widely used for detecting and characterizing buried metallic objects [10, 63, 17]. The picture of the GEM-3 is shown in Fig. 5-3. The GEM-3 is a monostatic sensor characterized by a zero source -receiver separation. The sensor head of the GEM-3 contains two concentric transmitting current loops with radii of approximately 20 cm and 10 cm. The total current in the inner loop is one half of that in the outer loop and flows in the opposite direction. Therefore, the primary fields at the center, where the receiver is placed, are nearly zero. The frequency range of the GEM-3 is roughly between 30 Hz and 24 kHz.

During the measurement, in order to minimize variance due to sensor position, the GEM-3's position and orientation is fixed. Test objects are placed upon a supporting wooden platform that is built around the GEM-3 instrument. Whenever test objects are moved to a new position on the wooden platform, their induced magnetic fields are measured by the GEM-3 sensor. The accuracy of the measurement was tested by a previous group member in his work [11, 12], where the measured responses of spheroidal objects

are compared with those obtained by an analytically approach. The results show that the measurement data taken by the GEM-3 are reliable at frequencies up to about 12 kHz, with decreasing accuracy at higher frequencies. Note that all the measurements reported in the thesis were taken by Dr. Kevin O'Neill's group at Hanover, NH.

5.4 Inversion for a single spheroidal object

It has been shown that many realistic elongated objects can be approximated as prolate spheroids [27]. In this section, we investigate a spheroidal object or equivalently an elongated object with a response that can be well-approximated by that of a spheroid. For a single spheroid or an equivalent spheroid, the vector p_B is $\{2a, 2b, \mu_r, \sigma\}$, where $2a$ and $2b$ are the length of minor and major axis, respectively, μ_r is the relative magnetic permeability, and σ is the conductivity of the object. For a given source, the vector p_b depends on the location and the orientation of the object. As a robust optimization scheme, differential evolution is applied to search for the set of trial parameters $\{p_b, p_B\}$ that produce the values of $\overline{H}^s$ in Eq. (5.4) that best match the observed data. For each trial $\{p_b, p_B\}$, the forward process calculating the secondary field is executed. An essential step in the forward process is the application of the coefficients $B_k^{(j)}$ obtained by an analytical approach [11, 12, 67].

First, we run numerical simulations to determine the parameters of a hypothetical spheroid illuminated by a uniform primary field. Fig. 5-4 illustrates the setup of the single spheroid inversion problem. In the laboratory coordinate system, the spheroid is located at $\overline{r}_0 \equiv (x_0, y_0, z_0)$, which is $(0, 0, -0.55)$ m in the simulation. The orientation of the spheroid is defined by the Euler angles (θ_0, ϕ_0), which are $(\frac{2\pi}{3}, \frac{5\pi}{4})$. A self coordinate system is defined by the location and orientation of the spheroid, in which a spheroidal mode approach introduced in section 5.2 can be used. Other parameters of the spheroid are as follows: $2a = 0.05$ m, $2b = 0.20$ m, $\mu_r = 100$, $\sigma = 3 \times 10^6$ S/m. Here we choose a mono-static model, i.e., the source and the observation positions are the same. The uniform primary field sent out from measurement position $\overline{r}_m$ is $\overline{H}^{PR}(\overline{r}) = (\overline{r}_m - \overline{r}_0)H_0$, where H_0 is a constant. The magnetic field (x, y, z components) is "measured" on a 5 by 5 grid ($x = 0.2 \times (i - 3), y = 0.2 \times (j - 3)$, $i, j = 1, 2, ..., 5$) at the height $z = 0$. In the

current simulation model, first we compute the forward problem, calculating the secondary field produced by the spheroid. Then in the inverse problem, we treat the calculated secondary fields as the "measured" fields. We treat the conductivity σ as a known parameter in this simulation and assume that the x and y coordinates of the spheroid have been estimated by another sensor type, such as ground penetrating radar [71]. The task is to find the parameters of the trial spheroid $(z_0, \theta_0, \phi_0, 2a, 2b, \mu_r)$ so that the secondary fields produced by the trial spheroid match the "measured" fields as closely as possible. The sample frequencies are chosen to be 40 Hz, 500 Hz, 10 kHz, and 1 MHz.
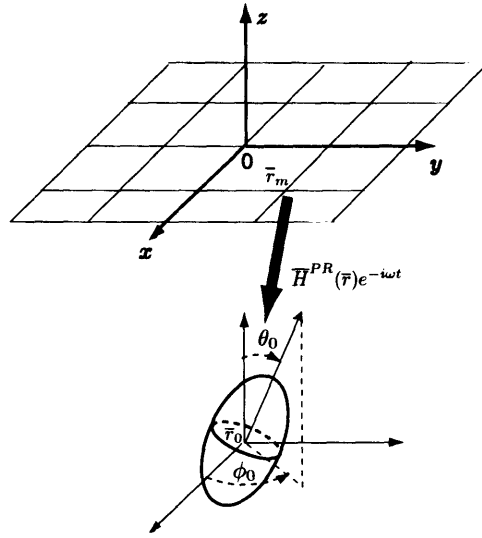
Figure 5-4: Illustration of the setup of the single spheroid inversion problem

The mathematical optimization model is expressed as

$$\min \quad f(\overline{X}) = \frac{1}{N_d N_f} \sum_{s=1}^{N_d} \sum_{t=1}^{N_f} \frac{1}{\max\{\delta, |\overline{H}^S_{\mathrm{d}(s,t)}(\overline{X})|\}} |\overline{H}^S_{\mathrm{m}(s,t)}(\overline{X}) - \overline{H}^S_{\mathrm{d}(s,t)}(\overline{X})| \quad (5.6)$$

$$\text{s.t.} \quad X_i^{\min} \leq X_i \leq X_i^{\max}, \qquad i = 1, 2, \ldots N_u,$$

where N_d is the total number of measurement points, N_f is the total number of sample frequencies, N_u is the total number of unknowns, $\overline{H}^S_{\mathrm{d}}$ is the data of the measured field, and δ is a small positive number (which is one percent of the maximum magnitude of the measured magnetic field in the simulation) that avoids infinite weighting for too small

103

Table 5.2: Comparison of the optimized and theoretical data in the numerical model.

	z_0 [m]	θ_0	ϕ_0	$2a$ [m]	$2b$ [m]	μ_r
Theoretical value	−0.55	2.09 ($= \frac{2}{3}\pi$)	3.93 ($= \frac{5}{4}\pi$)	0.050	0.20	100.0
Optimized value	−0.54	2.07	3.93	0.051	0.19	107.5

$|\overline{H}_d^S|$. Note we have transformed $\overline{H}_m^S$ calculated by the model Eq. (5.4) to the value in the laboratory coordinates. In this simulation, $\overline{X} = (z_0, \theta_0, \phi_0, 2a, 2b, \mu_r)$. The objective function $f(\overline{X})$ expresses the average relative mismatch of the secondary fields and its value is zero in the ideal situation.

Differential evolution algorithm (DE) [36, 57] is applied to optimize the objective function. DE has been introduced in chapter 4 and is not repeated here. When DE is applied to the buried object detection, each individual is a vector consisting of the location, size, permeability etc. of the buried object. The individual producing a better match with the measured field wins in the "selection" operation. After 200 generations of optimization, with a population of 12 individuals in each generation, DE gives the results shown in Table 5.2.

The optimized objective function value is $f_{opt} = 0.031$, which means that the average mismatch between the measured data and the computed secondary field is of 3.1%. Some optimization trajectories are shown in Fig. 5-5 and Fig. 5-6 , in which the individual $\overline{X}$ of each generation that produces the smallest mismatch and its corresponding objective function values f are plotted. We can see from Fig. 5-5 and Fig. 5-6 that after about 150 generations of evolution, the optimized parameters are close to their true values, and the objective function value is less than 0.04.

Second, we apply the inversion method to deal with the data collected by the GEM-3 instrument [63]. The primary fields are calculated by the Biot-Savart's law and then are conveniently expressed in terms of fields from a collection of infinitesimal magnetics sources with analytical expressions [27]. The GEM-3 data in arbitrary units are converted to equivalent magnetic fields using the normalization method proposed in [11, 12]. The primary fields produced by the GEM-3 are nonuniform, and $b_j \neq 0$ for $n > 1$, where j indexes the set $\{p, m, n\}$. In order to find the secondary field in Eq. (5.4), we need

(a) z_0

(b) θ_0, ϕ_0

(c) $2a, 2b$

(d) μ_r
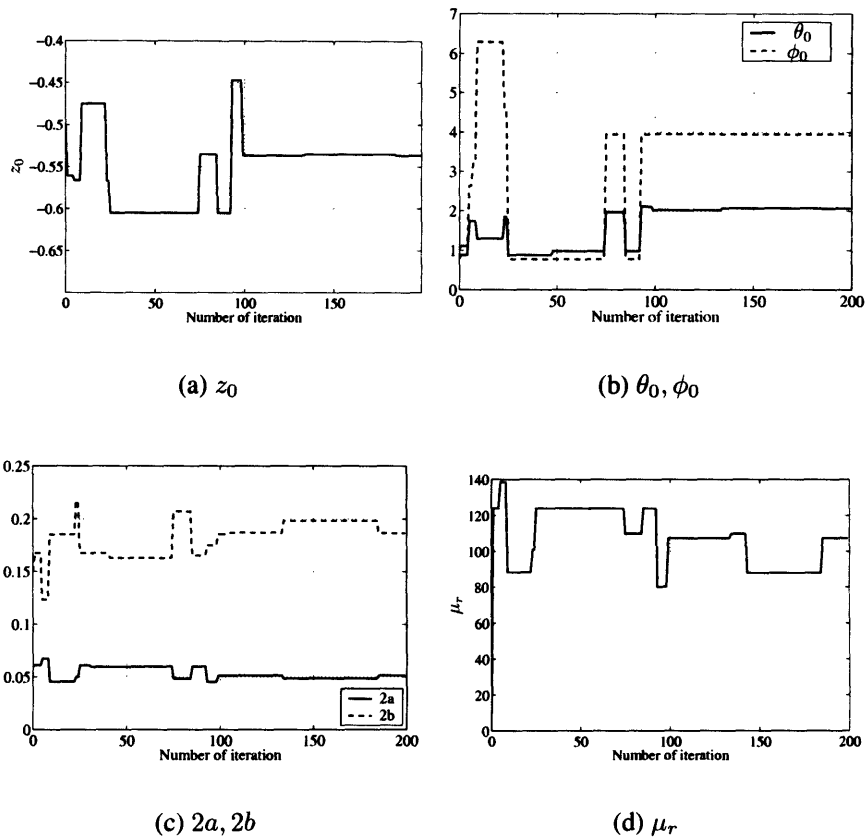
Figure 5-5: Optimization trajectory of parameters in the numerical model, in which the parameters of the hypothetical spheroid are $z_0 = -0.55$ m, $\theta_0 = \frac{2\pi}{3}(= 2.09)$, $\phi_0 = \frac{5\pi}{4}(= 3.93)$, $2a = 0.05$ m, $2b = 0.20$ m, and $\mu_r = 100$.
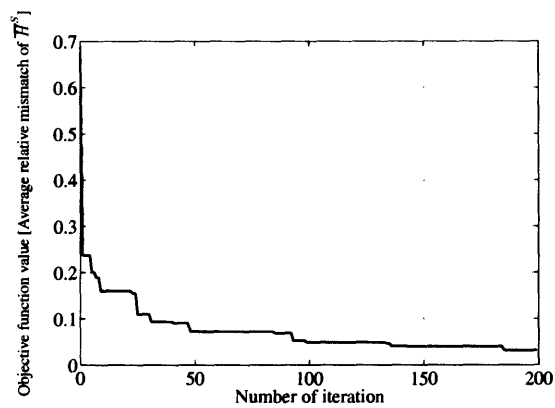
Figure 5-6: Trajectory of the optimized objective function value in the numerical model for the hypothetical spheroid.

105

Table 5.3: Comparison of the optimized and real data for spheroid A2 shown in Fig. 5-7.

	z_0 [m]	θ_0	ϕ_0	$2a$ [m]	$2b$ [m]	μ_r	σ [S/m]
Real value	−0.275	0	Any	0.03	0.09	1.0	$2 \times 10^7 \sim 5 \times 10^7$
Optimized value	−0.269	0.140	1.656	0.029	0.084	1.0	3.09×10^7

to calculate b_j for this source. One way to find the excitation coefficients is to utilize the orthogonality of the associated Legendre functions [27]. Although it is an accurate method, the computation entailed is somewhat burdensome for inversion routines: we must calculate a double integration with a rapidly oscillating integrand for each b_j. A faster method for obtaining the excitation coefficients is to solve for all b_j together in a linear equation system obtained by matching the primary field on a spheroidal surface defined by $\xi = \xi_0$. The point matching technique can be expressed by a truncated version of Eq. (5.3), with the maximum primary mode j being J. The contribution to the primary field from the modes after J is negligible. For this problem, we found the primary field modes j with $m > 3$ or $n > 5$, produce a negligible contribution compared with the leading modes. Note that the primary magnetic fields produced by the GEM-3 instrument are expressed in the self coordinate system. For N matching points and three (x, y, z) field components, there are $3N$ equations. When $3N > J$, the task of finding b_j is overdetermined and can be solved by a least squares method.

After obtaining b_j, DE is employed to optimize the objective function Eq. (5.6). For a real machined spheroid (see Fig. 5-7) [12, 11] with parameters $(z_0, \theta_0, \phi_0, 2a, 2b, \mu_r, \sigma) =$ (−0.275 m, 0, Any, 0.03 m, 0.09 m, 1, 2×10^7 S/m $\sim 5 \times 10^7$ S/m), we measured the secondary field at a grid of 4 by 4 ($x = 0.05 + 0.1 \times (i - 3), y = 0.05 + 0.1 \times (j - 3)$, $i, j =$ 1, 2, 3, 4) at the height $z = 0$ at the frequencies of 90, 150, 210, 330, 450, 510, 930, 2490, 6270, 10950 Hz. For this inversion problem with 7 parameters to be optimized, DE obtains the results shown in Table 5.3, using a population size of 20 and 100 iterations.

The optimized objective function value f_{opt} is 0.077. The comparison of optimized and measured broadband EMI response at point $\bar{r} = (0.05, 0.05, 0)$ m is shown in Fig. 5-8. Note that the choice of sign convention follows the convention common in the geophysics field in that the complex conjugate of the magnetic field is shown. We observe from Fig. 5-8

that the optimized results are close to the measured data.
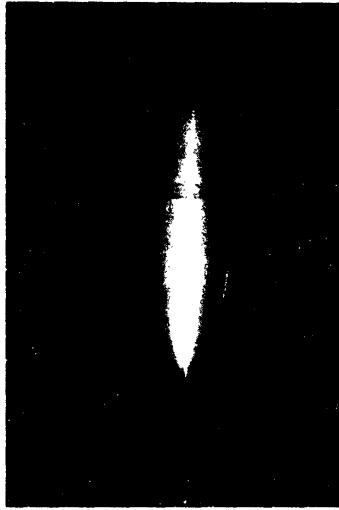
Figure 5-7: A real ellipsoid made of aluminum, with dimensions $2a = 0.03$ m, $2b = 0.09$ m, designated A2 (Courtesy of Dr. K. O'Neill).
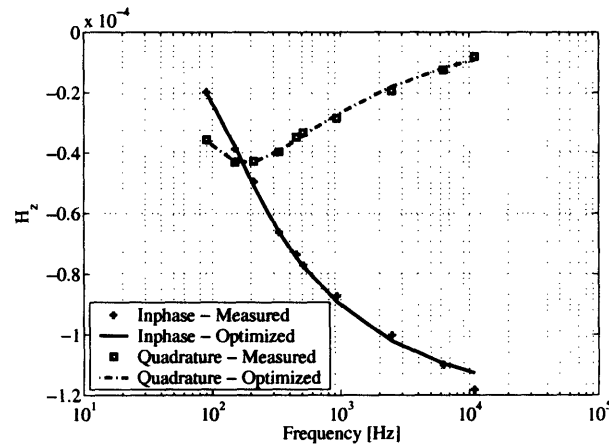
Figure 5-8: Comparison of the measured field and the optimized field at point $(x, y, z) = (0.05, 0.05, 0.0)$ m for the spheroid shown in Fig. 5-7.

5.5 Inversion from clean synthetic data

In this section, we present two examples in which the characteristic scattering coefficients are retrieved from the synthetic data. We first expand the secondary field produced by an oblate spheroid under a prolate spheroidal coordinate system. Then scattering coefficients of a composite object consisting of two coaxial spheroids are retrieved.

107

5.5.1 An oblate spheroid in a prolate spheroidal system

As mentioned in section 5.2.2, the spheroidal modes form a complete set so that the secondary fields produced by any scatterer can be uniquely expanded in a given spheroidal coordinate system, regardless of the shape and size of the object. In this example, we expand the secondary field produced by an oblate spheroid in a prolate spheroidal coordinate system.

The size of the oblate spheroid is $2a = 0.38$ (m) and $2b = 0.20$ (m), with an interfocal distance $d = 2\sqrt{a^2 - b^2} = 0.32311$ (m). The relative permeability of the spheroid is $\mu_r = 50$ and the conductivity is $\sigma = 1 \times 10^7$ (S/m). The spheroid is located at $\vec{r}_0 = (0, 0, -1.0)$ (m) with the rotation angle $\theta_0 = 0$ and $\phi_0 = 0$. Magnetic fields are measured at two levels ($z = 0$ and 0.3 (m)) on grids (11 by 11 points within $x = [-0.5, 0.5]$ (m) and $y = [-0.5, 0.5]$) (m) at the operating frequency 100 Hz. In the simulation, we choose a mono-static model, in which the uniform primary field is $\overline{H}^P(\vec{r}) = (\vec{r}_m - \vec{r}_0)H_0$, where $\vec{r}_0$ is where the spheroid is located, $\vec{r}_m$ is the measurement position, and H_0 is a constant. Thus, the primary field over the object is uniform for each $\vec{r}_m$.

The secondary fields are expanded as a linear combination of orthogonal modes in a prolate spheroidal coordinate system with the interfocal distance identical to that of the oblate spheroid under investigation.

In the numerical simulation, we choose $M = 1$, $N = 6$ for the secondary modes and $j = (0, 0, 1)$, $(0, 1, 1)$, $(1, 1, 1)$ for primary modes due to the uniform excitation.

The simulation results show that the fields at all measurement points are expanded correctly, which means that the secondary fields produced by an oblate spheroid can be expanded in a prolate spheroidal coordinate system. For comparison, the fields are also expanded in an oblate spheroidal coordinate system with the same interfocal distance.

The magnitudes of the scattering coefficients $B_k^{(j)}$ and the contribution of each mode to the total fields are shown in Figs. 5-9 and 5-10. We observe that for those non-zero secondary modes, as n increases, $B_k^{(j)}$ increases, Ψ_k^S decreases (due to the property of the associated Legendre function of the second kind), and the field contribution $B_k^{(j)} \nabla \Psi_k^S$ decreases.
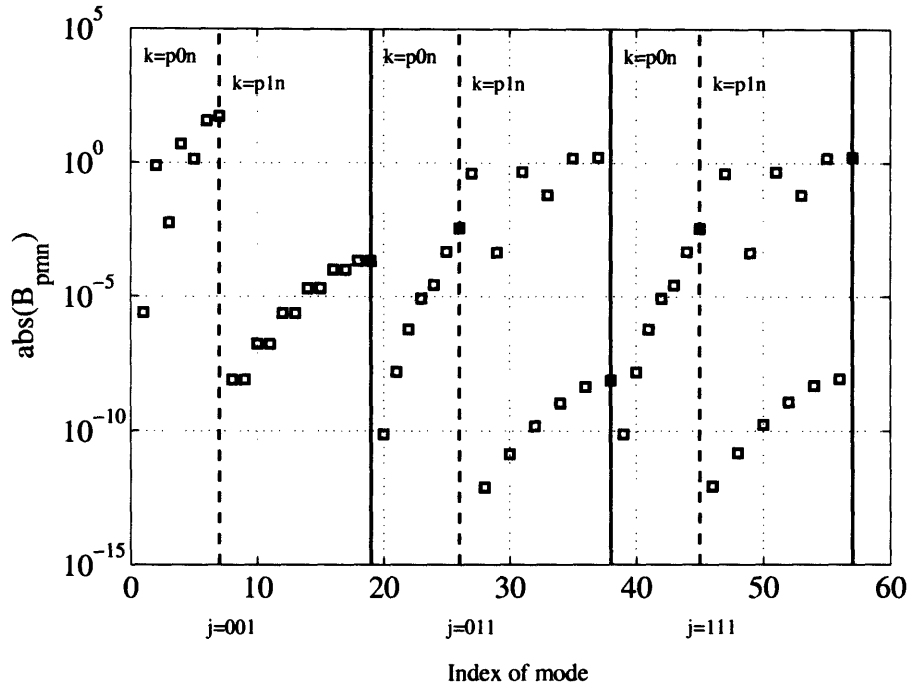
Figure 5-9: Magnitude of $B_k^{(j)}$ in the prolate coordinate system for the oblate spheroidal body

In comparison, the the fields are also expanded in an oblate spheroidal coordinate system with the same interfocal distance, as shown in Figs. 5-11 and 5-12. The same expansion properties are observed.

Comparing Fig. 5-10 and Fig. 5-12, we see that for the secondary field produced by the oblate spheroid, the series expanded in the oblate spheroid coordinate system converges faster than that in the prolate spheroid coordinate system.

5.5.2 Composite object

When the object is too complicated to be represented by a spheroid, we still express the primary and secondary fields on and outside a fictitious spheroidal enclosing surface in the same way. In other words, in the spheroidal coordinate system, we can obtain the coefficients b_j for the primary field and $B_k^{(j)}$ for the secondary field, whatever the object may be. It is shown [13] that for a single spheroid the coefficients $B_k^{(j)}$ are the characteristics of the object, independent of its location and orientation and of the properties of the source. In

109
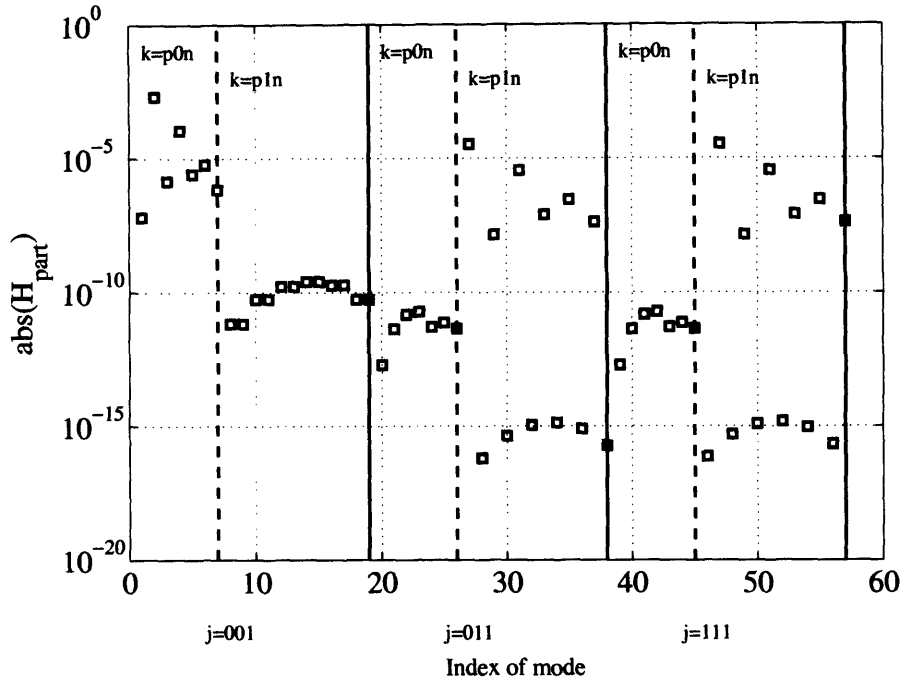
Figure 5-10: Magnitude of H_z in the prolate coordinate system for the oblate spheroidal body

fact, the same conclusion is applied to an object with an arbitrary shape.

For example, consider a composite object (see Fig. 5-13) consisting of two spheroids. Here we assume the following parameters: the first spheroid, $2a = 0.198$ m, $2b = 0.282$ m, $\mu_r = 1$, $\sigma = 1 \times 10^7$ S/m; the second spheroid: $2a = 0.312$ m, $2b = 0.589$ m, $\mu_r = 100$, $\sigma = 1 \times 10^7$ S/m. For combinations of magnetic and non-magnetic metallic pieces, the scattered field obtained by assuming a simple superposition of MQS responses from two such objects will be insignificantly different from the actual scattered field, if the observation point is farther away than their characteristic dimensions [18, 19]. Similarly, if the objects are both magnetic but their separation is at least on the order of the smallest characteristic dimension, the effects of the interaction on the scattered far field is weak [18, 19]. In this example we only consider such cases, i.e., the scattered field from the two objects can be obtained by superposing the responses of each object, accounting for their different locations within the primary field. The purpose is simply to assemble an example of a heterogeneous structure for which the response can readily be calculated, in order to

110
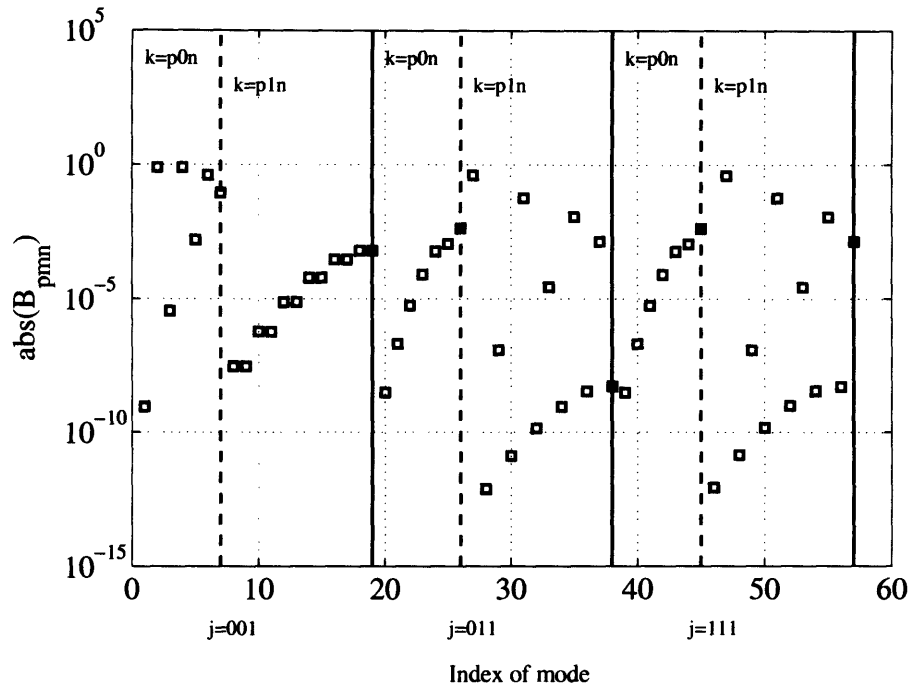
Figure 5-11: Magnitude of $B_k^{(j)}$ in the oblate coordinate system
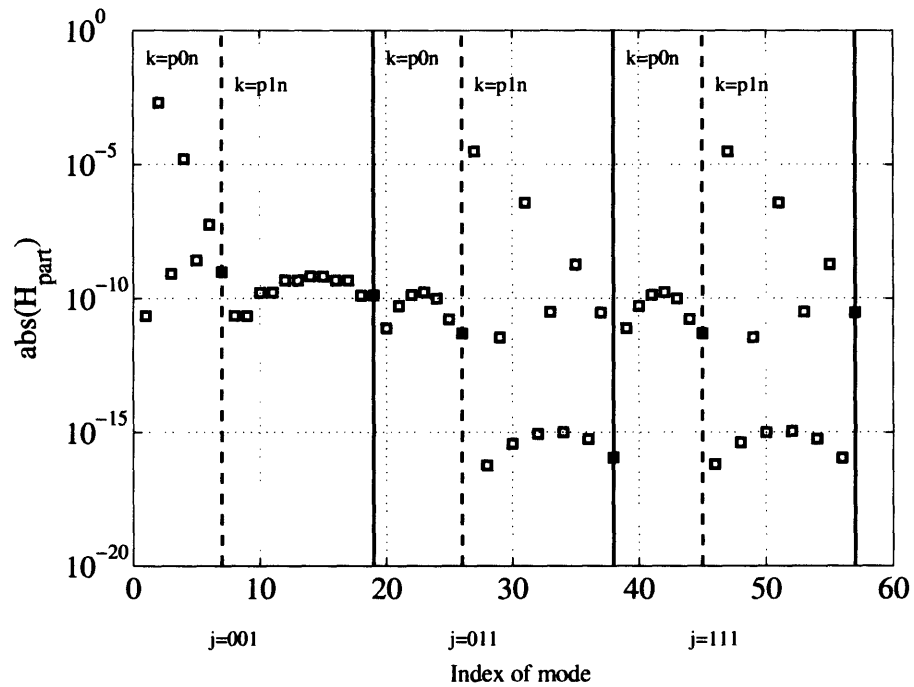
Figure 5-12: Magnitude of H_z in the oblate coordinate system
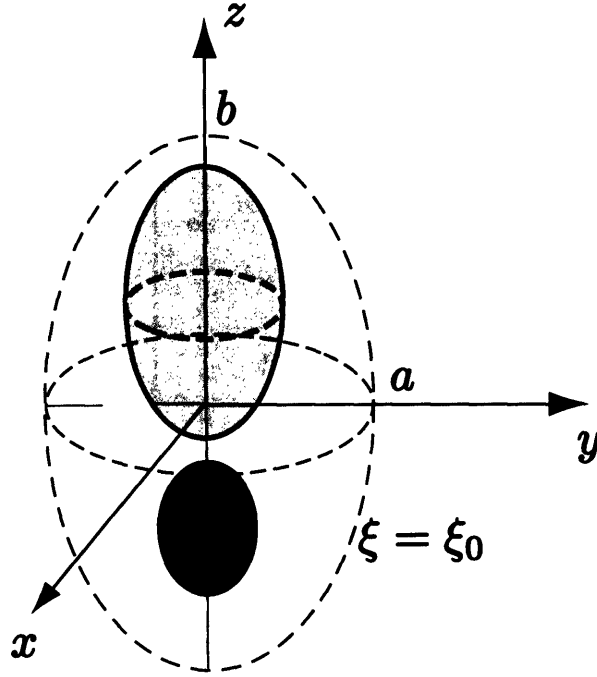
Figure 5-13: Composite object composed of two spheroids. We expand the fields in a spheroidal coordinate system with the surface of the spheroid $\xi = \xi_0$ enclosing the composite object. The interfocal distance d is 1.6 m in the simulation.

Table 5.4: Inverted $B_k^{(j)}$ for the composite object shown in Fig. 5-13. The number inside the parenthesis means the power of 10.

	$k = (0,0,1)$		$k = (0,1,1)$	
	Inversion A	Inversion B	Inversion A	Inversion B
$j = (0,0,1)$	$4.45(-2) - 1.19(-2)$i	$4.45(-2) - 1.19(-2)$i	$9.73(-10) - 4.69(-10)$i	$-7.90(-9) + 3.27(-9)$i
$j = (0,1,1)$	$1.14(-10) - 4.55(-11)$i	$-1.40(-10) + 7.69(-11)$i	$-2.74(-2) + 6.52(-3)$i	$-2.74(-2) + 6.52(-3)$i
$j = (1,1,1)$	$1.91(-11) - 7.43(-12)$i	$-3.14(-18) + 1.03(-18)$i	$-1.15(-10) + 4.66(-11)$i	$-2.58(-17) - 6.75(-18)$i

illustrate the invariance of the $B_k^{(j)}$ in a given spheroidal coordinate system.

We solve for $B_k^{(j)}$ by matching measurements on and above the "ground" (i.e. some chosen plane near the object). We obtain $B_k^{(j)}$ by solving the truncated version of Eq. (5.4) in which the maximum primary mode index j and the maximum secondary mode index k are chosen to be J and K, respectively. In this numerical simulation, we choose J to be $m = 3, n = 5$, and K to be $m = 2, n = 5$. Note the secondary field $\overline{H}^S(\bar{r})$ here is expressed in the self coordinate system. An overdetermined problem is setup for N measurements when the number of equations $3N$ is greater than the total number of unknowns JK.

To show that the coefficients $B_k^{(j)}$ are independent of the orientation of the object, we solve for them in the following two situations: case A: $(\theta_0, \phi_0) = (\frac{\pi}{3}, 0)$; case B: $(\theta_0, \phi_0) = (\frac{\pi}{4}, \frac{\pi}{4})$. Some of the typical resulting $B_k^{(j)}$ at 463 Hz are shown in Table 5.4. The values illustrate that the coefficients $B_k^{(j)}$ are independent of the orientation of the object so that $B_k^{(j)}$ is indeed a characteristic of the object. Note that the small terms are close to zero, and we do not expect them to be exact due to numerical errors. Also, note that we may not always be able to determine all the $B_k^{(j)}$ that we desire when some input modes or scattering modes are too weakly represented in the particular data at hand.

5.6   Inversion from noisy synthetic data

In order to obtain the characteristic scattering coefficients $B_k^{(j)}$, we solve a linear equation system, i.e., a truncated version of Eq. (5.4), with the maximum primary mode J and secondary mode K. For ease of presentation, we rewrite the linear equation system to be

$$Ax = h \tag{5.7}$$

where x is a JK-dimensional vector representing the unknowns $B_k^{(j)}$, h is a N-dimensional vector representing the measured magnetic fields, A is a N by JK matrix, and N denotes the total number of measurements. An overdetermined problem is set up when the number of equations N is greater than the total number of unknowns JK,

$$\text{Minimize} : \ ||Ax - h||^2, \tag{5.8}$$

and its solution is well-known:

$$x = (A^T A)^{-1} A^T h. \tag{5.9}$$

It is well known that the solution is very sensitive to small errors on h when the matrix A is ill-conditioned, or nearly singular. Ill-conditioning is a common issue in inverse problems. In the inversion of the scattering coefficient $B_k^{(j)}$, we deal with this issue using

113

two approaches. One is to choose few but important modes for both primary and secondary potentials so that the total number of unknowns is reduced. The other is to apply regularization techniques, in which the objective function is modified so that a balance between accuracy and stability is achieved.

5.6.1 Mode selection

One of the reasons for ill-conditioning is that the number of unknowns is too large. Since the number of unknowns (JK) is equal to the product of the numbers of the primary and the secondary modes, we seek to use as few as possible of both the primary and the secondary modes, while those modes should be important in representing the properties of the primary and the secondary fields. Another effect of the reduction of the modes is to speed up the inversion.

In the following numerical example, we show how the primary and the secondary modes are chosen in order to reduce the ill-conditioning of the inverse problem.

A prolate spheroid with $2a = 0.066$ (m), $2b = 0.245$ (m), relative permeability $\mu_r = 50$, and conductivity $\sigma = 10^7$ (S/m) is considered in this example. We choose the interfocal distance of the spheroidal coordinate system to be same as that of the spheroid $d = 2\sqrt{b^2 - a^2} = 0.23594$ (m). The spheroid object is put on a horizontal grid whose height is $z = 0$. During the measurement, the object is moving while the GEM-3 sensor is stationary. The GEM-3 sensor is positioned directly beneath the center of the grid. The object is first moved along the y axis, where 13 measurements are performed, $y = -0.6 + (i - 1) \times 0.1$(m), $i = 1, \ldots, 13$. Then the object is moved along the x axis, and 12 measurements are performed, $x = -0.6 + (i - 1) \times 0.1$(m), $i = 1, \ldots, 6, 8, \ldots, 13$. Two levels of measurements are carried out, where the the GEM-3 is located at $z = -0.165$ (m) and $z = -0.265$ (m), respectively. We will retrieve the scattering coefficients $B_k^{(j)}$ from the measurements for some orientations of the object, and then predict the secondary fields for other orientations of the object. In the retrieval stage, the object is orientated at $(\theta = 3\pi/4, \phi = \pi)$ and $(\theta = 0, \phi = 0)$, respectively, with the GEM-3 at the level $z = -0.165$ (m). In the prediction stage, the orientation of the object is $(\theta = \pi, \phi = 0)$,

with the GEM-3 at the level $z = -0.165$ (m) and $z = -0.265$ (m). All the three components of magnetic fields are considered, and the operation frequency is 10,950 Hz.

Note that although the object is a spheroid, we do not use that as prior information in the inversion of the scattering coefficients $B_k^{(j)}$.

Selection of the primary modes

The GEM-3 sensor produces non-uniform fields, whose potentials can theoretically be expressed as an infinite linear combination of orthogonal primary modes. However, only a small number of modes are dominant, with others negligible. According to the author's experience, four to seven modes are usually sufficient to describe the potentials produced by the GEM-3 sensor.

In Fig. 5-14, the magnitudes of the primary modes are compared. In this example, the coefficients $b_j(\bar{r}_i)$ are calculated for each relative position $(\bar{r}_i)$ between the object and the sensor. The maximum magnitude of each primary mode, i.e. the maximum $|b_j(\bar{r}_i)|$ for all $\bar{r}_i$, is plotted in Fig. 5-14, where we choose $m \leq 7$ and $n \leq 7$ so that we have a finite number of j. Note that the magnitudes of the coefficients b_j in Fig. 5-14 are normalized so that the maximum one is unity. The index of the mode j is given in section 5.2.5. We observe that there are only four dominant modes: $j = (0, 0, 1)$, $(0, 0, 2)$, $(0, 1, 1)$, and $(1, 1, 1)$. Note that modes $(0, 0, 3)$, $(0, 1, 2)$, and $(1, 1, 2)$ are next to the aforementioned four modes, but they are small compared with the four basic modes. We also find that all other modes are negligible.

Selection of the secondary modes

Unlike the primary fields, whose modes are independent of the scattering object as long as the local spheroidal coordinate system is uniquely defined, the secondary fields strongly depend on the properties of the scattering object. For an object, which can be any shape, any composition, we cannot determine a priori which specific secondary mode is dominant or negligible. Thus, we have to truncate the secondary modes by keeping only the lower modes. We refer to this approach as a "standard model." In practice, however, since the response of most of UXO to a GEM-3 sensor can be effectively modeled as that of a body of
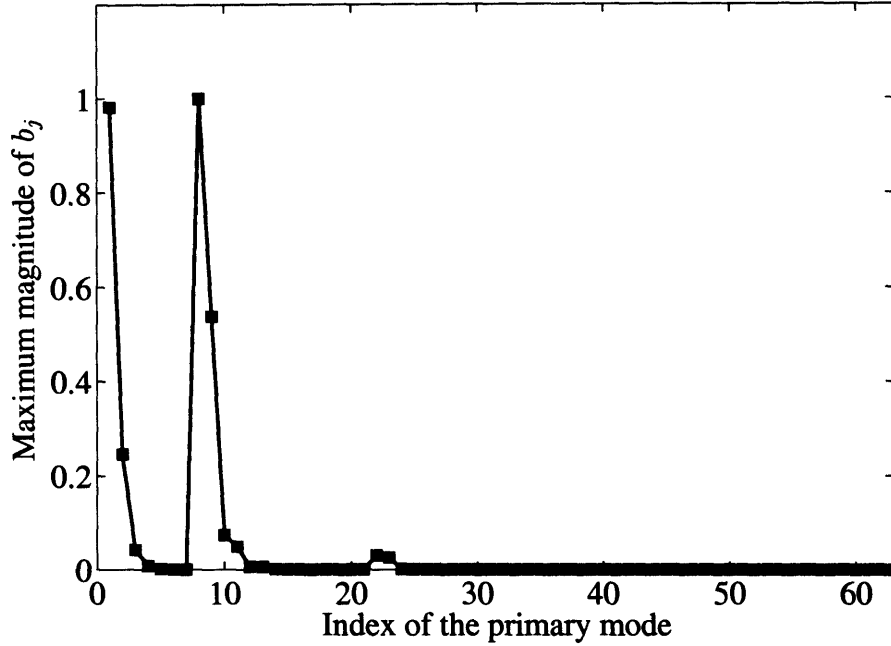
Figure 5-14: Maximum magnitude of b_j

revolution, the number of secondary modes is dramatically reduced due to the properties of the modes for a BOR that are presented in section 5.2.4. We refer to this model as a "BOR model". For example, in the case that only the secondary modes with $m \leq 2$ and $n \leq 2$ are considered, for the four fundamental primary modes, there are only eight unknown scattering coefficients in the BOR model, while there are 36 in the standard model. In the BOR model, the eight $B_k^{(j)}$s to be solved for are $B_{0,0,0}^{(0,0,1)}$, $B_{0,0,1}^{(0,0,1)}$, $B_{0,0,2}^{(0,0,1)}$, $B_{0,0,0}^{(0,0,2)}$ $B_{0,0,1}^{(0,0,2)}$, $B_{0,0,2}^{(0,0,2)}$, $B_{0,1,1}^{(0,1,1)}$ and $B_{0,1,2}^{(0,1,1)}$. All other 28 modes are either equivalent to one of the eight modes ($B_{1,1,1}^{(1,1,1)} = B_{0,1,1}^{(0,1,1)}$ and $B_{1,1,2}^{(1,1,1)} = B_{0,1,2}^{(0,1,1)}$) or equal to zero.

We test the stability of the system with different selections of primary and secondary modes in the presence of the noise, and the results are shown in Table 5.5.

To quantitatively evaluate the prediction, we define the relative error as follows:

$$E_R = \frac{\|h_t - h_p\|}{\|h_t\|}, \tag{5.10}$$

where h_t and h_p denote the true and the predicted magnetic fields at all measurement points

116

Table 5.5: Relative error of the prediction in the presence of noise. We interpret (4j, m1n1, 10%) as follows: four fundamental primary modes, secondary modes with $m \leq 1$ and $n \leq 1$, and 10% Gaussian noise added to the true magnetic fields. Other cases are interpreted similarly.

	Standard model	BOR model
(4j, m1n1, 10%)	0.15232	0.11409
(4j, m1n1, 20%)	0.25597	0.22049
(4j, m2n2, 10%)	0.41432	0.11937
(7j, m1n1, 10%)	0.27384	0.051730
(7j, m1n1, 20%)	0.53769	0.096471
(7j, m2n2, 10%)	1.9365	0.091543
(7j, m2n2, 10%, Regularization)	0.23230	0.090055

at the predict stage, respectively, and $|| \cdot ||$ represents the 2-norm Euclidean length. The smaller the relative error, the better the prediction.

Gaussian noise is added to the true magnetic fields at the retrieval stage, with magnitudes of 10% and 20% of the true field strength. The performances of both the standard model and the BOR model are evaluated.

In Table 5.5, we interpret (4j, m1n1, 10%) as follows: four fundamental primary modes, secondary modes with $m \leq 1$ and $n \leq 1$, and 10% Gaussian noise added to the true magnetic fields. Other cases are interpreted similarly. Table 5.5 shows that the BOR model works better than the standard model for a spheroidal object in the presence of noise. For the secondary modes, the selection of $m \leq 1$ and $n \leq 1$ is better than that of $m \leq 2$ and $n \leq 2$, other parameters being equal. For the primary modes, although the seven-mode case is slightly better than the four-mode case in the BOR model, this is not true when the positions of the measurements also contain noise. Table 5.6 shows the comparison of the results between the four-primary-mode and the seven-primary-mode in the presence of the noise in the positions of the measurements, where we add Gaussian noise to the x and y coordinates, with magnitude of 5 (mm). The results in Table 5.6 show that the four-primary-mode formulation performs better than the seven-primary-mode one. It is encouraging that good prediction can be obtained using only four fundamental primary modes and few secondary modes with $m \leq 1$ and $n \leq 1$.

Table 5.6: Relative error of the prediction in the presence of noise in both the magnetic fields and the positions of measurements.

	Standard model	BOR model
(4j, m2n2, 10%)	0.38698	0.12597
(7j, m2n2, 10%)	1.9094	0.13353

The comparison of the predicted and the true magnetic fields are compared in Fig. 5-15-Fig. 5-17. Note that only some typical results in Table 5.5 are plotted.

5.6.2 Regularization

For the overdetermined problem Eq. (5.8), its solution Eq. (5.9) is very sensitive to small errors in h if the matrix A is ill-conditioned. In this case, we say that the operator $(A^T A)^{-1} A^T$ is unstable. Besides the mode truncation as described in section 5.6.1, regularization techniques are another common approach to deal with the ill-conditioning problem. The idea of regularization is to approximate the unstable operator by a stable one. There are many regularization techniques with various degrees of sophistication, ease of implementation, and computational efficiency. Here we adopt a Tikhonov regularization technique that is most popularly used [72, 73, 74, 75, 76]. In Tikhonov regularization, the approximate operator is obtained by adding a stabilizing term to the variational formulation Eq. (5.8), which leads to the well known formulation:

$$\text{Minimize}: \ ||Ax - h||^2 + \alpha||x||^2, \tag{5.11}$$

where α is the regularization parameter. We can see from Eq. (5.11) that for the small values of α, the approximation is good but the approximate operator is only marginally stable. On the other hand, for the large values of α, the approximate operator is stable but the approximation is farther from the exact one. Therefore, there is a compromise between the accuracy of the solution and the stability. The solution x for the least square problem with Tikhonov regularization (Eq. (5.11)) is

$$x = (A^T A + \alpha)^{-1} A^T h. \tag{5.12}$$

118
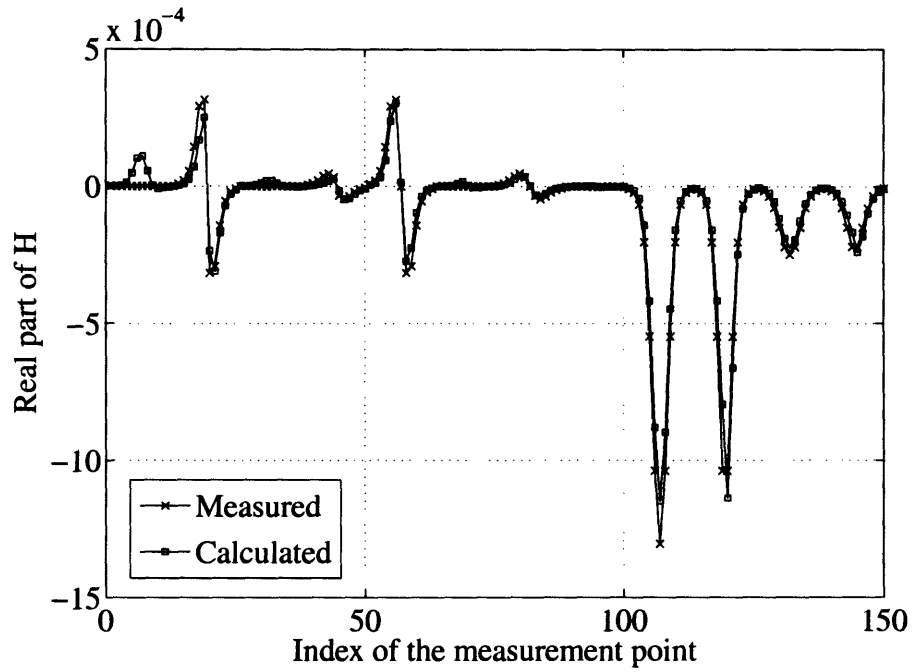
(a) Real part
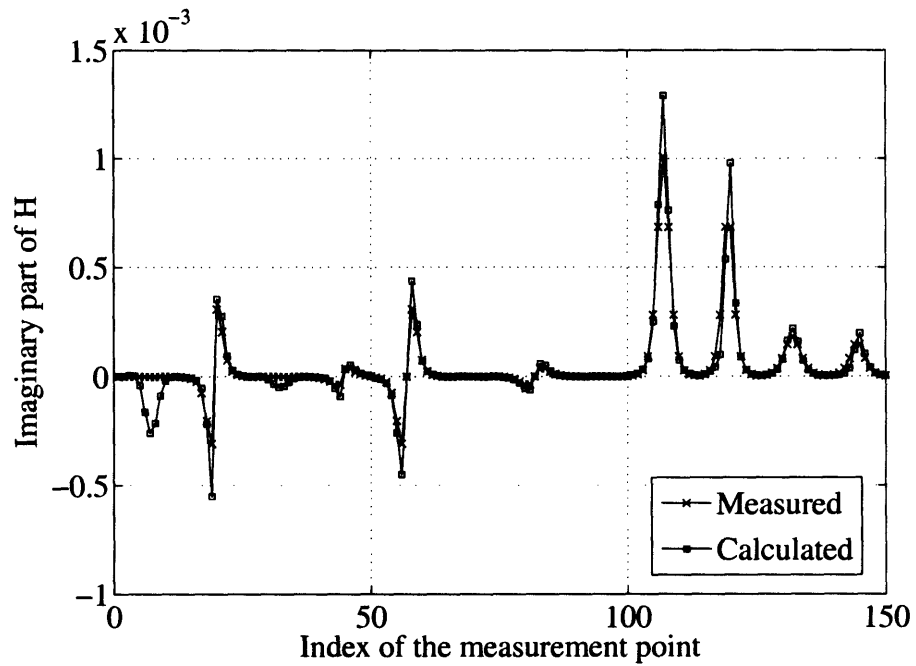
(b) Imaginary part

Figure 5-15: Comparison of the true and the predicted secondary magnetic fields in the presence of 20 % noise, where the standard model is used and the primary modes are chosen to be the four fundamental modes and the secondary modes are chosen to be $m \leq 1$ and $n \leq 1$.

119
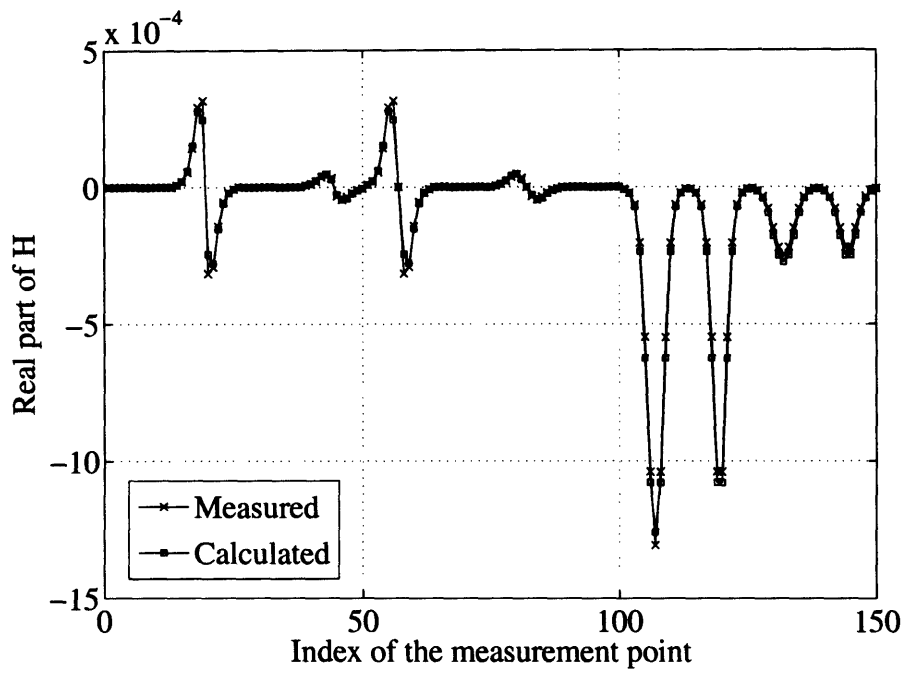
(a) Real part
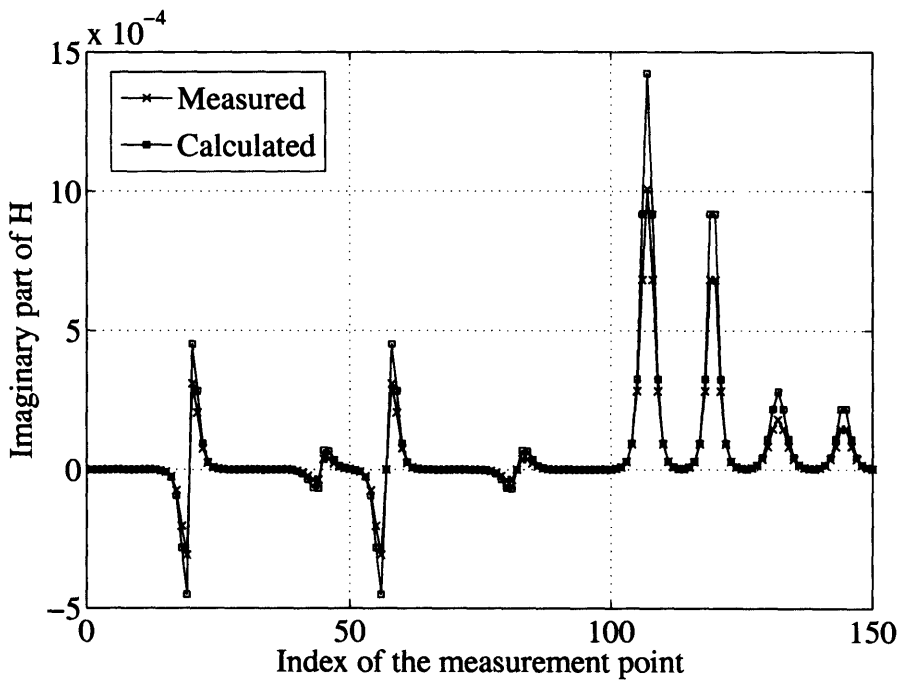
(b) Imaginary part

Figure 5-16: Comparison of the true and the predicted secondary magnetic fields in the presence of 20 % noise, where the BOR model is used and the primary modes are chosen to be the four fundamental modes and the secondary modes are chosen to be $m \leq 1$ and $n \leq 1$.

120
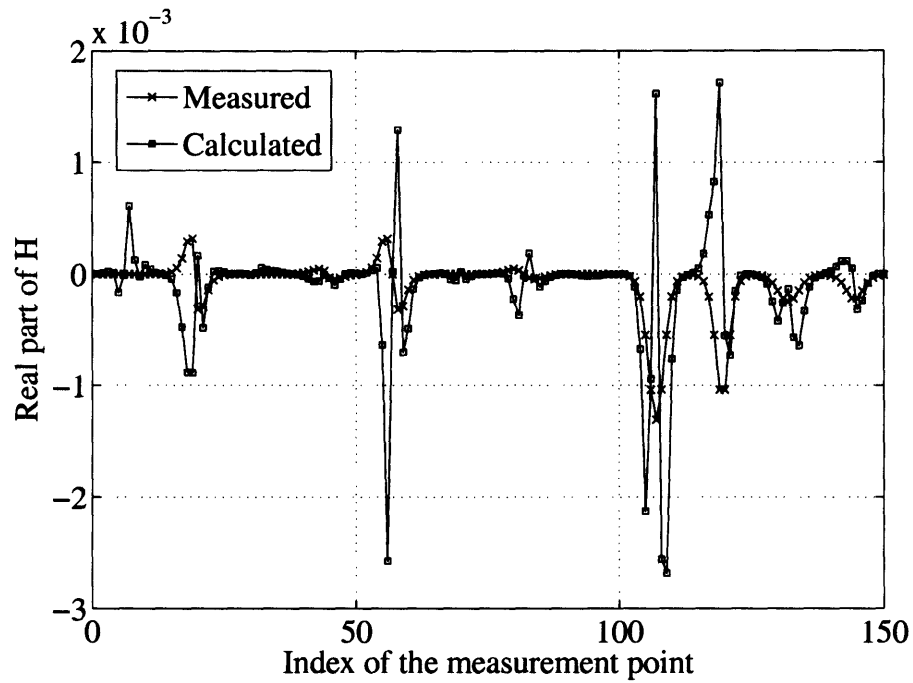
(a) Real part
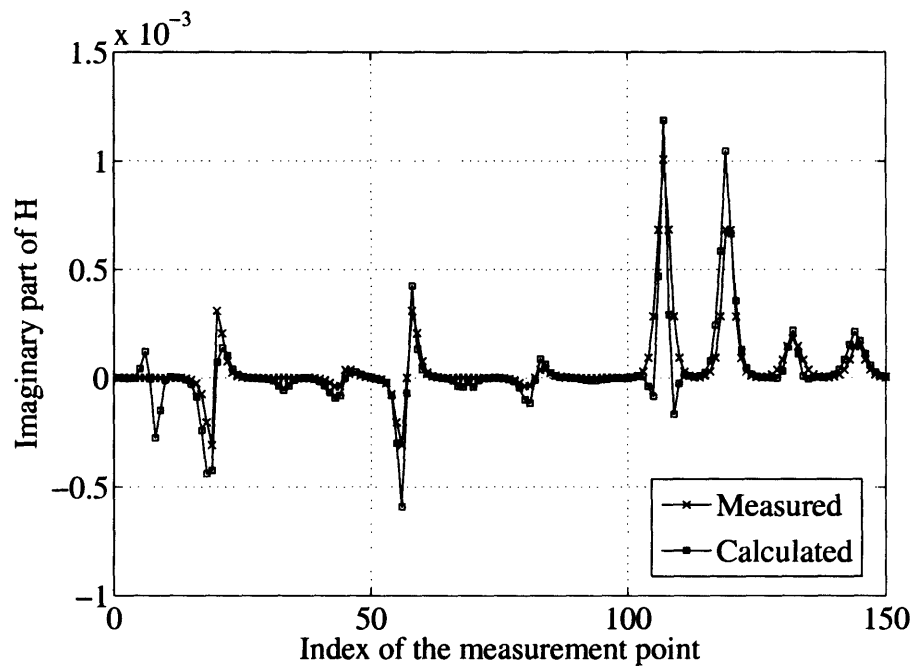
(b) Imaginary part

Figure 5-17: Comparison of the true and the predicted secondary magnetic fields in the presence of 10 % noise, where the standard model is used and the primary modes are chosen to be the seven fundamental modes and the secondary modes are chosen to be $m \leq 2$ and $n \leq 2$.

Choosing the regularization parameter α is difficult and most methods in the literature are typically based on heuristics [74]. Here we do not aim at finding a systematic way of choosing the regularization parameter, which in fact is a task for mathematicians. Instead, we show, by empirically choosing the regularization parameter, that Tikhonov regularization can help to improve performance in the inversion of the scattering coefficients $B_k^{(j)}$. In this example, we apply Tikhonov regularization to the case (7j, m2n2, 10%) in Table 5.5. Several values of regularization α between 10^{-9} and 10^{-3} are tested, and all of them turn out to help the prediction. The best among all the trials happens when $\alpha = 10^{-5}$. The relative error of the prediction is listed in Table 5.5, where we observe that the accuracy of the prediction of the standard model is improved noticeably and that of the BOR model is slightly improved. The comparison of the magnetic fields between the predicted results and the true results are shown in Fig. 5-18, where we see that the predicted results are much better than those obtained without regularization (see Fig. 5-17).

5.7 Inversion from measurement data

5.7.1 BOR object

In this section, we retrieve the characteristic scattering coefficients of real UXO, most of which can be effectively modeled as bodies of revolution [15]. To show the validity of the spheroidal model approach, we apply it to retrieve the scattering coefficients of a real UXO, namely U2, as shown in Fig. 5-19. We see that its head and body are bodies of revolution, and its eight fins are evenly distributed around the central axis. The longest and the widest dimensions of U2 are 0.245 (m) and 0.062 (m), respectively.

During the measurement, the object U2 is moving while the GEM-3 sensor is stationary. The object U2 is put on a horizontal grid with altitude $z = 0$. The GEM-3 sensor is positioned directly beneath the center of the grid. The object is first moved along the y axis, where 13 measurements are performed, $y = -0.6 + (i - 1) \times 0.1$, $i = 1, \ldots, 13$. Then the object is moved along the x axis, and 12 measurements are performed, $x = -0.6 + (i - 1) \times 0.1$, $i = 1, \ldots, 6, 8, \ldots, 13$. Two levels of measurements are carried
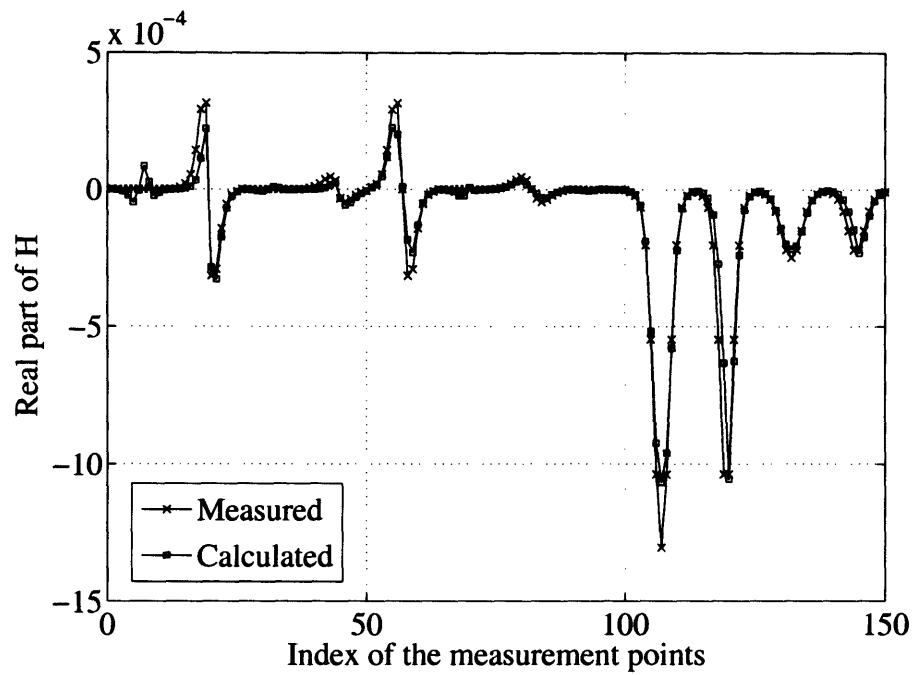
(a)
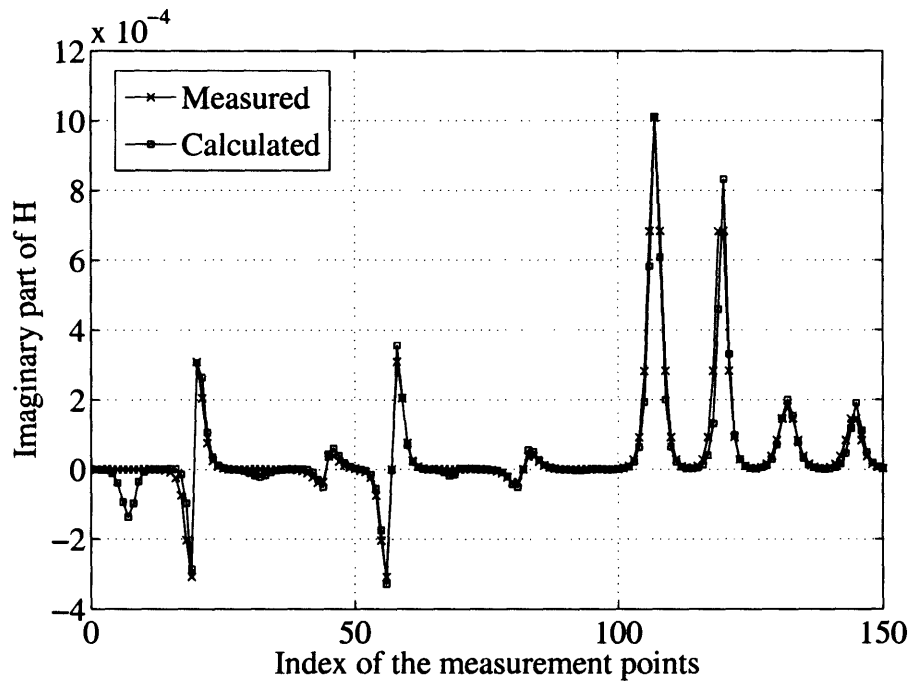
(b)

Figure 5-18: Comparison of the true and the predicted magnetic fields in the presence of 10 % noise, The standard model with the Tikhonov regularization is used and the primary modes are chosen to be the seven fundamental modes and the secondary modes are chosen to be $m \leq 2$ and $n \leq 2$.

out, where the GEM-3 is located at $z = -0.165$ (m) and $z = -0.265$ (m), respectively.

In the retrieval stage, the object are orientated in two ways: nose upward ($\theta = 0$, $\phi = 0$) and nose downward ($\theta = \pi$, $\phi = 0$). The GEM-3 sensor measures at two levels for each position of the object U2: $z = -0.165$ (m) and $z = -0.265$ (m). In the prediction stage, the object U2 is tilted $3\pi/4$, with the nose downward, pointing to the positive x direction, i.e. ($\theta = 3\pi/4$, $\phi = \pi$). The altitude of the GEM-3 sensor is same as that in the retrieval stage. Only z component of the fields are measured and the operation frequency is 10,950 Hz.

We choose the interfocal distance of the spheroidal coordinate system to be $= 0.236$ (m), which is same as that in section 5.6.1. Since the object U2 is almost a BOR, we use a BOR model in our retrieval. We choose the four basic primary modes modes, and $m \leq 1$ and $n \leq 1$ for the secondary modes. Tikhonov regularization with the regularization parameter $\alpha = 10^{-5}$ is used to deal with the ill-condition. The retrieved scattering coefficients $B_k^{(j)}$ are then used to predict the magnetic fields in the prediction stage. For all the 50 prediction data, the relative error is $E_r = 0.16050$, and the comparison of the predicted and the true values are shown in Fig. 5-20. We see that the predicted results generally agree with the measured true data. Again, as illustrated in retrieval on the synthetic data in section 5.6.1, it is encouraging to see that the scattering effect of the real BOR object can be effectively modeled using only four basic primary modes and the few lowest secondary modes.

5.7.2 Non-BOR object

In this section, we apply the spheroidal mode approach to some non-BOR objects. Some measurement data are first used to retrieve the scattering coefficients $B_k^{(j)}$, and then we predict the magnetic fields at other measurement positions.

First we consider a rectangular metallic plate, as shown in Fig. 5-21. For convenience, we refer to this object as CL15 (The picture and the name of the object are provided by Dr. Kevin O'Neill), whose dimension is 0.32 (m) $\times$ 0.14 (m) $\times$ 0.025(m). As shown in Fig. 5-21, we label the middle point of one of the edges with the length of 0.14 (m) as

all measurements in mm

60
42 49   outside diameters   60 62
25
16

37 — 28 — 126 — 54
245
lengths
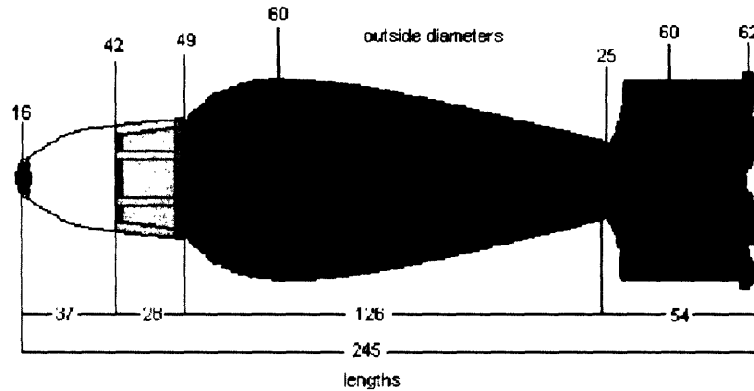
Figure 5-19: A UXO object labeled as U2 (Courtesy of Dr. K. O'Neill)

"nose", and the two edges with the length of 0.32 (m) as "left side" and "right side". The local coordinate system attached to the object is defined as follows: we assign the x axis to be the direction from the center to the right side of the object; y axis to be the direction from the center of the object to the nose; z axis to be the normal direction of the plate.

In the retrieval stage, two orientations of the object are considered. The object CL15 is first positioned with the nose upward and the normal of the plate paralleling with the x axis of the lab frame. In terms of the Euler angles, this orientation is ($\phi = 0$, $\theta = \frac{\pi}{2}$, $\gamma = \frac{\pi}{2}$). Then the object is positioned with the nose pointing to the y axis of the lab frame with the normal of the plate paralleling with the x axis of the lab frame. This orientation is ($\phi = 0$, $\theta = \frac{3\pi}{2}$, $\gamma = 0$). For both orientations, the object is placed onto a surface with the altitude $z = 0$. During the measurement, the object is stationary while the GEM-3 sensor is moving. The GEM-3 sensor performs measurements on a 7 by 7 grid ($x = -0.3 + (i - 1) \times 0.1$, $y = -0.3 + (j - 1) \times 0.1$, i, $j = 1, \ldots, 7$) above the object CL15. The altitudes of the measurements are $z = 0.532$ (m) and $z = 0.365$ (m) for the two orientations, respectively.

In the prediction stage, two levels of 7 by 7 grid of measurements are performed at $z = 0.582$ (m) and $z = 0.632$ (m) for the first orientation, and the two levels ($z = 0.415$ (m) and $z = 0.465$ (m)) of measurements are carried out for the second orientation. These

125
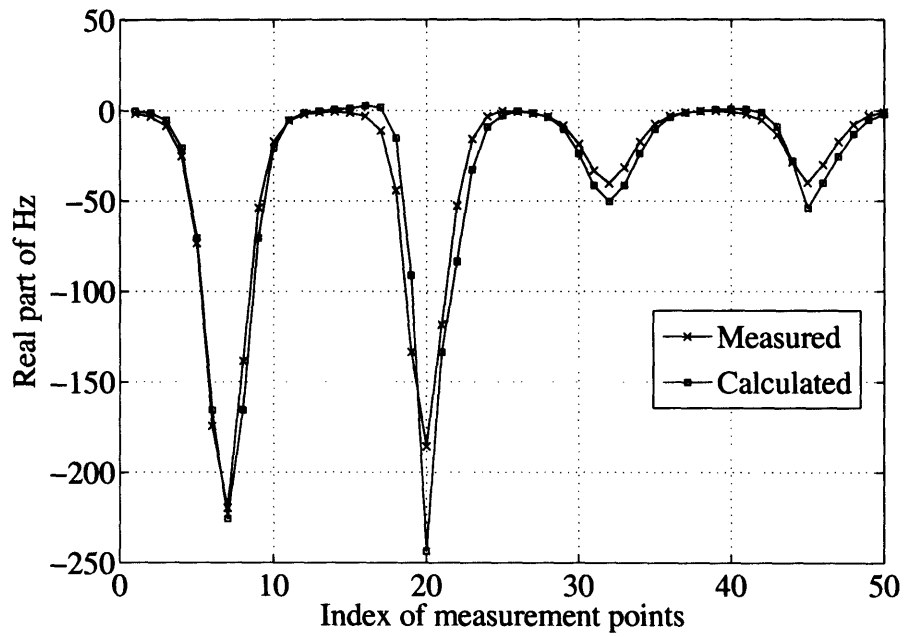
(a) Real parts
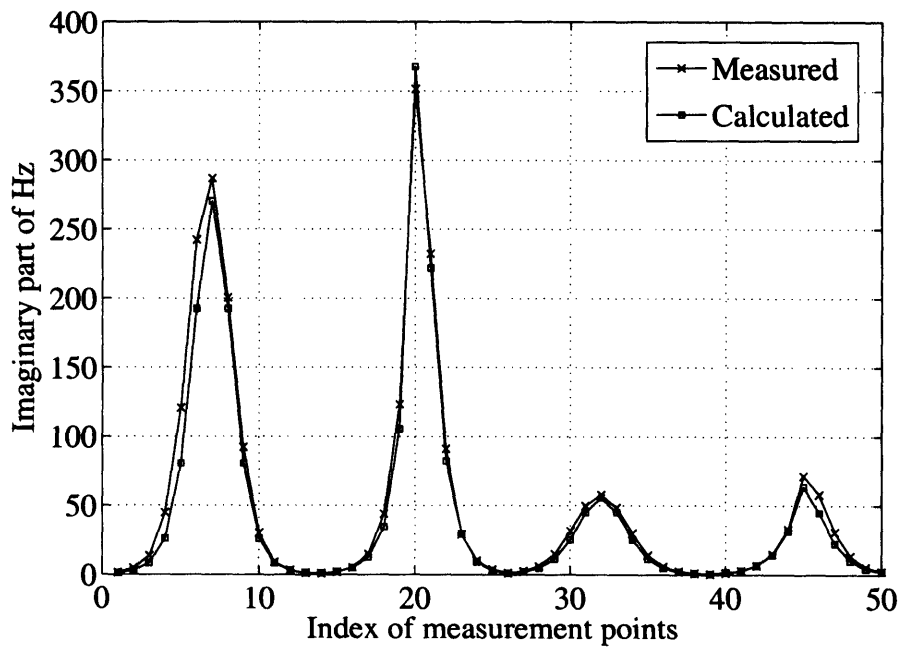
(b) Imaginary parts

Figure 5-20: Comparison of the measured and the predicted magnetic fields for the object U2

Figure 5-21: A metallic rectangular object labeled as CL15 (Courtesy of Dr. K. O'Neill)

data are used as the true value to compare with the predicted results.

Note that in both retrieval and prediction stages, only the z component of the magnetic fields are measured, and the operation frequency is 210 Hz. In the coordinate system attached to the object, we define a spheroidal coordinate system with the foci in the z axis of the local system and the interfocal distance $d = 0.236$ (m).

With the normal direction of the plate being the z axis in the local coordinate system, the object CL15 is not a body of revolution. First we use the standard model to retrieve the scattering coefficients. In the retrieval, we choose the four fundamental primary modes modes, and $m \leq 1$ and $n \leq 1$ for the secondary modes. Tikhonov regularization with the regularization parameter $\alpha = 10^{-7}$ is used to deal with the ill-condition. For all the 196 prediction data, the relative error is $E_r = 0.17598$, and the comparison of the predicted and the true values are shown in Fig. 5-22.

Since the object CL15 is far from a BOR, if we apply a BOR model to it, we expect to have a bad prediction of the magnetic fields. The prediction results from a BOR model with the same parameters as in the standard model are shown in Fig. 5-23, where noticeable mismatch between the predicted and the true values is observed. The relative error is $E_r = 0.33229$, much larger than that of the standard model.

In the second example, we consider a square plate with dimension 0.14 (m) × 0.14 (m) × 0.01(m), as shown in Fig. 5-24. We refer to this object as CL16 (The picture and the name of the object are provided by Dr. Kevin O'Neill). The method of labeling the "nose", "left side", and "right side" are similar to that for the object CL15 (see Fig. 5-24). The definition of the local coordinate system is also same as that for the object CL15.

Only one orientation is considered in both the retrieval and the prediction stages: ($\phi = 0$, $\theta = \frac{\pi}{2}$, $\gamma = \frac{\pi}{2}$), which is the first orientation of the object CL15. The measurements are carried out on the same grid, except the the altitude is $z = 0.341$ (m) in the retrieval stage and $z = 0.391$ (m) and 0.441 (m) in the prediction stage.

First we use the standard model to retrieve the scattering coefficients, which are then used to predict the magnetic fields. The spheroidal coordinate system, the primary and secondary modes, and the regularization parameters are chosen to be same as those in the retrieval for the object CL15. The comparison of the predicted and the true values are

128
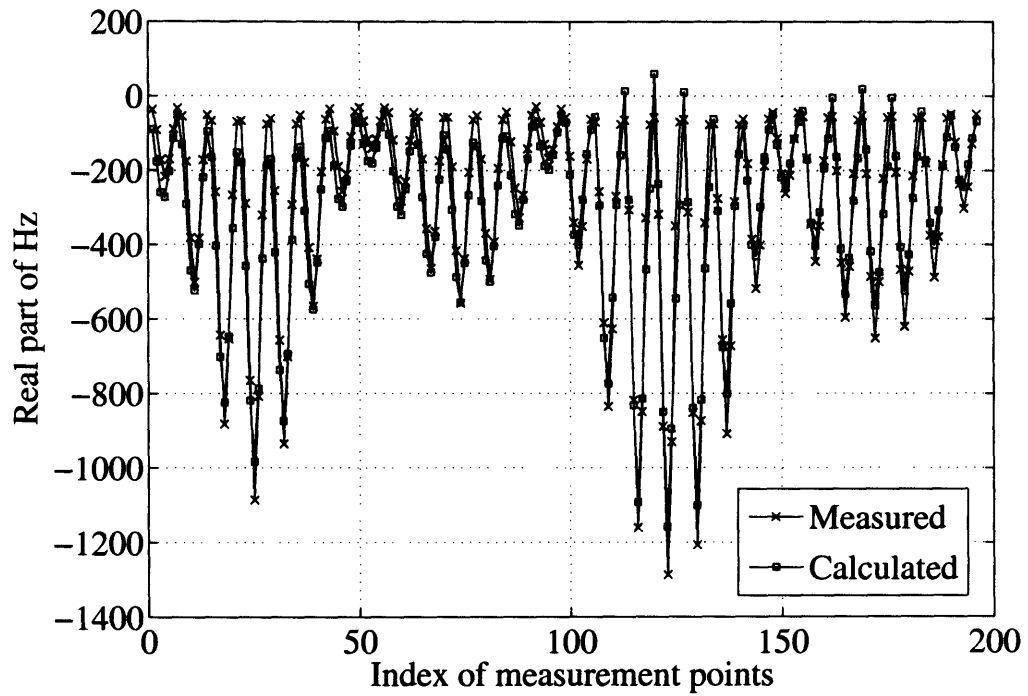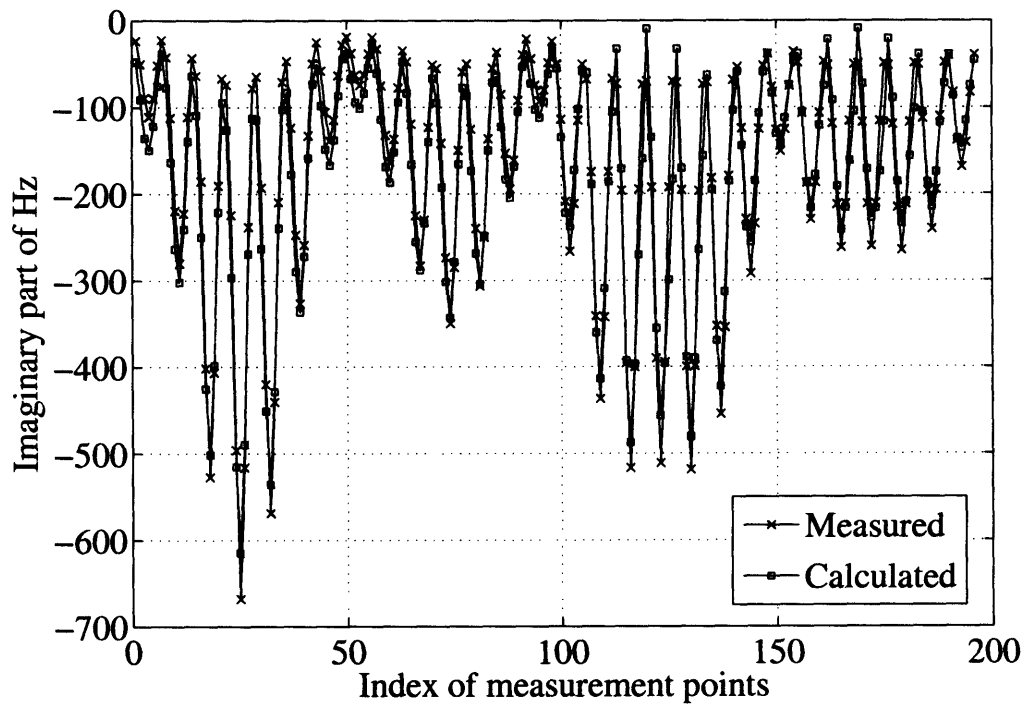
(a) Real parts

(b) Imaginary parts

Figure 5-22: Comparison of the measured and the predicted magnetic fields for the object CL15, where the standard model is used in the retrieval.

129
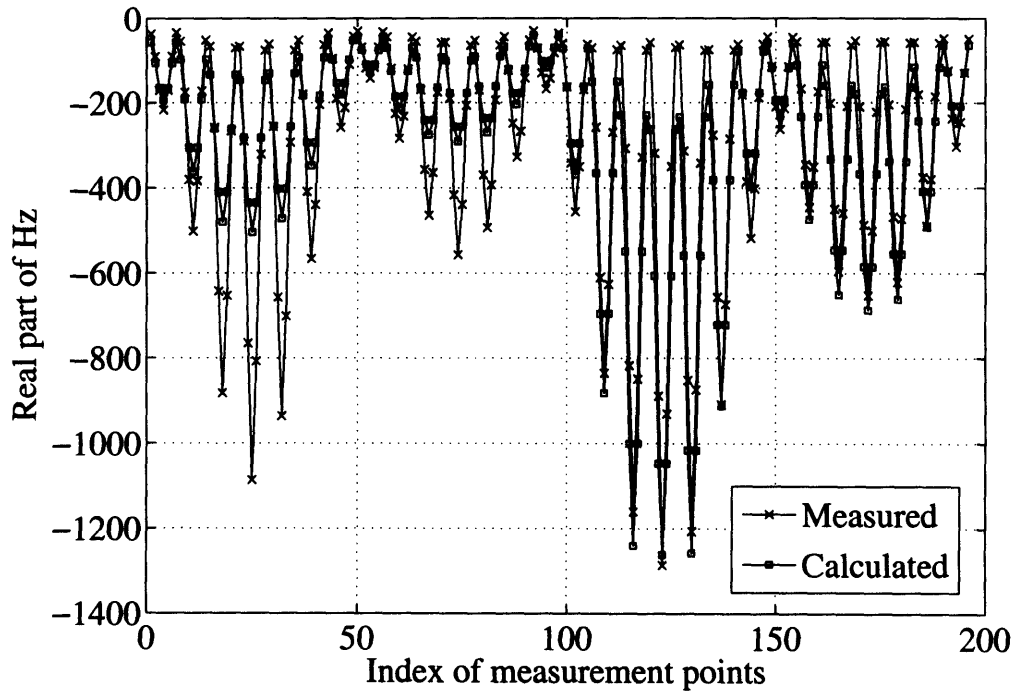
(a) Real parts

(b) Imaginary parts

Figure 5-23: Comparison of the measured and the predicted magnetic fields for the object CL15, where the BOR model is used in the retrieval.

130

Figure 5-24: A square metallic plate labeled as CL16 (Courtesy of Dr. K. O'Neill)

shown in Fig. 5-22, and the relative error is $E_r = 0.054052$.

Although the object CL16 is not a BOR, we expect to effectively model it using a BOR model since it is a square plate. The prediction results from a BOR model with the same parameters as in the standard model are shown in Fig. 5-25, where we see good match between the predicted and the true values. The relative error is $E_r = 0.17989$, much smaller than that of the BOR model for the object CL15.

5.8 Pattern matching and classification

5.8.1 Pattern matching

The spheroidal mode approach can also be implemented in a pattern matching ("finger-printing") calculation for dealing with very complex objects, such as some UXOs. In the following pattern matching example, we identify a UXO among a list of candidates by investigating the patterns of the secondary fields produced by the candidates under a given
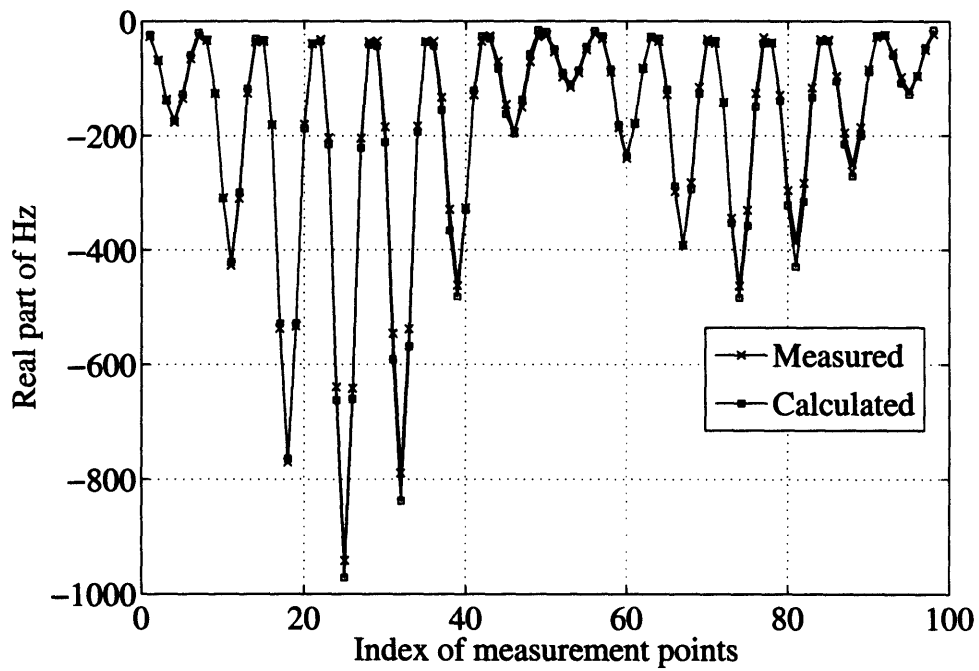
(a) Real parts
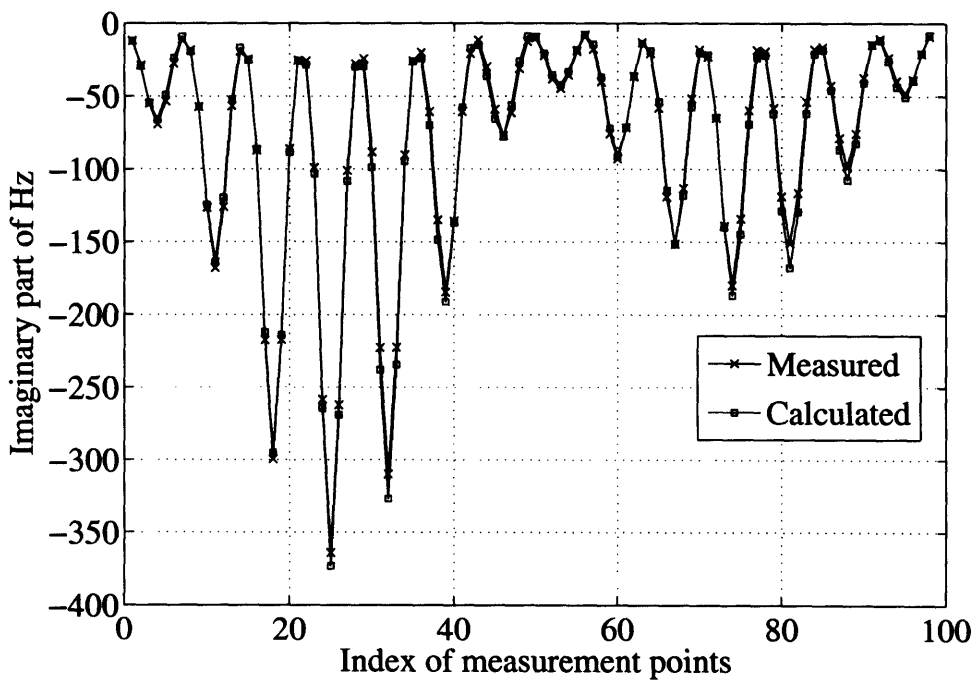
(b) Imaginary parts

Figure 5-25: Comparison of the measured and the predicted magnetic fields for the object CL16, where the standard model is used in the retrieval.
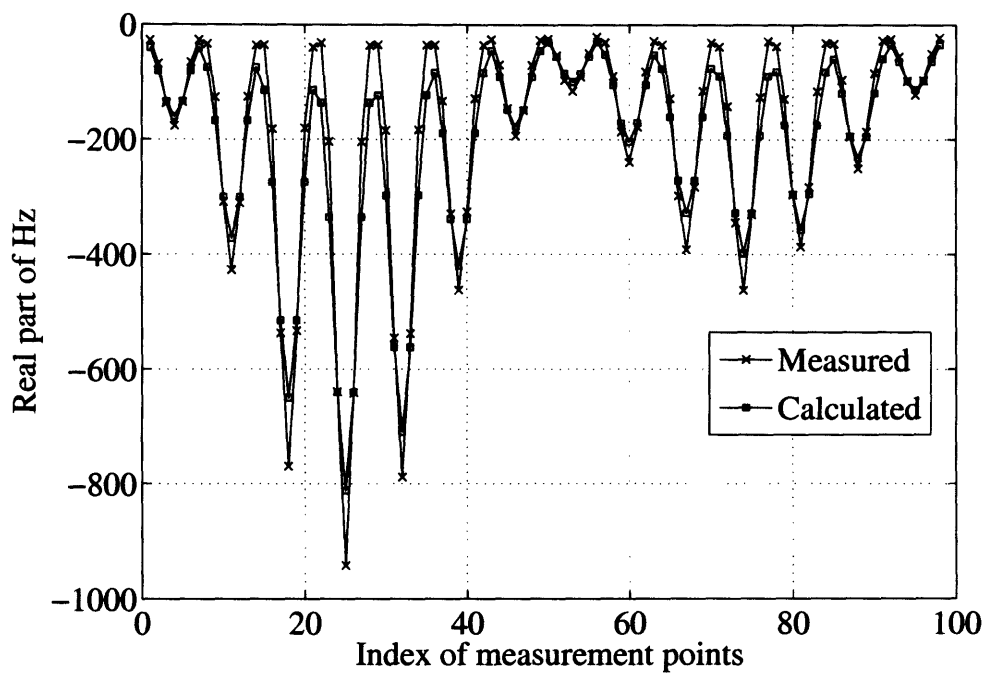
(a) Real parts
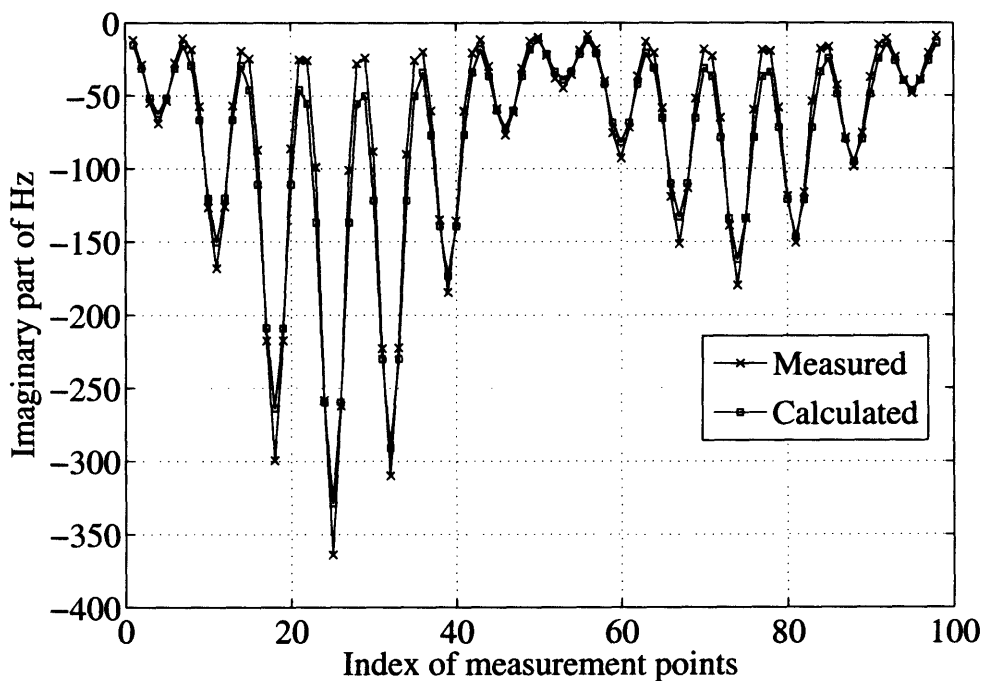
(b) Imaginary parts

Figure 5-26: Comparison of the measured and the predicted magnetic fields for the object CL16, where the BOR model is used in the retrieval.

133

Table 5.7: List of objects that create the candidate patterns

Pattern ID	Object	Material	axis(2a)	axis(2b)	elongation (e)
P1	I1	Iron	91mm	91mm	1
P2	S2	Steel	30mm	182mm	6
P3	S3	Steel	30mm	90mm	3
P4	S4	Steel	15mm	90mm	6
P5	A2	Aluminum	30mm	91mm	3
P6	A3	Aluminum	15mm	91mm	6
P7	C1	composite: I1; S2			
P8	C2	composite: I1; S3			
P9	C3	composite: I1; A2			
P10	U1	UXO: longest dimension: 280mm; widest dimension: 83mm; mainly made of steel			

excitation. When positioned at $\bar{r}_0$ with the rotation angles (θ_0, ϕ_0), each candidate object produces a pattern of secondary fields under a certain excitation. For a certain UXO, we know its characteristic coefficients $B_k^{(j)}$ which are stored in the database. The pattern matching is to determine which unseen candidate object is the above-mentioned UXO. The problem is solved by calculating the pattern of the scattered fields produced by the UXO and comparing the calculated pattern (referred as "test pattern") with the candidate patterns. Since the coefficients $B_k^{(j)}$ are known from the database, only the coefficients b_j need to be calculated in order to obtain the secondary field (see Eq. (5.4)). For a given source, the coefficients b_j are calculated by the method proposed in section 5.4. After sweeping all the candidate patterns of secondary fields, the pattern that produces the minimum mismatch with the test pattern is identified. The discrimination criterion is that when the mismatch is less than a threshold, we conclude that the identified object is the UXO in consideration, otherwise it is not.

In this pattern matching example, we have ten candidate patterns of scattered fields. To create the candidate patterns, we put each of the objects listed in Table 5.7 at $\bar{r}_0 = (0, 0, 0)$ m, with rotation angle $(\theta_0, \phi_0) = (0, 0)$, and the GEM-3 instrument is used to excite the object and record the scattered magnetic fields. Object A2 is shown in Fig. 5-7, while objects I1, A3, S2, S3, and S4 are shown in Fig. 5-27, and U1 is shown in Fig. 5-28. Note that C1, C2 and C3 are composite objects, consisting of a spheroid and a sphere positioned

(a) I1   (b) S2   (c) S3   (d) A3 (left), S4 (right)
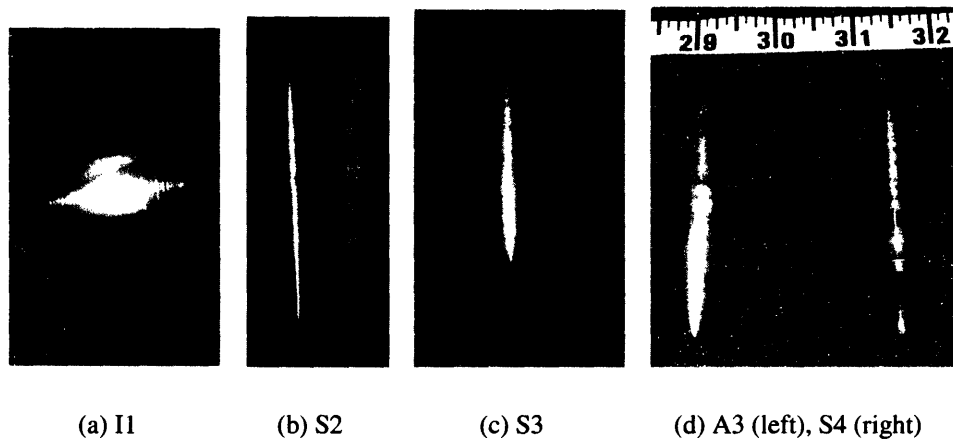
Figure 5-27: Objects in Table 5.7 that create the candidate patterns (Courtesy of Dr. K. O'Neill)

Figure 5-28: An example of UXO with the longest dimension 280mm and widest dimension 83mm, designated U1 (Courtesy of Dr. K. O'Neill)

coaxially as shown in Fig. 5-13. Operating at 510 Hz, the GEM-3 collects data at eight different levels above the object. In this pattern matching test, we assume that we don't know the identity of the objects in Table 5.7. Given the ten candidate patterns and the coefficients $B_k^{(j)}$ for the UXO U1 that is sought (in a spheroidal coordinate system with the interfocal distance $d = 0.2$ m), we are to determine which candidate pattern is most likely to be associated with the UXO U1.

The mismatch between the test pattern and the candidate pattern is defined in Eq. (5.6), which represents the average relative mismatch of the secondary fields. For a candidate pattern, the smaller the mismatch, the higher the similarity to the test object UXO U1.

After sweeping the candidate patterns, we get the mismatch values as shown in Fig. 5-29.

It can be seen that the mismatch of candidate pattern P10 is nearly zero (actually 0.0045) and notably less than those of other candidate patterns. If the discrimination threshold is set to 0.01, we draw the conclusion that the object producing the candidate pattern P10 is UXO U1 being sought, which agrees with the experimental truth. Other than pattern P10, pattern P7 (produced by object C1) produces the smallest mismatch. We also observe that the objects made of steel produce a higher similarity to the pattern of UXO U1 than those made of aluminum with similar size.

5.8.2 Pattern classification

The characteristic scattering coefficients can be used to train a support vector machine (SVM) to sort objects into generic classes, such as elongated or not, permeable or not. We first introduce the support vector machine.

Principle of SVM

The Support Vector Machine (SVM) has been applied to a wide range of pattern-recognition problems, and has achieved remarkable success [10, 77, 78]. Based on the statistical learning theory and structural-risk minimization principle[79, 80], the SVM finds a nonlinear decision function in the pattern space (input space) by mapping the data into a higher dimensional feature space and separates them there by means of a maximum margin hyper-
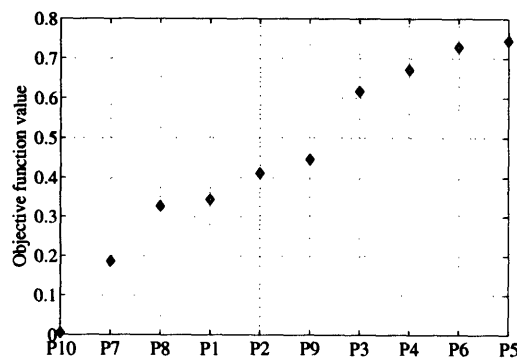
Figure 5-29: Sorted mismatch value of each candidate pattern

plane. In the training of an SVM , a subset of informative input points, known as support vectors, are identified automatically by the system and are used to make binary decisions in the testing process.

A simple way to build a binary classifier is to construct a plane separating separating one pattern class, "+1" from another pattern class, "−1". However, most real-world problems involve data for which there is no such simple plane that separates the two pattern classes. One solution to this problem is to map the data in pattern space (input space) to a higher-dimensional space, known as feature space, and define a separating hyperplane there. Here is an example illustrating this idea. As shown in Fig. 5-30, there are two classes, "+1", represented by the squares on the inner circle, and "−1", represented by the cross on a outer circle. There does not exist a straight line that separates the class "+1" from the class "−1". However, under a mapping defined as

$$\Phi : \mathbb{R}^2 \rightarrow \mathbb{R}^3$$

$$(u_1, u_2) \mapsto (x_1, x_2, x_3) = (u_1^2, \sqrt{2}u_1u_2, u_2^2),$$

the data in the three-dimensional feature space can be separated by a plane. In fact, the mapping of any circle located in between the inner and outer circles can be the separating hyperplane in the feature space.

Assume that we are given a set of training observations, $\{u_i, y_i\}, (i = 1, \ldots, N)$, with input data $u_i \in \mathbb{R}^n$ and corresponding binary class labels $y_i \in \{-1, +1\}$. Let $x_i = \Phi(u_i)$ be the feature vectors obtained by a nonlinear mapping Φ. In the feature space, assume that the hyperplane is expressed by

$$< w, x > + b = 0 \tag{5.13}$$

where w represents the vector normal to the hyperplane. For a given hyperplane, we can always scale w and b so that the hyperplane is in a canonical form in which

$$\begin{cases} < w, x_i > + b \geq +1, & \text{if } y_i = +1 \\ < w, x_i > + b \leq -1, & \text{if } y_i = -1, \end{cases} \tag{5.14}$$

137
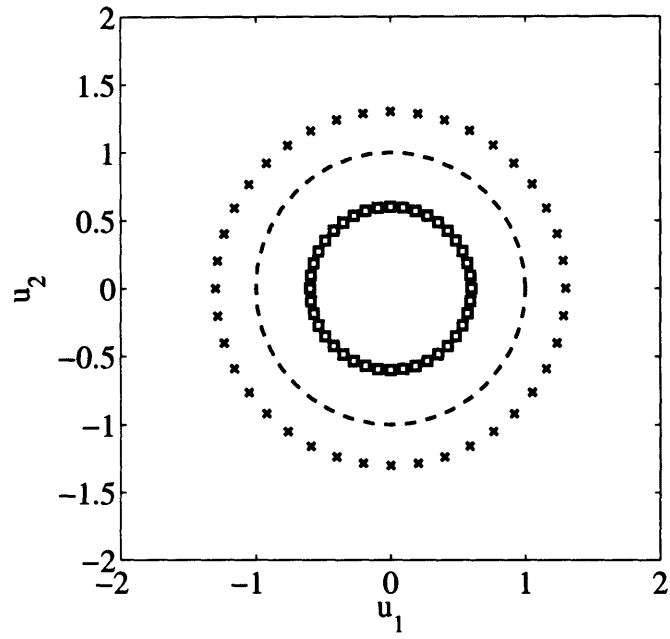
(a) Patter space
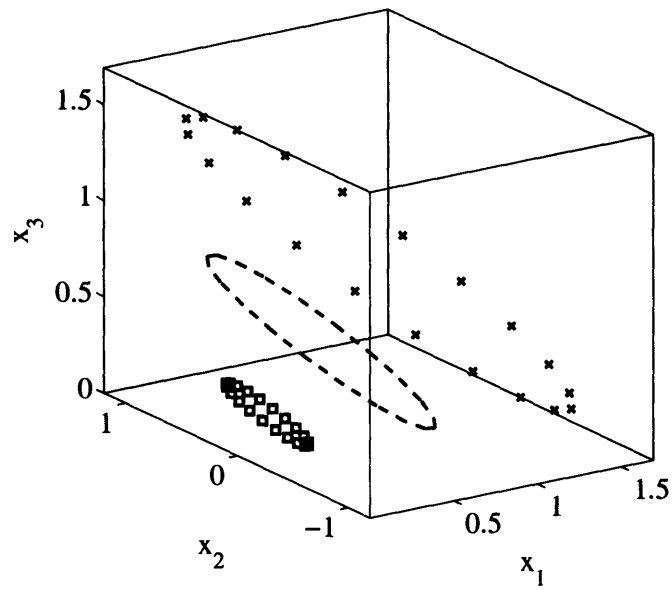
(b) Feature space

Figure 5-30: Illustration of mapping from the pattern space to the feature space
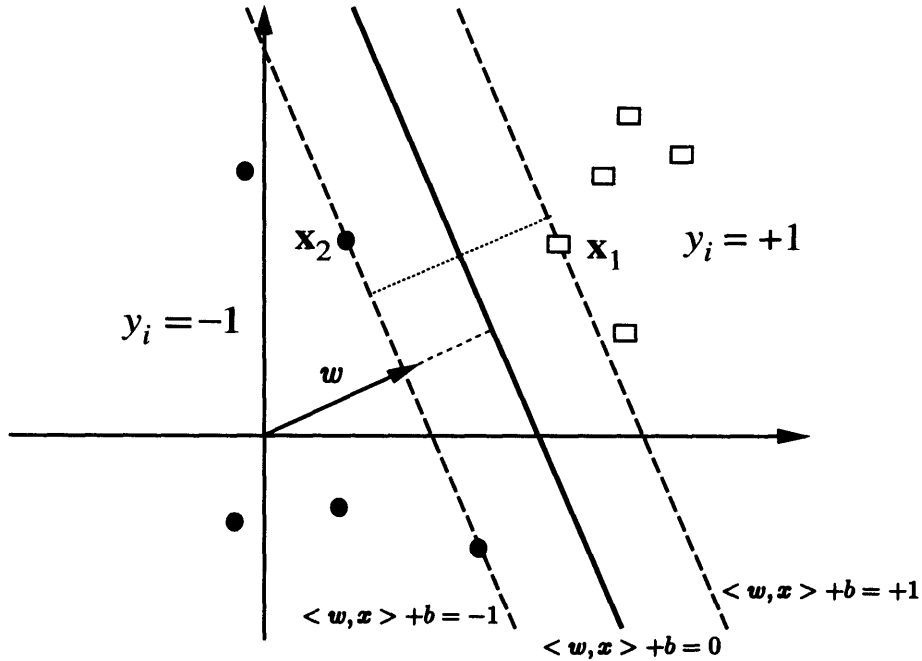
Figure 5-31: Canonical optimal hyperplane in the feature space

which is equivalent to

$$y_i[< w, x_i > +b] \geq 1, \quad i = 1, \ldots, N. \quad (5.15)$$

We show here that the separation between the two classes due to the hyperplane is proportional to $1/||w||$, where $||w||$ denotes the norm of w. Let the x_1 and x_2 be the closest points to the hyperplane among the points in class "+1" and "−1", respectively, as shown in Fig. 5-31. It is easy to see that

$$
\begin{aligned}
< w, x_1 > +b &= +1, \\
< w, x_2 > +b &= -1, \\
< w, (x_1 - x_2) > &= 2, \\
< w/||w||, (x_1 - x_2) > &= 2/||w|| \quad (5.16)
\end{aligned}
$$

From Eq. (5.16), we see that the separation between the two classes is proportional to $1/||w||$. The larger the separation, the better the classification ability.

One thing worth mentioning is that the SVM may not be able to find any separation hyperplane sometimes in the presence of the the noise. Consequently, the problem is addressed by using a "soft margin" that accepts classification error in the training examples. To reflect this idea, we modify Eq. (5.15) by introducing the slack variables ξ:

$$y_i[< \boldsymbol{w}, \boldsymbol{x}_i > +b] \geq 1 - \xi_i, \quad i = 1, \ldots, N. \tag{5.17}$$

where

$$\xi_i \geq 0, \quad , i = 1, \ldots, N. \tag{5.18}$$

Thus, a support vector machine can be specified by controlling both the classification margin and the the magnitude of the penalty for the training error. This is achieved by minimizing the objective function

$$f(\boldsymbol{w}, \boldsymbol{\xi}) = \frac{1}{2}||\boldsymbol{w}||^2 + C \sum_{i=1}^{N} \xi_i \tag{5.19}$$

subject to Eqs. (5.17) and (5.18) for some constant C that represents the trade-off between the classification ability and the training errors.

The above constrained optimization problem can be solved by the method of Lagrange multipliers. It is well-known from optimization theory that the solution is characterized by the saddle of the Lagrangian. After mathematical manipulations, we finally arrive at the dual formulation of the original problem:

$$\text{Max } Q(\boldsymbol{\alpha}) = \sum_{i=1}^{N} \alpha_i - \frac{1}{2} \sum_{i,j=1}^{N} \alpha_i \alpha_j y_i y_j < \boldsymbol{x}_i, \boldsymbol{x}_j > \tag{5.20}$$

subject to

$$\begin{cases} 0 \leq \alpha_i \leq C & i = 1, 2, \ldots, N \\ \sum_{i=1}^{N} \alpha_i y_i = 0 \end{cases} \tag{5.21}$$

We observe that the optimization problem(Eqs. (5.20) and (5.21)) is a quadratic programming problem, and the its solution can always be deterministically found, regardless of the initial points.

Once $\boldsymbol{\alpha}$ is obtained, the optimal separating hyperplane is identified in which $\boldsymbol{w}$ is ex-

plicitly determined $(w = \sum_{i=1}^{N} \alpha_i y_i x_i)$ and b is implicitly determined from the optimal condition of the Eq. (5.19) [77]. Thus, the SVM classifier is obtained,

$$y(u) = \text{sign}\left(\sum_{i=1}^{m} \alpha_i y_i < \Phi(u), \Phi(x_i) > +b\right). \tag{5.22}$$

Those u_i for which $\alpha > 0$ lie close to the decision hyperplane and are called the "support vectors", since the removal of them would change the location of the separating hyperplane. Thus, the SVM focuses upon the small subset of examples that are critical to differentiating one class from another class, discarding the remaining examples.

Note that feature vector $\Phi(u)$ always appears in the format of dot product in the decision function Eq. (5.22). Thus, after defining a function $K(u, u_i) = < \Phi(u), \Phi(u_i) >$, there is no need to compute $\Phi(u)$ explicitly. The function $K(u, u_i)$ is known as "kernel function". Mathematicians often find that it is easier to specify a kernel function than to specify explicitly the mapping function. As long as the kernel function is legitimate, an SVM will operate correctly even if we do not know exactly what features of the training data are being used in the kernel-induced feature space. The definition of a legitimate kernel function requires that the function must be continuous and positive definite [80]. Several choices of the kernel $K(u, u_i)$ are possible [77]:

- Liner kernel: $K(u, u_i) = u_i^T u$

- Polynomial kernel: $K(u, u_i) = (u_i^T u + 1)^d$

- Gaussian kernel: $K(u, u_i) = e^{-\|u - u_i\|^2 / \sigma^2}$

In fact, the kernel function expresses the similarity measure between the patterns u and u_i. The more similar between u and u_i, the larger the kernel function $K(u, u_i)$.

To my knowledge, there is no a kernel that works well for all classification problems, so we have to find the appropriate kernel by try-and-error. When the data in the pattern space are separable by a plane, liner kernel is a good candidate. If the data in the pattern space cannot be separated by a plane, nonlinear kernels are needed. For the polynomial kernel, when d is equal to one, it reduces to the linear kernel since an additional constant does not contribute to the decision. For the Gaussian kernel, a too large value of σ makes the kernel

141

always close to one, thus the SVM thinks that any two data in the pattern space are always almost identical. On the other hand, a too small value of σ makes the kernel always close to zero, thus any two data in the pattern space are thought by the SVM to be very different unless they are exactly identical ($\|u - u_i\| = 0$). In addition, the choice of σ also depends on the scale of u since σ and u are in the denominator and numerator of the argument of an exponential function.

The SVM software "mySVM"

In the following classification examples, a free non-commercial software "mySVM" is used [81]. The software mySVM is an implementation of the support vector machine, and it can be used for pattern classification. When using mySVM, we need to supply mainly the following parameters: the capacity parameter C ($C > 0$) in Eq. (5.19), the kernel definition, the training data, and the test data. I've applied mySVM to some analytical functions, for example, $\frac{\sin x}{x} > 0.5$? (for $x \in [-\pi, \pi]$), $\sin x_1 \cos x_2 < 0$? (for $x_1, x_2 \in [-\pi, \pi]$). The fact that more than 90% of the test data are correctly classified shows that the software works well.

Classification results based on synthetic data

In this section, we apply an SVM on synthetic data to sort unseen objects into generic classes, e.g., elongated or not, permeable or not, based on examination of the scattering coefficients $B_k^{(j)}$. In order to obtain the scattering coefficients $B_k^{(j)}$, we first calculate the secondary fields produced by the objects, which are then used as the "measured" data to retrieve $B_k^{(j)}$ in a given spheroidal coordinate system. Note that in order to compare the scattering coefficients, we have to retrieve them in the same coordinate system, regardless of the shapes and sizes of the objects.

Example 1: Is the spheroid elongated ($e > 2$)?

In this example, we say a spheroid is "elongated" if the elongation (e) is greater than 2. The parameters of the spheroids considered in the training and the test are as follows: The range of elongation is $e \in [0.2, 5]$, the relative permeability is $\mu_r \in [1, 250]$, length of

major axis (the maximum of $2a$ and $2b$) is between 0.05 and 0.65 (m), the conductivity is chosen to be a constant $\sigma = 10^7$ (S/m).

The input to the SVM are the scattering coefficients $B_k^{(j)}$ retrieved in a spheroidal coordinate system with the interfocal distance $d = 0.01$ (m). Only the fundamental modes of $B_k^{(j)}$ are considered in the classification, i.e., $j = (0,0,1),(0,1,1),(1,1,1)$ and $k = (0,0,0),(0,0.1),(0,1,1),(1,1,1)$. For a given spheroid, both the real and the imaginary parts of the fundamental modes retrieved at the limiting operating frequencies 10 Hz and 100 kHz compose one input point in the pattern space. Thus, the dimension of each input is 48 ($3 \times 4 \times 2 \times 2$). The scattering coefficients of 394 different spheroids randomly chosen from the ranges mentioned in the previous paragraph are retrieved, and are sent to a SVM program "mySVM" (see [81]) as the training data. Then the trained SVM predicts whether the 93 test spheroids are elongated ($e > 2$?) or not. The classification results are listed in the Table 5.8. We observe that only 3 out of 93 spheroids are misclassified.

We sort the spheroids used in the tests by the elongation, and plot the corresponding prediction results in Fig. 5-32. We see that those spheroids with an elongation close to 2 are more likely to be wrongly classified.

Example 2: Is the composite object elongated ($e > 2.5$)?

In the second example, SVM will determine whether a composite object is elongated or not ($e > 2.5$?). The composite consists of two spheroids, one oblate ($e_1 = 1/3$) and the other prolate ($e_2 = 3$), coaxially placed as shown in Fig. 5-33, with the closest points separated by 0.05 (m). The range of the parameter b (semi-axis) for the oblate spheroid is $b_1 \in [0.01, 0.05]$ (m), and $b_2 \in [0.03, 0.25]$ (m) for the prolate spheroid. The range of the relative permeability for both of the spheroids is $\mu_r \in [1, 250]$. We choose the conductivities of the two spheroids to be 10^7 (S/m) and 2.8×10^6 (S/m), respectively. The

Table 5.8: SVM classification results for spheroids: Class $+1$ for $e > 2$; Class -1 otherwise

		Number of predicted values	
		$+1$	-1
Number of	$+1$	48	2
true values	-1	1	42
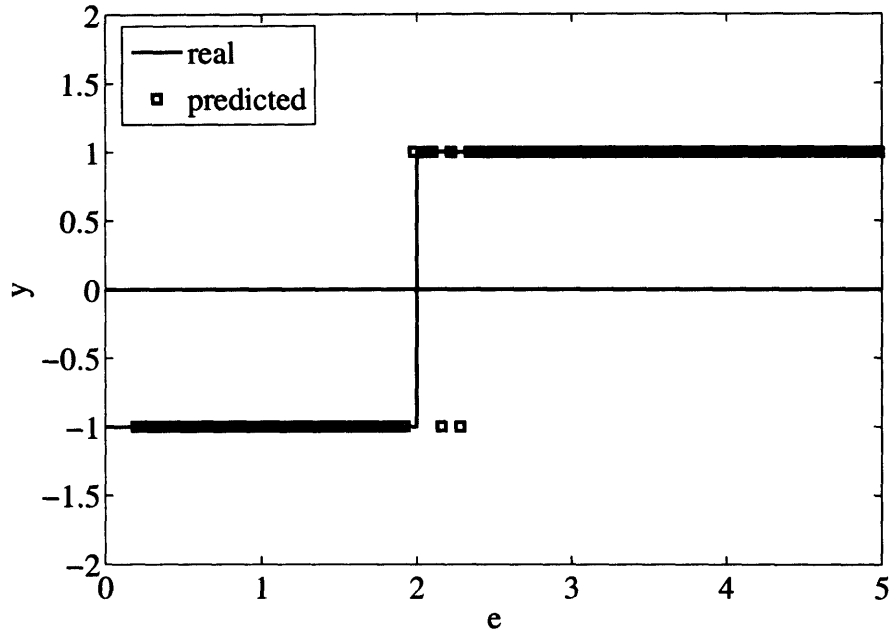
Figure 5-32: Classification results: if the spheroid is elongated or not ($e > 2$) ?

Table 5.9: SVM classification results for composite objects: Class $+1$ for $e > 2.5$; Class -1 otherwise

		Number of predicted values	
		$+1$	-1
Number of	$+1$	33	0
true values	-1	0	66

interfocal distance of the spheroidal coordinate system and operating frequency are same as those in the example 1. Elongation is defined by the ratio of the length along the axial direction to the widest dimension.

After being trained by 483 input patterns, the SVM predicts whether 99 test composite objects are elongated or not. The prediction results are shown in Table 5.9. It shows that all the test patterns are correctly classified.

Example 3: permeable ($\mu_r > 20$?)

In the third example, we will determine whether a homogeneous spheroid is permeable or not ($\mu_r > 20$?). The parameters of the spheroids considered in the training and the test are as follows: The range of elongation is $e \in [0.2, 5]$, the relative permeability is
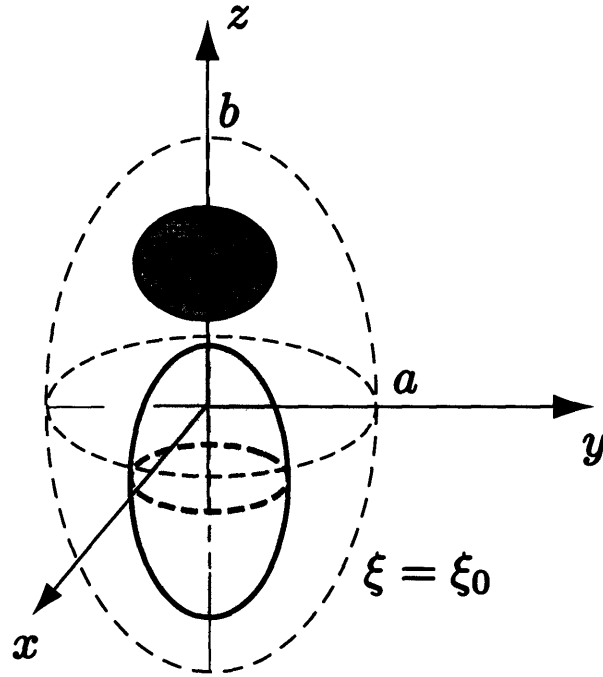
Figure 5-33: Composite object for classification

Table 5.10: SVM classification results for spheroids: : Class +1 for $\mu_r > 20$; Class -1 otherwise

		Number of predicted values	
		+1	-1
Number of	+1	55	0
true values	-1	0	43

$\mu_r \in [1, 150]$, length of major axis (the maximum of $2a$ and $2b$) is between 0.1 (m) and 0.3 (m), the conductivity is chosen to be $\sigma = 2.8 \times 10^7$ (S/m) for $\mu_r < 20$, or $\sigma = 10^6$ (S/m) for $\mu_r > 20$. the interfocal distance of spheroidal coordinate system is chosen to be $d = 0.236$ (m) and the operating frequencies are 210 Hz, 10,950 Hz. The scattering coefficients $B_k^{(j)}$ are obtained for the BOR model, and the real and the imaginary parts of $B_k^{(j)}$ of the fundamental modes $(j = k = (0,0,1)$ and $j = k = (0,1,1))$ are chosen to compose an eight-dimension pattern space $(2 \times 2 \times 2)$.

After being trained by 448 input patterns, the SVM predicts whether the 98 test composite object are permeable or not. The prediction results are shown in Table 5.10. It shows

that all the test patterns are correctly classified.

Classification results based on experimental data

In the last example, we use an SVM to determine whether real objects are elongated or not
($e > 2$?). The objects considered are listed in the Table 5.11. We use the GEM-3 sensor to
collect the secondary fields produced by those objects, and the scattering coefficients $B_k^{(j)}$
are retrieved and saved in the library. Note that the method used here for retrieving the
scattering coefficients $B_k^{(j)}$ is same as that applied to the object U2 as described in section
5.7.1, i.e., only z component of the magnetic field is used, the measurements are performed
on two cross lines, and different orientations and altitudes of the object are considered.
The interfocal distance of the spheroidal coordinate system is 0.236 (m), and the operating
frequencies are 210 Hz and 10,950 Hz.

The ideal situation is that we train SVM using the scattering coefficients $B_k^{(j)}$ obtained
for the real object. But we have limited number of those real objects. So we have to resort
to synthetic data in the training of SVM. In the training we train SVM using the scattering
coefficients $B_k^{(j)}$ of both 163 synthetic homogeneous spheroids and a real UXO U2. Here
all of the objects are treated as BORs and the dimension of each input is eight. After
training, SVM predicts whether the real objects are elongated or not.

The prediction results show that only U4, U5, and U6 are misclassified. The reason for
the misclassification is that all but one training data are for synthetic homogeneous media,
while all the data for testing are obtained from measurement for real object. When we have
more (say, hundreds of) real objects used for training, we expect to have better results in
the testing.

5.9 Conclusion and discussion

In this chapter, we adopt a spheroidal mode approach in the use of electromagnetic induc-
tion (EMI). Both the exciting and the induced magnetic fields are expanded as a linear com-
bination of basic modes in the spheroidal coordinate system. For the inversion of a single
spheroid, the DE algorithm is used to characterize the material properties, general shape,
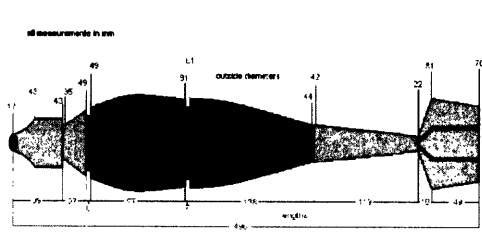
(a) U3
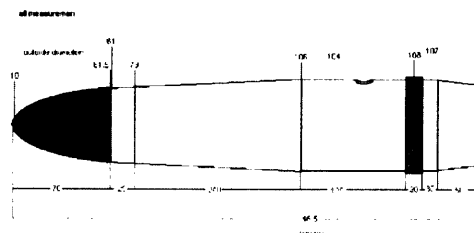
(b) U4
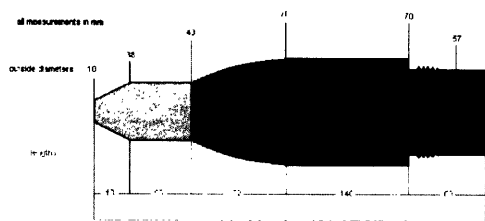
(c) U5.
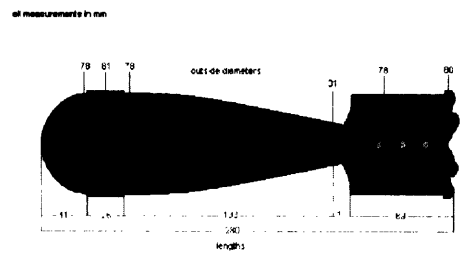
(d) U6
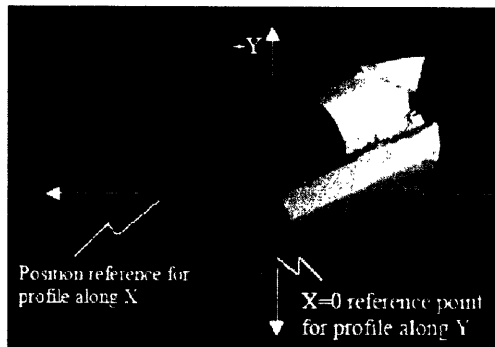
(e) U7
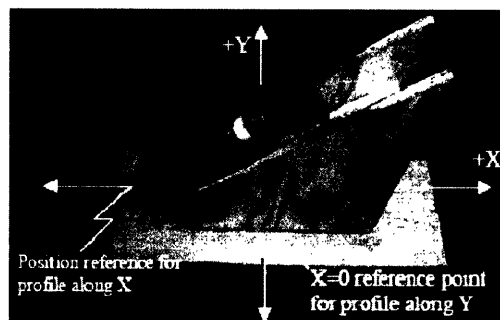
(f) U8
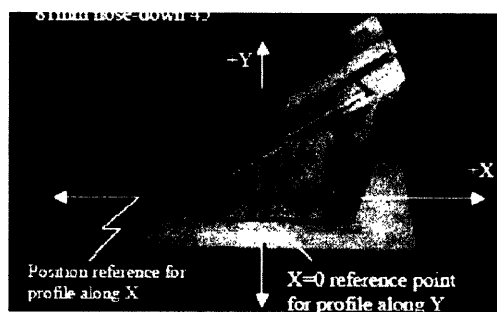
(g) U9

Figure 5-34: UXO objects for the use of classification (Courtesy of Dr. K. O'Neill)

Table 5.11: List of objects used for SVM classification

Object	Material	widest dimension	longest dimension	elongation (e)
I1	Iron	91 mm	91 mm	1
S2	Steel	30 mm	182 mm	6
S3	Steel	30 mm	90 mm	3
S4	Steel	15 mm	90 mm	6
S5	Steel	30 mm	5 mm	1/6
S6	Steel	30 mm	10 mm	1/3
S7	Steel	30 mm	30 mm	1
S8	Steel	90 mm	30 mm	1/3
S9	Steel	90 mm	15 mm	1/6
A1	Aluminum	30 mm	180 mm	6
A2	Aluminum	30 mm	91 mm	3
A3	Aluminum	15 mm	91 mm	6
A4	Aluminum	30 mm	5 mm	1/6
A5	Aluminum	30 mm	9 mm	1/3
A6	Aluminum	30 mm	30 mm	1
A7	Aluminum	90 mm	30 mm	1/3
A8	Aluminum	90 mm	15 mm	1/6
U1		83 mm	280 mm	3.37
U2		62 mm	245 mm	3.40
U3		97 mm	490 mm	5.05
U4		108 mm	465 mm	4.31
U5		70 mm	399 mm	5.70
U6		81 mm	280 mm	3.46
U7		37 mm	110 mm	3.40
U8		60 mm	260 mm	4.33
U9		83 mm	400 mm	4.82

Table 5.12: SVM classification results for real objects: Class $+1$ for $e > 2$; Class -1 otherwise

		Number of predicted values	
		$+1$	-1
Number of	$+1$	11	3
true values	-1	0	11
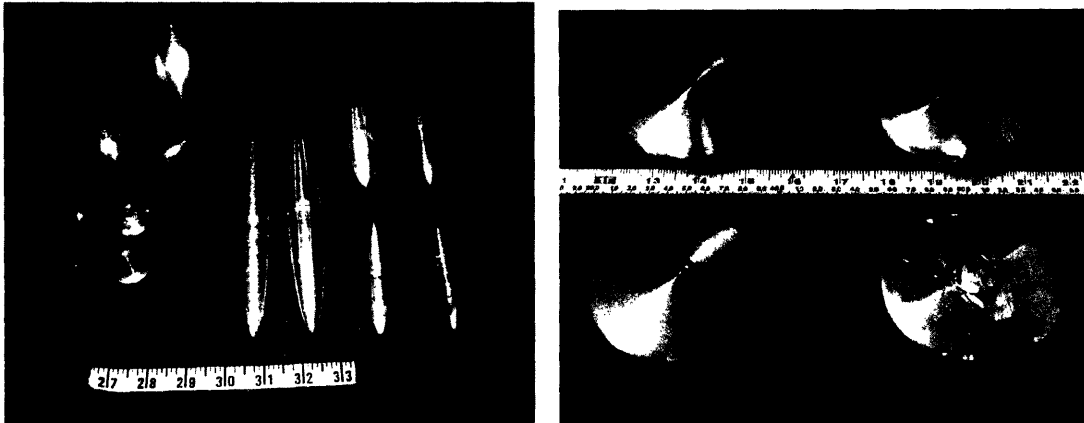
(a) All spheroids except S8, S9, A7, and A8   (b) Oblate spheroids S8, S9, A7, and A8

Figure 5-35: All spheroidal objects for the use of classification (Courtesy of Dr. K. O'Neill)

and location of a subsurface object. Beyond this, the response of any discrete scatterer (including non-spheroidal objects) can be represented in terms of basic mode solutions in spheroidal coordinates. Theoretical analysis proves that the scattering coefficients are the characteristics of the object, which is subsequently verified by numerical examples. The scattering coefficients are retrieved from the knowledge of the secondary fields, where both the synthetic and measurement data are used. The ill-conditioning issue is dealt with by mode truncation and Tikhonov regularization technique. It is encouraging that only four primary modes and few fundamental secondary modes ($m \leq 1$ and $n \leq 1$) are needed in the inversion of the characteristic scattering coefficients. Stored in a library, the scattering coefficients can produce fast forward models for use in pattern matching. Also they can be used to train a support vector machine (SVM) to sort objects into generic classes, such as elongated or not, permeable or not.

Chapter 6

Conclusion

In this thesis, I have dedicated myself to the investigation of two inverse problems. The first is the retrieval of the effective constitutive parameters of metamaterials from the measurement of the reflection and the transmission coefficients. The second inverse problem deals with the detection and the classification of buried metallic objects using electromagnetic induction (EMI).

Retrieval of constitutive parameters

In the retrieval of constitutive parameters, my work contains three parts:

First, a robust method is proposed for the retrieval of metamaterials as isotropic media, and four improvements over the existing methods make the retrieval results more stable. The main conclusion is as follows:

(1). The first boundary and the thickness of the effective media can be determined by matching z through all sample frequencies for different lengths of slabs in the propagation direction. For symmetric 1D metamaterials, we have drawn the empirical conclusion that the first boundary coincides with the first boundary of the unit cell facing the incident wave, and the thickness of the effective medium is approximately equal to the number of unit cells multiplied by the length of a unit cell. For 2D and asymmetric 1D metamaterials, the effective boundaries have to be determined by optimization.

(2). The requirement $z' \geq 0$ cannot be used directly for practical retrievals when z' is

151

close to zero because the numerical or measurement errors may flip the sign of z', making the result unreliable. In this case, we have to determine the sign of z by the value of its corresponding n so that $n'' \geq 0$.

(3). There is a resonance band characterized by the fact that the requirement $\mu'' \geq 0$ and $\epsilon'' \geq 0$ cannot be satisfied at those frequencies. On each side of the resonance, the branch of n' can be obtained by a Taylor expansion approach considering the fact that the refractive index n is a continuous function of frequency. Since the refractive index n at the initial frequency determines the values of n' at the subsequent frequencies, we determine the branch of the real part of n at the initial frequency by requiring that μ'' and ϵ'' are non-negative across all the frequency band.

(4). Due to the noise contained in the S parameters, the retrieved n and z at some specific frequencies are not reliable, especially for thicker metamaterials at lower frequencies. In spite of this, the fact that S_{11} and S_{21} for multiple cells of metamaterial calculated from the retrieved ϵ and μ for a unit cell metamaterial match the S_{11} and S_{21} computed directly from numerical simulation confirms that the metamaterials can be treated as an effective homogeneous material.

Second, a new scheme is presented for the retrieval of a specific bianisotropic metamaterial that consists of split-ring resonators, which signifies that the cross polarization terms of the metamaterial are quantitatively investigated for the first time. The main conclusion is as followings:

(1). Analytical inversion equations are proposed to retrieve the constitutive parameters of homogeneous lossless bianisotropic media, while a numerical approach is proposed for lossy bianisotropic media. Both methods have been first validated using analytical functions as input values for the constitutive parameters and second, using simulated S parameters of real split-ring structures.

(2). The retrieval results qualitatively corroborate the conclusions of previously published articles, proving the existence of the bianisotropy in the edge-coupled SRR metamaterials, but not in the broadside-coupled SRR metamaterials.

Third, an optimization approach is designed to achieve the retrieval of general bian-

isotropic media. The hybrid algorithm combining the differential evolution (DE) algorithm and simplex method steadily converges to the exact solution. The main conclusion is as followings:

(1). The method is for either rotated media with known constitutive properties or more general media with unknown constitutive properties.

(2). High dimensional inverse problems are attacked by the combination of differential evolution algorithm and simplex method. DE is used first to parallel explore the searching space and then simplex method is applied to accelerate the convergence. Fewer incidences are used in DE in order to reduce the computation burden and diverse incidences are used in simplex method in order to obtain the unique solution. Importantly, our method obtains a group of solutions, all of which are almost identical to the true one.

(3). Linear extrapolation of the results at the previous two frequencies are used as an initial guess for the retrieval of dispersive medium using simplex optimization method. Optimization results show that the constitutive parameters are reconstructed successfully.

(4). It should be noted that slabs with different thickness should be used for the broadband retrieval.

(5). The limitation of the proposed method is that it cannot deal with the bianisotropic media whose cross-polarization terms are not close to zero at low frequencies.

Detection and classification of a buried object

In the detection and classification of a buried object, we adopt a spheroidal mode approach in the use of electromagnetic induction (EMI). Both the exciting and the induced magnetic fields are expanded as a linear combination of basic modes in the spheroidal coordinate system. For the inversion of a single spheroid, the DE algorithm is used to characterize the material properties, general shape, and location of a subsurface object. Beyond this, the response of any discrete scatterer (including non-spheroidal objects) can be represented in terms of basic mode solutions in spheroidal coordinates. Theoretical analysis proves that the scattering coefficients are the characteristics of the object, which is subsequently verified by numerical examples. The scattering coefficients are retrieved from the knowledge of the secondary fields, where both the synthetic and measurement data are used. The ill-

conditioning issue is dealt with by mode truncation and Tikhonov regularization technique. It is encouraging that only four primary modes and few fundamental secondary modes ($m \leq 1$ and $n \leq 1$) are needed in the inversion of the characteristic scattering coefficients. Stored in a library, the scattering coefficients can produce fast forward models for use in pattern matching. Also they can be used to train a support vector machine (SVM) to sort objects into generic classes, such as elongated or not, permeable or not.

Bibliography

[1] R. A. Shelby, D. R. Smith, and S. Schultz, "Experimental verification of a negative index of refraction," *Science*, vol. 292, pp. 77–79, 2001.

[2] V. Veselago, "The electrodynamics of substances with simultaneously negative values of ϵ and μ," *Sov. Phys. Usp*, vol. 10, pp. 509–514, January-February 1968.

[3] D. R. Smith, W. J. Padilla, D. C. Vier, S. C. Nemat-Nasser, and S. Schultz, "Composite medium with simultaneously negative permeability and permittivity," *Phys. Rev. Lett.*, vol. 84, no. 8, pp. 4184–4187, 2000.

[4] L. Ran, X. Zhang, K. Chen, T. M. Grzegorczyk, and J. A. Kong, "Left-handed meta-material and its experimental verifications," *Chin. Sci. Bull.*, vol. 48, pp. 1325–1327, July 2003.

[5] J. Pendry, A. Holden, W. Stewart, and I. Youngs, "Extremely low frequency plasmons in metallic mesostructures," vol. 76, pp. 4773–4776, 17 June 1996.

[6] J. Pendry, A. Holten, and W. Stewart, "Magnetism from conductors and enhanced nonlinear phenomena," *IEEE Trans. Microwave Theory Tech.*, vol. 47, pp. 2075–2084, November 1999.

[7] J. A. Kong, "Electromagnetic wave interaction with stratified negative isotropic media," *Prog. Electromagn. Res.*, vol. 35, pp. 1–52, 2002.

[8] J. Pendry, "Negative refraction makes a perfect lens," *Phys. Rev. Lett.*, vol. 85, pp. 3966–3969, 30 October 2000.

[9] S. O'Brien and J. B. Pendry, "Photonic band-gap effects and magnetic activity in dielectric composites," *Journal of Physics: Condensed Matter*, vol. 14, pp. 4035–4044, Apr. 2002.

[10] Y. Zhang, L. Collins, H. Yu, C. Baum, and L. Carin, "Sensing of unexploded ordnance with magnetometer and induction data: theory and signal processing," *IEEE Trans. on Geoscience and Remote Sensing*, vol. 41, pp. 1005–1015, May 2003.

[11] B. E. Barrowes, K. O'Neill, T. M. Grzegorczyk, X. Chen, and J. A. Kong, "Boardband electromagnetic induction solution for a conducting and permeable spheroid," *IEEE Trans. on Geoscience and Remote Sensing*, vol. 42, pp. 2479–2489, Nov. 2004.

[12] B. E. Barrowes, *Electromagnetic Scattering and Induction Models for Spheroidal Geometries*. PhD thesis, Massachusetts Institute of Technology, January 2004.

[13] X. Chen, K. O'Neill, T. Grzegorczyk, B. Barrowes, C. Moss, B.-I. Wu, and J. A. Kong, "Fundamental mode approach in electromagnetic induction scattering and inversion," in *Progress in Electromagnetic Research Symposium*, (Honolulu, Hawaii, USA), p. 318, Oct. 2003.

[14] P. B. Weichman and E. M. Lavely, "Study of inverse problems for buried UXO discrimination based on EMI sensor data," in *SPIE Proc.*, vol. 5089, pp. 1189–1200, Apr. 2003.

[15] F. Shubitidze, K. O'Neill, K. Sun, and K. D. Paulsen, "Investigation of broadband electromagnetic induction scattering by highly conductive, permeable, arbitrarily shaped 3-D objects," *IEEE Trans. Geosci. Remote Sensing*, vol. 42, pp. 540–556, Mar. 2004.

[16] A. B. Tarokh, "A unified approach to statistical classification of buried objects from spatially sampled electromagnetic induction data," Master's thesis, Northeastern University, May 2003.

[17] H. Huang and I. Won, "Characterization of UXO-like targets using broadband electromagnetic induction sensors," *IEEE Trans. on Geoscience and Remote Sensing*, vol. 41, pp. 652–663, March 2003.

[18] F. Shubitidze, K. O'Neill, K. Sun, and I. Shamatava, "Interaction between highly conducting and permeable metallic objects in the low frequency EMI range," in *Proc. Applied Computational Electromagnetics Symp.*, (Monterey CA, USA), pp. 625–631, Mar. 2003.

[19] F. Shubitidze, K. O'Neill, K. Sun, I. Shamatava, and K. Paulsen, "Analysis of EMI scattering to support UXO discrimination: heterogeneous and multiple objects," in *Proc. SPIE'03*, (Orlando, FL, USA), pp. 929–939, Apr. 2003.

[20] F. Shubitidze, K. ONeill, K. Sun, I. Shamatava, and K. Paulsen, "A fast and accurate representation of physically complete EMI response by a heterogeneous object for enhanced UXO discrimination," *IEEE Trans. Geosci. Remote Sensing*, submitted for publication, 2004.

[21] F. Shubitidze, K. O'Neill, I. Shamatava, K. Sun, and K. Paulsen, "A new numerical procedure for efficient and accurate representation of low frequency EM responses for a heterogeneous object," in *Appl. Comput. Electromagn. Symp.*, (Syracuse, NY, USA), Apr. 2004.

[22] F. Shubitidze, K. O'Neill, I. Shamatava, K. Sun, and K. Paulsen, "Use of standardized source sets for enhanced EMI classification of buried heterogeneous objects," in *SPIE Defense and Security Symp.*, (Orlando, FL, USA), Apr. 2004.

[23] K. Sun, K. O'Neill, F. Shubitidze, I. Shamatava, and K. D. Paulsen, "Fundamental mode approach to forward problem solutions in EMI scattering - inferring fundamental solutions from training data," in *Appl. Comput. Electromagn. Symp.*, (Syracuse, NY, USA), Apr. 2004.

[24] K. Sun, K. O'Neill, F. Shubitidze, I. Shamatava, and K. D. Paulsen, "Fast data-derived fundamental spheroidal excitation mode to UXO identification," in *SPIE Defense and Security Symp.*, (Orlando, FL, USA), Apr. 2004.

[25] F. Shubitidze, K. O'Neill, K. Sun, I. Shamatava, and K. Paulsen, "A standardized excitation approach for classification of buried UXO," (Anchorage, AK, USA), Sep. 2004.

[26] X. Chen, K. O'Neill, B. E. Barrowes, T. M. Grzegorczyk, and J. A. Kong, "Application of a spheroidal-mode approach and a differential evolution algorithm for inversion of magneto-quasistatic data in UXO discrimination," *Inverse Problem*, vol. 20, pp. S27–40, 2004.

[27] K. Sun, K. O'Neill, I. Shamatava, F. Shubitidze, and K. D. Paulsen, "A fast forward model for simulating EMI scattering with realistic sensors and elongated objects," *Applied Computational Electromagnetics Society Journal*, vol. 18, no. 4, pp. 97–106, 2003.

[28] D. R. Smith, S. Schultz, P. Markoš, and C. M. Soukoulis, "Determination of effective permittivity and permeability of metamaterials from reflection and transmission coefficients," *Phys. Rev. B*, vol. 65, p. 195104, 2002.

[29] P. Markoš and C. M. Soukoulis, "Transmission properties and effective electromagnetic parameters of double negative metamaterials," *Opt. Express*, vol. 11, no. 7, pp. 649–661, 2003.

[30] R. W. Ziolkowski, "Design, fabrication, and testing of double negative metamaterials," *IEEE Trans. Antennas Propag.*, vol. 51, pp. 1516–1529, July 2003.

[31] A. M. Nicolson and G. F. Ross, "Measurement of the intrinsic properties of materials by time-domain techniques," *IEEE Trans. Instrum. and Meas.*, vol. 19, pp. 377–382, November 1970.

[32] J. Baker-Jarvis, E. J. Vanzura, and W. Kissick, "Improved technique for determining complex permittivity with the transmission/reflection method," vol. 38, pp. 1096–1103, August 1990.

[33] J. A. Kong, *Electromagnetic Wave Theory*. Cambridge, MA, USA: EMW, 2000.

[34] D. A. Shelby, D. R. Smith, S. C. Nemat-Nasser, and S. Schultz, "Microwave transmission through a two-dimensional, isotropic, left-handed metamaterial," *Appl. Phys. Lett.*, vol. 78, pp. 489–491, Jan. 2001.

[35] C. D. Moss, T. M. Grzegorczyk, Y. Zhang, and J. A. Kong, "Numerical studies of left handed metamaterials," *Prog. Electromagn. Res.*, vol. 35, pp. 315–334, 2002.

[36] R. Storn and K. Price, "Differential evolution - a simple and efficient heuristic for global optimization over continuous spaces," *J. Global Optim.*, vol. 11, pp. 341–359, 1997.

[37] C. R. Simovski, P. A. Belov, and S. He, "Backward wave region and negative material parameters of a structure formed by lattices of wires and split-ring resonators," *IEEE Trans. Antennas Propag.*, vol. 51, pp. 2582–2591, Oct. 2003.

[38] J. E. Sipe and J. V. Lranendonk, "Macroscopic electromagnetic theory of resonant dielectrics," *Phys. Rev. A*, vol. 9, pp. 1806–1822, May 1974.

[39] P. A. Belov, S. A. Tretyakov, and A. J. Viitanen, "Nonreciprocal microwave band-gap structure," *Phys. Rev. E*, vol. 66, p. 016608, May 2002.

[40] T. Koschny, P. Markoš, D. R. Smith, and C. M. Soukoulis, "Resonant and antiresonant frequency dependence of the effective parameters of metamaterials," *Phys. Rev. E*, vol. 68, p. 065602, 2003.

[41] R. Marqués, F. Mesa, J. Martel, and F. Medina, "Comparative analysis of edge- and broadside-coupled split ring resonators for metamaterial design–theroy and experiments," *IEEE Trans. Antennas Propag.*, vol. 51, pp. 2572–2581, Oct. 2003.

[42] R. Marqués, F. Medina, and R. Rafii-El-Idrissi, "Role of bianisotropy in negative permeability and left-handed metamaterial," *Phys. Rev. B*, vol. 65, p. 144440, 2002.

[43] N. Katsarakis, T. Koschny, M.Kafesaki, E. N. Economou, and C. M. Soukoulis, "Electric coupling to the magnetic resonance of split ring resonators," *Appl. Phys. Lett.*, vol. 84, pp. 2943–2945, Aug. 2004.

[44] J. A. Kong, "Theorems of bianisotropic media," *Proc. IEEE*, vol. 60, pp. 1036–1046, 1972.

[45] P. Gay-Balmaz and O. J. F. Martin, "Electromagnetic resonances in individual and coupled split-ring resonators," *J. Appl. Phys.*, vol. 92, pp. 2929–2936, Sep. 2002.

[46] X. Chen, T. M. Grzegorczyk, B.-I. Wu, J. Pacheco, and J. A. Kong, "Robust method to retrieve the constitutive effective parameters of metamaterial," *Phys. Rev. E*, vol. 70, p. 016608, July 2004.

[47] T. M. Grzegorczyk, X. Chen, J. Pacheco, J. Chen, B.-I. Wu, and J. A. Kong, "Reflection coefficients and Goos-Hanchen shift in anisotropic and bianisotropic left-handed metamaterials," *Prog. Electromagn. Res.*, vol. 51, pp. 83–113, 2005.

[48] S.Rikte, G.Kristensson, and M.Andersson, "Propagation in bianisotropic media - reflection and transmission," *IEE Proc.-Microw. Antennas Propag.*, vol. 148, pp. 29–36, February 2001.

[49] W. C. Chew, *Waves and Fields in Inhomogeneous Media.* Electromagnetic Waves, IEEE Press, 1995.

[50] Y. A. Kao, "Finite-difference time-domin modeling of oblique incidence scattering from periodic surface," Master's thesis, Massachusetts Institute of Technology, Apr. 1997.

[51] D. R. Smith, D. C. Vier, T. Koschny, and C. M. Soukoulis, "Electromagnetic parameter retrieval from inhomogeneous metamaterials," *Phys. Rev. E*, vol. 71, p. 036617, Mar. 2005.

[52] X. Chen, B. Wu, J. A. Kong, and T. M. Grzegorczyk, "Retrieval of the effective constitutive parameters of bianisotropic metamaterials," *Phys. Rev. E*, vol. 71, p. 046610, Apr. 2005.

[53] L. H. Ruotanen and A. Hujanen, "Simple derivation of the constitutive parameters of an isotropic chiral slab from wideband measurement data," *Microwave Opt. Technol. Lett.*, vol. 12, pp. 40–45, May 1996.

[54] R. Luebbers, H. S. Langdon, F. Hunsberger, C. F. Bohren, and S. Yoshikawa, "Calculation and measurement of the effective chirality parameter of a composite chiral material over a wide frequency band," *IEEE Trans. Antennas Propag.*, vol. 43, pp. 123–130, Feb. 1995.

[55] A. B. de Monvel and D. Shepelsky, "Reconstruction of a stratified omega medium and the associated riemann-hilbert problem," *Inverse Problem*, vol. 18, pp. 1377–1395, Oct. 2002.

[56] M. Norgren, "General optimization approach to a frequency-domain inverse problem for stratified bianisotropic slab," *J. Electromagnetic Waves and Applications*, vol. 11, pp. 515–546, 1997.

[57] R. Storn, "System design by constraint adaptation and differential evolution," *IEEE Trans. Evolutionary Comput.*, vol. 3, pp. 22–34, Apr. 1999.

[58] E. C. Laskari, K. E. Parsopoulos, and M. N. Vrahatis, "Evolutionary operators in global optimization with dynamic search trajectories," *Numer. Algorithms*, vol. 34, pp. 393–403, Dec. 2003.

[59] S. S. Rao, *Engineering optimization : theory and practice*. New York: Wiley, 1996.

[60] J. A. Nelder and R. Mead, "A simplex method for function minimization," *Comput. J.*, vol. 7, pp. 308–313, 1965.

[61] L. Tsang, J. A. Kong, and K. H. Ding, *Scattering of Electromagnetic Waves: Theories and Applications*. Wiley-Interscience, 2000.

[62] V. Dmitriev, "Constitutive tensors of omega- and chiroferrites," *Microwave Opt. Technol. Lett.*, vol. 29, pp. 201–205, May 2001.

[63] I. J. Won, D. A. Keiswetter, D. Hansen, E. Novikova, and T. M. Hall, "Gem-3: a monostatic broadband electromagnetic induction sensor," *Jour. Envir. Eng. Geophysics*, vol. 2, no. 1, pp. 53–64, 1997.

[64] I. J. Won, D. A. Keiswetter, and T. H. Bell, "Electromagnetic induction spectroscopy for clearing landmines," *IEEE Trans. on Geoscience and Remote Sensing*, vol. 39, pp. 703–709, April 2001.

[65] K. Sun, K. O'Neill, F. Shubitidze, S. A. Haider, and K. D. Paulsen, "Simulation of electromagnetic induction scattering from targets with negligible to moderate penetration by primary fields," *IEEE Trans. on Geoscience and Remote Sensing*, vol. 40, pp. 910–27, April 2002.

[66] H. Braunisch, C. O. Ao, K. O'Neill, and J. A. Kong, "Magnetoquasistatic response of conducting and permeable spheroid under axial excitation," *IEEE Trans. on Geoscience and Remote Sensing*, vol. 39, pp. 2689–2701, December 2001.

[67] C. O. Ao, H. Braunisch, K. O'Neill, , and J. A. Kong, "Quasi-magnetostatic solution for a conducting and permeable spheroid with arbitrary excitation," *IEEE Trans. on Geoscience and Remote Sensing*, vol. 40, pp. 887–897, April 2002.

[68] H. W. Wyld, *Mathematical methods for physics*. Reading, MA, USA: W. A. Benjamin, Inc., 1976.

[69] C. O. Ao, *Electromagnetic Wave Scattering by Discrete Random Media with Remote Sensing Applications*. PhD thesis, Massachusetts Institute of Technology, May 2001.

[70] E. W. Hobson, *The theory of spherical and ellipsoidal harmonics*. New York, USA: Chelsea Pub. Co., 1955.

[71] L. Peters, J. J. Daniels, and J. D. Young, "Ground penetrating radar as a subsurface environmental sensing tool," *Proc. IEEE*, vol. 82, pp. 1802–1822, Dec. 1994.

[72] D. G. Beetner and R. M. Arthur, "Estimation of heart-surface potentials using regularized multipole sources," *IEEE Transactions on Biomedical Engineering*, vol. 51, pp. 1366–1373, Aug. 2004.

[73] J. Colinas, Y. Goussard, and J. J. Laurin, "Application of the tikhonov regularization technique to the equivalent magnetic currents near-field technique," *IEEE Trans. Antennas Propag.*, vol. 52, pp. 3122–3132, Nov. 2004.

[74] A. Neumaier, "Solving ill-conditioned and singular linear systems: A tutorial on regularization," *SIAM Review*, vol. 40, pp. 636–666, Sep. 1998.

[75] S. Begot, E. Voisin, P. Hiebel, J. M. Kauffmann, and E. Artioukhine, "Resolution of linear magnetostatic inverse problem using iterative regularization," *European Physical Journal-Applied Physics*, vol. 12, pp. 123–131, Nov. 2000.

[76] A. Kirsch, *An introduction to the mathematical theory of inverse problem*. New York: Springer, 1996.

[77] C. J. C. Burges, "A tutorial on support vector machines for pattern recognition," *Data Mining and Knowledge Discovery*, vol. 2, pp. 121–167, 1998.

[78] M. P. S. Brown, W. N. Grundy, D. Lin, N. Cristianini, C. W. Sugnet, T. S. Furey, M. Ares, and D. Haussler, "Knowledge-based analysis of microarray gene expression data by using support vector machines," *Proceedings of the National Academy of Sciences of the United States of America*, vol. 97, pp. 262–267, Jan. 2000.

[79] V. Vapnik, *The nature of statistical learning theory*. New York: Springer, 1995.

[80] V. Vapnik, *Statistical learning theory*. New York: Wiley, 1998.

[81] S. Rüping, *mySVM-Manual*, University of Dortmund, Germany, http://www-ai.cs.uni-dortmund.de/SOFTWARE/MYSVM/, 2000.

[82] T. M. Grzegorczyk, C. D. Moss, J. Lu, X. Chen, J. Pacheco, and J. A. Kong, "Characterization of a low-loss metamaterial with left-handed properties." *IEEE Trans. Microwave Theory Tech.*, accepted for publication, 2005.

[83] C. D. Moss, *Numerical Methods for electromagnetic wave propagation and scattering in complex media.* PhD thesis, Massachusetts Institute of Technology, Feb. 2004.

[84] L. D. Landau, E. M. Lifshitz, and L. P. Pitaevskii, *Electrodynamics of Continuous Media.* Oxford: Pergamon, 2rd ed., 1984.

Biographical note

Xudong Chen was born in Liaoning, China on January 8, 1977 (November 11, 1976 by Chinese Lunar calendar). He received the B.Eng. and M.S. degrees in Electrical Engineering from Zhejiang University, Hangzhou, China, in 1999 and 2001 respectively. Since September 2001, he has been a research assistant in the Department of Electrical Engineering and Computer Science (EECS) and the Research Laboratory of Electronics (RLE) at Massachusetts Institute of Technology (MIT), Cambridge, Massachusetts, where his research interests are mainly in electromagnetic inverse problems, metamaterials, and bianisotropic media. From 2002 to 2005, he has been a teaching assistant in the EECS department of MIT for several graduate electromagnetic courses.